Faculty of Science

Noble Gases and Water Under Confinement in Graphenic Nanostructures: From Material Behavior to Interfacial Thermodynamics

Thesis submitted in fulfilment of the requirements for the degree of
doctor in philosophy in physics
at the University of Antwerp

Fahim Faraji

Supervisors
prof. dr. Erik C. Neyts
prof. dr. Mehdi Neek-Amal
prof. dr. Milorad V. Milošević

Antwerpen, 2024

Jury

Chairman
prof. dr. Dirk Lamoen, University of Antwerp, Belgium

Supervisors
prof. dr. Erik C. Neyts, University of Antwerp, Belgium
prof. dr. Mehdi Neek-Amal, University of Antwerp, Belgium
prof. dr. Milorad V. Milošević, University of Antwerp, Belgium

Members
prof. dr. Annemie Bogaerts, University of Antwerp, Belgium
prof. dr. Lino da Costa Pereira, Katholieke Universiteit Leuven, Belgium
prof. dr. Paola Carbone, University of Manchester, United Kingdom

Contact
Fahim Faraji
University of Antwerp
Faculty of Science
PLASMANT
Condensed Matter Theory (CMT)
Groenenborgerlaan 171, 2020 Antwerpen, België
M: fahim.faraji@uantwerpen.be

© 2024 Fahim Faraji
All rights reserved.

ISBN 987-90-57285-34-7
Wettelijk depot D/2022/12.293/03

Dutch title:

Edelgassen en Water Onder Opsluiting in Grafeenachtige Nanostructuren: Van Materiaalgedrag tot Interfaciale Thermodynamica

To Mom,
For Everything

Acknowledgements

I would like to express my deepest gratitude to my advisors, Prof. François M. Peeters, Prof. Erik C. Neyts, Prof. Mehdi Neek-Amal, and Prof. Milorad V. Milošević, whose unwavering guidance, invaluable insights, and continuous support have been instrumental throughout the entirety of my doctoral journey. Their expertise and encouragement have been pivotal in shaping the course of my research and academic growth.

Additionally, I extend my sincere appreciation to the experimentalists at KU Leuven, specifically the group of Prof. Lino da Costa Pereira, and at the University of Manchester, led by Prof. Irina Grigorieva, for their collaboration and contributions to my work, which enriched the depth and breadth of my research endeavors.

A heartfelt thank you extends to all my teachers and professors from the first stage of elementary school, whose dedication to education ignited my passion for learning and set the foundation for my academic pursuits.

To my family, both blood-related and my newfound Belgian family, consisting of Elke, Pjotr, Yoppe, Lotje, Tony, and Nora, your care and fondness have been a constant source of strength, and I am profoundly grateful for the warmth and kinship you have extended to me during my time in Belgium.

I extend my sincere appreciation to everyone in the CMT and PLASMANT groups at the University of Antwerp. The collaborative and stimulating research environment provided by these groups has been pivotal in shaping my research endeavors. Additionally, I would like to thank the CalcUA team for their support and access to the HPC core facility, which greatly enhanced the computational aspects of my research.

Special thanks go to all my friends made during my PhD, whose camaraderie and shared experiences have made this academic journey not only intellectually enriching but also a period of personal growth and lifelong connections.

This acknowledgment is a tribute to the collective efforts and support of all those who have been part of my academic and personal journey. Your contributions, whether big or small, have left an indelible mark, and for that, I am truly grateful.

During the writing of this thesis, artificial intelligence (AI) was utilized to assist with language-related issues, for which I am grateful.

Fahim Faraji
Antwerp, October 2024

Abstract

This thesis initiates an inquiry into the intricate interplay between confinement and material behaviors, addressing cutting-edge topics in nanomechanics and interfacial physics. Each section explores how confinement significantly alters material properties compared to their bulk counterparts, extending the investigation into the nuanced realm of thermodynamic properties at interfaces.

We first demonstrate the breakdown of a previously acknowledged universal aspect ratio (height versus diameter) in nanometer-sized bubbles within graphene, laying the groundwork for a detailed examination of adhesion energies. Further, the indentation of graphene nanobubbles reveals failure points reminiscent of viral shells through analysis using the Föppl–von Kármán (FvK) dimensionless number. Additionally, phase transitions of encapsulated noble gases are explored, exhibiting intriguing behaviors under varying temperatures.

The formation of anomalous shapes in flat nanobubbles encapsulated by hexagonal boron nitride is also investigated, highlighting the influence of heating rates and hydrogen bonding. The cation-controlled permeation of charged polymers through nanocapillaries is examined, revealing distinct effects of monovalent cations on polymer transmission speed. The ability to manipulate permeation is elucidated based on the differing surface versus bulk preferences of various alkali cations in the presence of an external electric field, offering valuable insights into the interplay between ionic dynamics and nano-confinement effects.

The exploration continues with an assessment of the accuracy of the Kelvin equation in nanoscale capillaries, proposing a revision based on disjoining pressure. Finally, critical commentary on the Shuttleworth equation corrects misconceptions and contributes to a comprehensive understanding of interfacial thermodynamics.

Abstract – Nederlandse versie

Deze thesis is een onderzoek naar de complexe interactie tussen beperking en materiaalgedrag en behandelt cutting-edge onderwerpen in nanomechanica en interfaciale fysica. Elke sectie verkent hoe beperking de materiaaleigenschappen aanzienlijk verandert in vergelijking met hun massa-tegenhangers, en breidt het onderzoek uit naar het genuanceerde domein van thermodynamische eigenschappen aan interfaces.

We demonstreren eerst het falen van een eerder erkende universele aspectverhouding (hoogte versus diameter) in nanometer-grote bubbels binnen grafenen, wat de basis legt voor een gedetailleerde analyse van hechtenergieën. Verder onthult de indrukking van grafeennanobubbels falingspunten die doen denken aan virale schillen door middel van analyse met het dimensionale Föppl–von Kármán (FvK) getal. Daarnaast onderzoeken we faseovergangen van ingekapselde edelgassen, die intrigerend gedrag vertonen onder variërende temperaturen.

De vorming van anomale vormen in platte nanobubbels ingekapseld door hexagonaal boornitride wordt eveneens onderzocht, waarbij de invloed van verwarmingssnelheden en waterstofbruggen wordt benadrukt. De kation-gecontroleerde permeatie van geladen polymeren door nano-capillairen wordt bestudeerd, waarbij specifieke effecten van monovalente kationen op de transmissiesnelheid van polymeren worden onthuld. De mogelijkheid om permeatie te manipuleren wordt verhelderd op basis van de verschillende oppervlakte- versus bulkvoorkeuren van verschillende alkali-kationen in de aanwezigheid van een extern elektrisch veld, wat waardevolle inzichten biedt in de interactie tussen ionendynamica en nano-beperkingseffecten.

Het onderzoek gaat verder met een beoordeling van de nauwkeurigheid van de Kelvinvergelijking in nanoschaal-capillairen, waarbij een revisie wordt voorgesteld op basis van disjunctiedruk. Ten slotte biedt een kritische commentaar op de Shuttleworth-vergelijking correcties voor misvattingen en draagt bij aan een alomvattend begrip van interfaciale thermodynamica.

Contents

Chapter 1

Introduction

In the landscape of contemporary scientific inquiry, nanoscience stands as a transformative force, reshaping the boundaries of what is conceivable and propelling innovation across disciplines. At the heart of this revolution is nanomechanics, a field focused on unraveling the mechanical intricacies of materials at the nanoscale. The significance of nanoscience and nanomechanics resonates across diverse realms of application, from materials engineering to biomedical sciences. The ability to manipulate and understand materials at the atomic and molecular levels opens avenues for groundbreaking technologies, fostering the development of advanced materials with tailored properties and the creation of nanoscale devices with unprecedented functionalities [1–11]. As researchers navigate this intricate terrain, the quest for understanding the mechanical behaviors of materials at the nanoscale not only deepens our fundamental knowledge but also holds the promise of revolutionary advancements in materials design, healthcare, and electronics, making nanoscience a driving force in the forefront of contemporary research and technological progress [12–18].

In the intricate landscape of nanoscience, confinement stands out as a pivotal factor shaping the properties and behaviors of materials at the nanoscale. This phenomenon introduces a paradigm shift, where spatial restrictions give rise to novel phenomena and behaviors distinct from the bulk characteristics of materials. Whether manifested in nanoscale structures or in the nuanced responses of materials to confinement, this spatial limit becomes a critical lens unveiling the intricacies of material behaviors in restricted spaces [19]. This emphasis on confinement is not purely theoretical; it resonates with the practical challenges and opportunities in nanotechnological applications. From miniaturized electronic components to advancements in targeted drug delivery systems, the impact of confinement governs the performance and functionality of nanoscale systems [20–24].

The importance of interface phenomena becomes particularly pronounced when grappling with systems characterized by a substantial surface-to-volume ratio, as is the case in nanoscale confinements [25]. In such confined spaces, the interfacial region becomes a dominant player, governing material behaviors and dictating the performance of nanomaterials. The heightened significance of interfaces in confined systems is underscored by their potential to dictate mechanical, thermodynamic, and chemical interactions [26–33]. Therefore, understanding and manipulating these interface-driven phenomena become imperative for tailoring materials to meet specific requirements in nanotechnology applications.

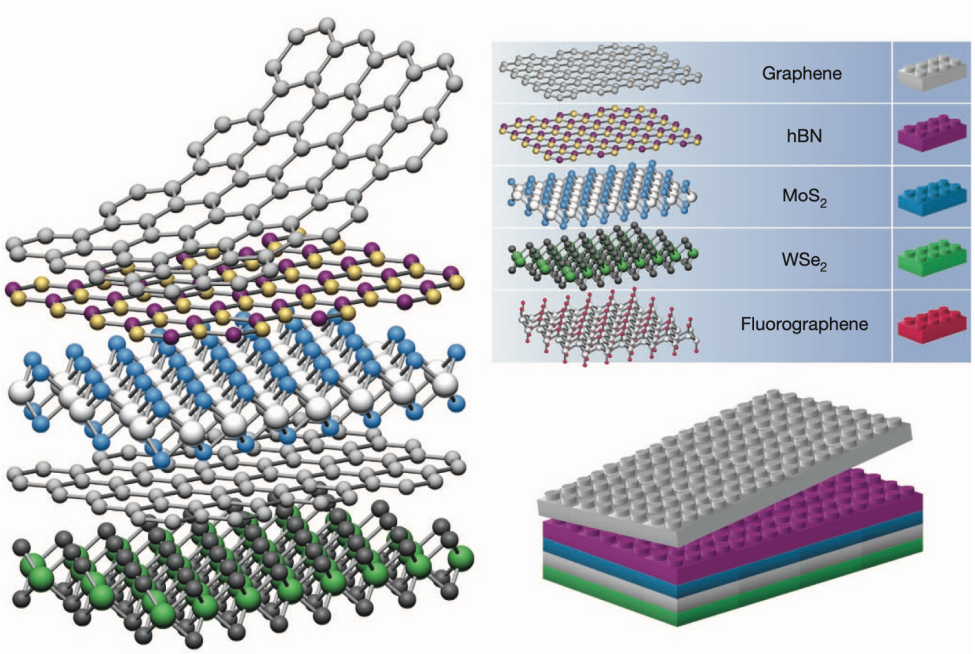

Figure 1.1: If one considers 2D crystals to be analogous to Lego blocks (right panel), the construction of a huge variety of layered structures becomes possible. Conceptually, this atomic-scale Lego resembles molecular beam epitaxy but employs different 'construction' rules and a distinct set of materials. This image and caption are sourced from ref. 23.

A noteworthy development in the exploration of nanoscale confinement lies in the emergence of two-dimensional (2D) van der Waals (vdW) heterostructures, with graphene prominently standing at the forefront [23]. These heterostructures, composed of atomically thin layers stacked atop one another (Fig. 1.1), offer a unique platform for creating well-defined boundaries in confined systems [34]. Graphene, owing to its exceptional mechanical strength and electrical conductivity, serves as an exemplary building block for constructing these boundaries [35–40]. The precise layering of diverse 2D materials introduces tailored properties and functionalities, further accentuating the confinement effects within the created nanoenvironments. As these heterostructures become the focal point of investigation, their potential as boundaries in confinements opens avenues for manipulating material behaviors at the nanoscale.

Despite the precision achieved in the synthesis of 2D sheets stacked at interfaces, the presence of impurities has proven to be an inherent challenge in this advanced process. The synthesis of these atomic layers is susceptible to the infiltration of foreign particles, gases, or defects, which inevitably become trapped between the 2D sheets during their assembly [34]. The entrapment of impurities within the layers poses a critical consideration, as it can influence the electronic, mechanical, and thermal properties of the resulting van der Waals (vdW) heterostructures.

Once considered a signature of robust adhesion and assembly [41], the phenomenon of trapped impurities manifesting as bubbles within 2D materials has undergone a trans-

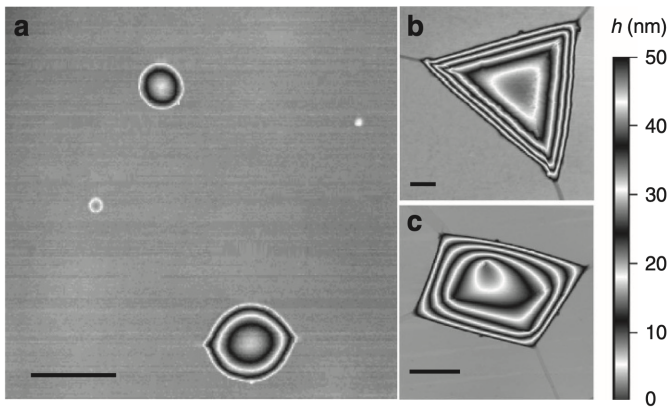

Figure 1.2: Atomic force microscope (AFM) images of graphene bubbles of different shapes. Scale bars, 500 nm (a); 100 nm (b); 500 nm (c). The vertical scale on the right indicates the height of the bubbles. This image and caption are sourced from ref. 52.

formative shift in perception. Fig. 1.2 displays atomic force microscope (AFM) images of example bubbles formed by 2D sheets. Far from being merely artifacts, these bubbles have evolved into powerful tools with diverse applications. They serve as unique probes for studying the elastic properties of the involved 2D crystals [37]. Additionally, the evaluation of conditions that nanoscale confinement exerts on the enclosed materials has become a focal point of research, leveraging these impurity-induced bubbles as observable markers. Examples range from the encapsulation of water inside graphene nanocapillaries [42–44] to the confinement of nanocrystals or biological molecules within graphene liquid cells [45–48]. Further, the study extends to room-temperature ice confined in a 2D nanochannel [49, 50] and the use of a hydrothermal anvil made of graphene on diamond [51], showcasing the versatility of impurity-induced bubbles as valuable tools in probing and manipulating materials at the nanoscale.

The meticulous study of the morphology of impurity-induced bubbles within 2D materials stands as a crucial endeavor, shedding light on fundamental aspects of nanoscale confinement [52, 53]. Through a combination of analytical membrane theory [54, 55] and experimental investigations, researchers have discerned that the shape of these bubbles adheres to a universal aspect ratio between height and radius (Fig. 1.3) [52]. This revelation carries profound implications, as it not only enhances our understanding of the underlying mechanics governing bubble formation but also provides a valuable benchmark for interpreting and predicting bubble morphologies in diverse 2D material systems.

Despite the established understanding of a universal aspect ratio governing the morphology of impurity-induced bubbles, a groundbreaking revelation emerges through the synergy of scanning tunneling microscopy (STM) and molecular dynamics simulation. This collaborative exploration, conducted in partnership with the group of Prof. Lino da Costa Pereira at KU Leuven, has unveiled a notable breakdown in the universal aspect ratio, particularly in the shaping of very small bubbles with radii less than 1 nm. The intricacies of this deviation have been systematically investigated in chapter 3 of this

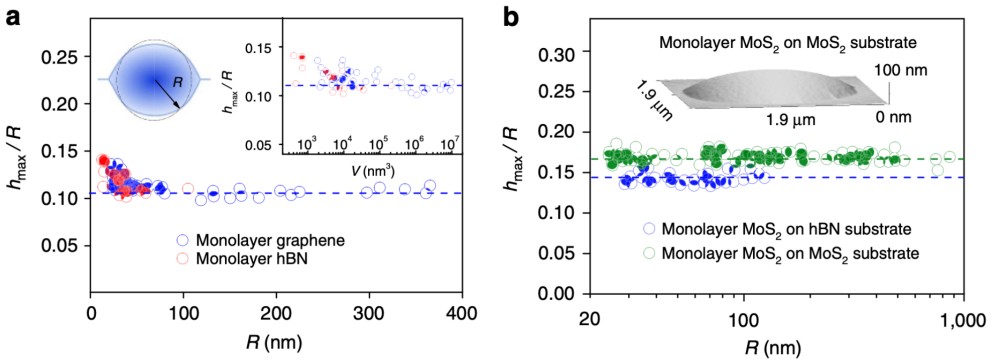

Figure 1.3: (a) Measured aspect ratios as a function of the base radius for graphene (blue symbols) and monolayer hexaghonal boron-nitride (hBN) (red symbols). Dashed line shows the mean value. Top left inset: sketch of a nearly round bubble and its effective radius R determined as $R = \sqrt{A/\pi}$, where A is the measured area of the base of the bubble. Right inset: aspect ratio of the bubbles as a function of their volume. (b) Aspect ratio of MoS_2 bubbles on hBN and MoS_2 substrates. Dashed lines show the mean values of $h_{max}/R = 0.14$ and 0.17, respectively. The logarithmic scale is used to accommodate the large range of R. Inset: AFM image of a typical MoS_2 bubble. This image and caption are sourced from ref. 52.

thesis. The breakdown in the universal aspect ratio is attributed to the out-of-plane settlements of trapped elements within these diminutive bubbles, coupled with the atomic compressibility of the confined materials [56].

Nanoindentation, a powerful technique in the realm of nanoscience, serves as a sophisticated tool for probing and characterizing the mechanical properties of materials at the nanoscale [37, 57]. This method involves the controlled application of a precisely defined force onto a nanometer-sized indenter, often a sharp tip or pyramid, creating localized deformations on the material surface. In the context of nanobubbles within two-dimensional (2D) sheets, by measuring the resulting load-displacement curve, valuable information about hardness, elastic modulus, and the hydrostatic pressures of the confined matter can be extracted with exceptional precision.

While nanoindentation offers invaluable insights into the mechanical properties of nanobubbles and 2D sheets, the prospect of membrane failure, or rupture, looms as a critical consideration, drawing parallels with observations from indenting viral shells. High indentation forces, while informative in probing the robustness of materials, can lead to structural failures in membranes. This concern is particularly relevant in the context of nanobubbles within 2D sheets, where the delicate balance between probing mechanical properties and avoiding rupture becomes paramount.

In the investigation of membrane response to nanoindentation, the applicability of the elasticity theory of thin shells, proves to be a cornerstone. The advantages of this theory lie in its ability to capture the intricate interplay between forces, deformations, and material properties. Using molecular dynamics simulation, we reveal the applicability of

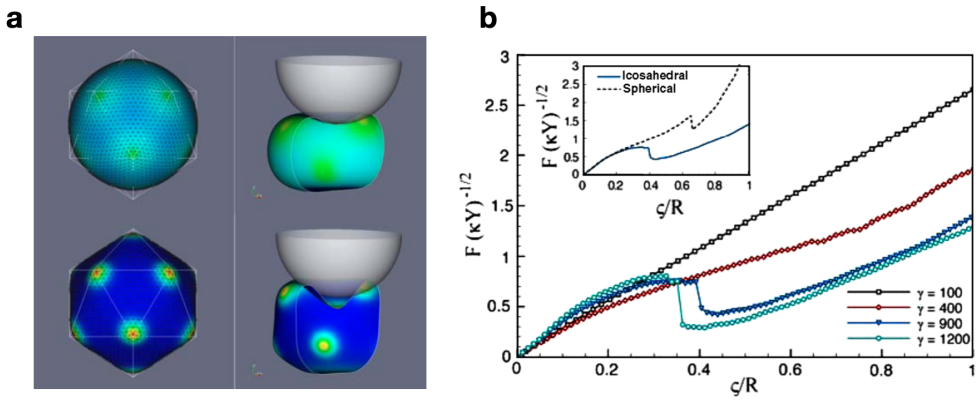

Figure 1.4: (a) Shapes of icosahedral shells under external force calculated numerically by finite-element analysis with FvK numbers $\gamma = 100$ (top) and $\gamma = 1200$ (bottom). (b) Force-indentation curves of an icosahedral shell with isotropic elastic properties deformed by a spherical tip. The force F and the indentation (i.e., the reduction in diameter along the indenting axis) ζ are expressed in dimensionless units, with R the equivalent radius of shell and tip, Y the two-dimensional Young's modulus, and κ the bending modulus. The dimensionless control parameter $\gamma = YR^2/\kappa$ determines whether the curve has a snap-through discontinuity. The inset compares the force-indentation curves of spherical and icosahedral shells with $\gamma = 900$. This image and caption are sourced from ref. 58.

the Föppl–von Kármán (FvK) dimensionless number within the context of the elasticity theory of thin shells as a predictive tool for discerning the failure points of graphene nanobubbles [59]. The FvK number is defined as YR^2/κ, where Y and κ represent the Young's modulus and bending stiffness of the membrane, respectively, and R denotes its radius of curvature. Mirroring the observed failure mechanisms in viral shells under indentation (Fig. 1.4) [58], the FvK dimensionless number proves instrumental in forecasting the points at which these nanobubbles succumb to external forces. This groundbreaking revelation is meticulously examined and expounded upon in chapter 4 of this thesis. Additionally, in chapter 4, a critical facet of our investigation delves into the aggregation properties of the elements confined within nanobubbles, revealing deviations from their bulk phase diagrams.

In recent experiments conducted by the group of Prof. Irina Grigorieva at the University of Manchester, an intriguing anomaly in the realm of bubble shapes has surfaced. This anomaly takes the form of flat Iceland shapes observed within bubbles created in hexagonal boron nitride (hBN) sheets. Chapter 5 of this thesis delves into the exploration of these unique bubbles, unraveling the intricate influence of hydrogen bonds. The presence of hydrogen bonds between the hydrogen atoms of trapped substances—whether water or hydrocarbon molecules—and the nitride acceptors of the hBN membranes proves to be a decisive factor shaping these special bubble morphologies. The study not only highlights the specific role of hydrogen bonding but also brings to light the highly irregular nature of the morphologies exhibited by bubbles within hBN sheets.

Contrary to the conventional perception of impurities as undesirable elements, there are instances where their intentional introduction serves strategic purposes. One notable

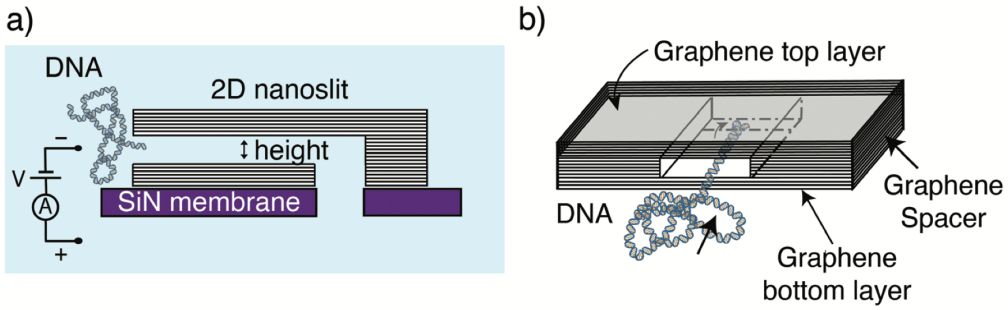

Figure 1.5: DNA translocation through 2D-nanoslit devices. a) Cross-sectional view of a 2D-nanoslit device in the DNA translocation setup. DNA is introduced from the cis (negatively biased) side and a positive voltage is applied to drive the DNA through the slit. b) Oblique-view schematic of the 2D nanoslit. The device is made by sandwiching graphene spacers between top and bottom layers of graphite crystals to form an atomically smooth surface within the slit. The graphene spacer defines the height of the device to an accuracy of a single layer—0.34 nm. The entire graphene crystal was then masked and etched perpendicularly to define the length of the slit. The final device geometry was $w = 110$ nm, $h = 6.5$ nm, $l = 400$ nm. This image and caption are sourced from ref. 60.

application lies in the intentional incorporation of impurities, such as macromolecules or other biomolecules, within nanocapillaries (Fig. 1.5)[22, 60–63]. This deliberate placement serves dual purposes: first, it facilitates high-resolution imaging of these macromolecules, enabling researchers to glean detailed insights into their structures and interactions. Second, the controlled presence of impurities within nanocapillaries serves as a means for aligning large biomolecules, capitalizing on the confined environment to influence their orientation.

The ability to precisely control the speed of permeation of large molecules within nanocapillaries stands as a critical factor. This level of control allows researchers to manipulate the transport kinetics of large molecules, influencing the rate at which they traverse the confined spaces of nanocapillaries. Building upon prior experiments that elucidated the role of various alkali cations in modulating the speed of DNA passage through nanopores of approximately 15 nm (Fig. 1.6) [64], our investigation takes a fresh perspective in the context of charged polymers navigating through nanocapillaries below 2 nm [65]. Remarkably, our findings reveal a parallel yet distinct trend in the permeation behavior of charged polymers compared to DNA. The observed discrepancy in permeation trends can be traced back to two primary sources. Firstly, the remarkably slim nature of these nanocapillaries enhances the hydrodynamic drag force experienced by macromolecules, creating a pronounced effect on their transit dynamics. This heightened drag force becomes a dominant factor in dictating the permeation behavior, particularly in comparison to larger nanocapillaries. Secondly, the solvation dynamics of alkali cations play a pivotal role, differing significantly in the confined space of sub-2 nm nanocapillaries compared to the bulk water environment. The altered solvation of alkali cations within small water clusters exerts a distinctive influence on the overall ion dynamics, thereby affecting the permeation characteristics of charged polymers. This dual origin of divergent trends, thoroughly investigated in chapter 6, contributes to a comprehen-

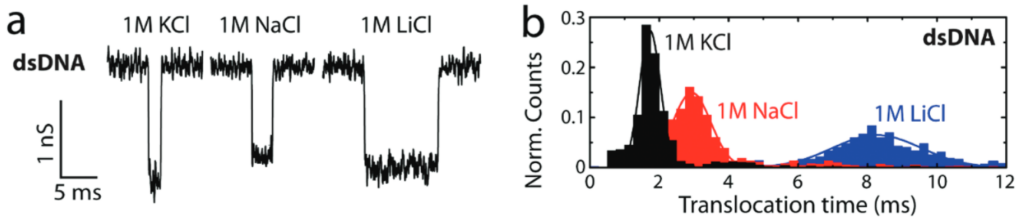

Figure 1.6: Experiments showing the slowing down of DNA translocation in LiCl. (a) Example current recordings for 48.5 kbp λ-dsDNA filtered at 5 kHz in 1 M KCl (left), 1 M NaCl (middle), and 1 M LiCl (right). (b) Translocation time histograms corresponding to (a). This image and caption are sourced from ref. 64.

sive understanding of the intricate interplay between hydrodynamics, ion solvation, and nanoscale confinement effects on macromolecular permeation.

The solvation dynamics of ions within small water clusters, comprising fewer than 250 water molecules, introduces a fascinating realm of complexity. Historically, the literature has delved into the surface versus bulk preference of different cations and anions in water, often presenting contentious issues [66–69]. However, the preferences in the presence of an external electric field, a driving force for our charged macromolecules, have remained elusive. Chapter 6 also embarks on a thorough exploration, shedding light on the nuanced behaviors of cations in small water clusters under the influence of external electric fields.

In the presence of a narrow, open-ended capillary tube submerged in a liquid container, a familiar phenomenon occurs—capillary rise or fall. This behavior is characterized by the liquid within the tube reaching a level distinct from the liquid surface in the container. The disparity in height is intricately governed by a balance between the weight of the liquid column and the force exerted by capillary pressure. The capillary pressure, a crucial factor in this equilibrium, signifies the pressure difference across the interface of the liquid and its vapor above. It is this pressure difference that dictates the elevation or descent of the liquid within the capillary tube. When capillary pressure is precisely matched with the gravitational force acting on the liquid column, a stable position is attained, leading to capillary equilibrium.

However, when we venture into experiments at the nanoscale, where the dimensions are comparable to molecular distances, the classical force balance governing capillary rise or fall encounters new considerations. At this level, the familiar equilibrium between the weight of the liquid column and capillary pressure must be reevaluated to include the difference in vapor pressure between the surface of the container and the surface of the tube. Unlike macroscopic devices where this pressure difference is typically negligible, at the nanoscale, molecular interactions and surface effects become prominent. The pressure difference, akin to the variation in atmospheric pressure with altitude, must now be considered in the force balance equation.

In 1870, the renowned physicist William Thomson, later known as Lord Kelvin, made a significant contribution by deriving an analytical expression for the vapor pressure over a liquid meniscus. Grounded in macroscopic thermodynamic homogeneity, Lord Kelvin's

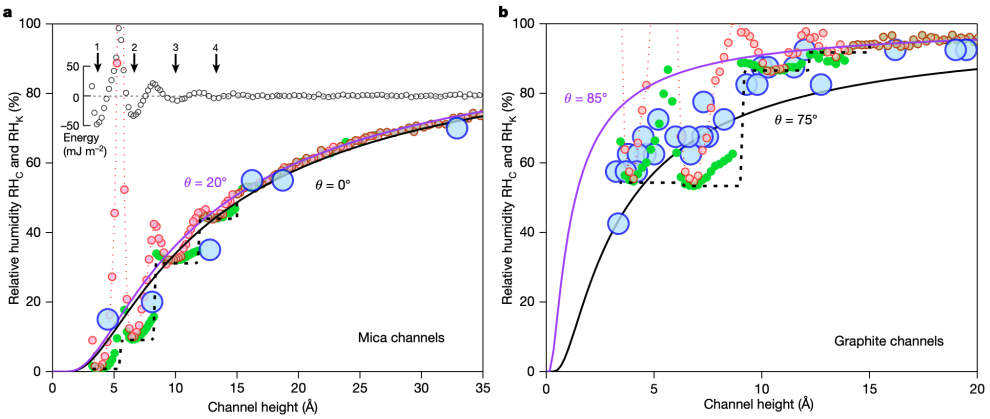

Figure 1.7: (a) Relative humidity RH_C required for water condensation in mica channels of different heights h. Blue circles indicate experimental observations. Two solid curves indicate RH_K given by Kelvin equation with bulk water's characteristics for the range of possible θ for mica (colour-coded). Inset: molecular dynamics calculations for changes in γ_{sl} caused by restructuring of water inside 2D channels. Red symbols are the expected behaviour calculated using the oscillating γ_s shown in the upper curve. Black dashed curve, same analysis but assuming fully flexible capillary walls allowing relaxation into the energy minima at commensurate h. Green filled circles, same analysis but for a finite rigidity of the confining walls. (b) Same as (a), but for graphite capillaries. This image and caption are sourced from ref. 70.

work provided a fundamental insight into the conditions that initiate the spontaneous condensation of vapor above the liquid meniscus. This derived expression, now widely recognized as the Kelvin equation, captures the delicate equilibrium between the liquid and vapor phases. The Kelvin equation predicts the relative humidity at which capillary condensation occurs as $RH_K = \exp\left(\frac{-2\sigma}{k_B T \rho_N d}\right)$, where σ is the liquid surface tension, T is temperature, ρ_N is the number density of liquid, k_B is the Boltzmann constant, and d is the diameter of the meniscus curvature.

Recent experiments have yielded surprising results regarding the Kelvin equation, originally formulated under specific assumptions derived from macroscopic thermodynamics. Contrary to expectations, the equation has demonstrated resilience beyond its initially envisaged applicability range, particularly in nanoscale capillaries (Fig. 1.7) [70]. The current understanding of this phenomenon attributes it to the oscillatory behavior of the solid-liquid interfacial free energy [70]. However, in chapter 7 of this thesis, we delve into the intricacies of this explanation, revealing thermodynamic and capillarity inconsistencies. Through a careful revision of the Kelvin equation, we propose a different hypothesis, ascribing its validity in nanoscale confinement to the influence of disjoining pressure.

Disjoining pressure is a fundamental concept in interfacial thermodynamics, playing a pivotal role in understanding the behavior of confined fluids and thin films [71, 72]. Emerging as a deviation from equilibrium pressure due to intermolecular interactions at the interface between two phases, disjoining pressure becomes particularly pronounced in systems where the distance between interfaces approaches molecular dimensions.

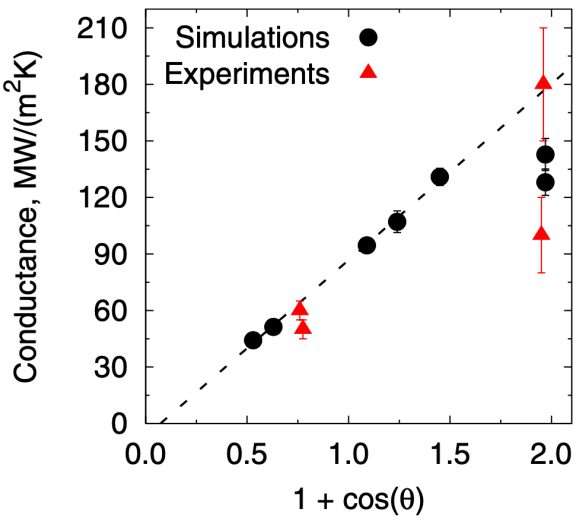

Figure 1.8: Interfacial thermal conductance as a function of work of adhesion [$\sim 1 + cos(\theta)$]. Simulations results (circles) are in good agreement with experimental data [74] (triangles) and show the direct proportionality of interfacial thermal conductance to the work of adhesion. This image and caption are sourced from ref. 75.

This phenomenon is governed by a delicate balance of forces, including van der Waals attractions, electrostatic interactions, steric effects, and solvation forces. The confinement geometry and curvature of the interface heavily influence the magnitude and distribution of disjoining pressure, ultimately dictating the stability and dynamics of thin liquid films, bubbles, droplets, and other confined systems [73].

To substantiate our hypothesis, we perform extensive calculations on wetting properties and interfacial heat transfer. Specifically, we calculate the free energy change of the system resulting from the separation of two materials at their interface, a quantity known as the work of adhesion. Additionally, we calculate the interfacial thermal conductance, referred to as the Kapitza conductance, which arises from differences in electronic and vibrational properties between materials. This conductance occurs when an energy carrier (phonon or electron, depending on the material) traverses the interface. While it is previously acknowledged that the work of adhesion and Kapitza conductance are directly proportional (Fig. 1.8) [75], our investigation within nanocapillaries reveals a breakdown in this proportionality due to confinement effects. Specifically, we find that in nanocapillaries, the work of adhesion is more influenced by entropy than energy.

Surface free energy and surface tension are often considered equivalent when studying the surfaces of liquids. However, this equivalence does not extend to solids, leading to common confusion between the two concepts [76]. In 1950, Shuttleworth introduced an equation to describe the relationship between these quantities [77]. The Shuttleworth equation reads $\gamma = F + A\left(\frac{\partial F}{\partial A}\right)$, where A is surface area, γ is surface tension and F is surface free energy per unit area. Since then, a considerable amount of scientific discussion and debate has taken place in the literature, both in support [78–82] and criticism [83–88] of

the Shuttleworth equation, particularly regarding its derivation and its alignment with Hermann's mathematical structure of thermodynamics. In chapter 8 of this thesis, we offer a critical commentary on these debates, aiming to provide clarity and insight into the ongoing discourse surrounding the Shuttleworth equation and its implications in surface science.

Overall, this thesis delves into cutting-edge scientific inquiries in nanoscience, focusing on instances where confinement significantly influences the material properties and interfacial thermodynamics. Our findings underscore the necessity of abandoning presumptions based on macroscopic physical laws or equations for a thorough understanding of phenomena at the nanoscale. Instead, meticulous fundamental derivations are imperative. While this research marks a significant stride forward, it is not the final destination. Future research endeavors will address substantial scientific gaps, such as exploring interfacial free energies and the role of entropy in nanobubble systems, an area notably overlooked in existing literature. Additionally, investigations into thermal resistance at interfaces within nanobubbles and the evaluation of solid-vapor interfacial free energy, a contentious concept, remain essential for advancing our understanding of nanoscale phenomena.

Chapter 2

Methodological Framework

Molecular dynamics simulation serves as the primary tool utilized in this thesis. Within this chapter, we aim to provide a concise overview of this computational technique. Beginning with a summary of classical mechanics, we explore the fundamentals of molecular dynamics. Additionally, we offer a succinct introduction to equilibrium statistical mechanics, crucial for connecting the observable thermodynamic properties of the systems under investigation with their microscopic behaviors simulated through molecular dynamics. It is important to note that achieving a comprehensive understanding of molecular dynamics and statistical mechanics extends beyond the scope of a single chapter. The content presented in this chapter draws from "Statistical Mechanics: Theory and Molecular Simulation" by Mark E. Tuckerman, published by Oxford University Press in 2010. Interested readers are encouraged to consult this reference or similar literature covering relevant topics.

2.1 Classical mechanics

Isaac Newton introduced his renowned equations of motion in the 17^{th} century, which subsequently formed the foundation of classical mechanics.

Newton's first law of motion, often referred to as the law of inertia, establishes that an object will persist in its state of rest or uniform motion in a straight line unless acted upon by an external force. This principle asserts that the natural tendency of an object is to maintain its current state of motion, whether stationary or moving with constant velocity.

Newton's second law of motion quantifies the relationship between force, mass, and acceleration. It states that the acceleration of an object is directly proportional to the net force acting on it and inversely proportional to its mass. Mathematically, it is articulated as $\Sigma F = ma$, where ΣF represents the net force, m denotes the mass of the object, and a signifies its acceleration. This law provides a precise means of predicting the acceleration of an object when subjected to known forces and possessing a defined mass. When there is no net force acting on an object ($F = 0$), according to the second law, its acceleration (a) is also zero. This implies that the object will either remain at rest or continue its uniform motion, in line with the principle of inertia described in the first law. Thus, Newton's first law is encompassed within the broader framework of the second law.

Newton's third law of motion asserts that for every action, there exists an equal and opposite reaction. In essence, when one object exerts a force on another, the second object exerts a force of equal magnitude but in the opposite direction on the first object.

Together, these three laws form the cornerstone of classical mechanics, underpinning our understanding of motion and dynamics across various disciplines. They serve as foundational principles for analyzing and predicting the behavior of physical systems. Specifically, Newton's second law enables the prediction and understanding of various phenomena, with applications in fields as diverse as engineering, biomechanics, materials science, and more. In essence, Newton's second law offers a fundamental framework for analyzing and comprehending the dynamics of the physical world at various scales.

Newton's second law, being a second-order differential equation, necessitates two initial conditions for accurate prediction of subsequent motion. These initial conditions encompass both the object's initial positions and velocities. With this information and the forces acting on the system, one can use Newton's second law to determine the object's motion at any point in time.

However, in the study of real-world systems such as biological tissues, granular materials, or turbulent flows, solving Newton's second law analytically for each particle's constituents becomes impractical due to the enormous number of particles and computational complexity. Additionally, the nonlinear nature of forces in such systems further complicates analytical solutions. Consequently, numerical methods are indispensable for accurately studying the dynamics of these systems.

Numerically solving Newton's second law for each particle of the system is known as molecular dynamics (MD). This technique involves discretizing Newton's equations of motion and integrating them numerically to track the positions and velocities of atoms or molecules in a system over time. However, is such microscopic information—positions and velocities of all particles—of interest for scientists? Indeed, practical thermodynamic quantities such as pressure and temperature often take precedence for scientists over tracking the exact dynamics of all particles within a system. The bridge between the microscopic dynamics of individual particles and the macroscopic thermodynamic quantities of interest is provided by a branch of science known as statistical mechanics.

In this chapter, we offer a concise introduction to the fundamental concepts of classical statistical mechanics and molecular dynamics. These disciplines serve as the cornerstone of the research conducted in this thesis, laying the groundwork for the discussions and analyses presented in the subsequent chapters.

2.2 Molecular dynamics

Molecular dynamics offers a computational platform akin to a *virtual laboratory*, enabling numerous numerical experiments that mimic real physical or chemical systems to a certain degree. This approach facilitates the manipulation of control parameters to conduct successive experiments easily. Furthermore, it allows the creation of extreme conditions, such as high temperature and pressure, in a straightforward and safer manner. However, the accuracy of the results is contingent upon the fidelity of the numerical model. Addi-

tionally, there is a risk of introducing artificial bias if the molecular dynamics simulation fails to adequately sample a sufficient number of microstates within the allotted time.

The Fermi–Pasta–Ulam calculation of 1955 stands out as one of the earliest instances of such a numerical thought experiment. In this study, the equations of motion for a one-dimensional chain of nonlinear oscillators were numerically integrated to assess the degree of ergodicity—defined in the following sections—and energy equipartitioning within the system. Subsequently, Alder and Wainwright conducted the pioneering condensed-phase molecular dynamics calculation on a hard-sphere system in 1957 and 1959, revealing the existence of a solid–liquid phase transition.

Building on this work, Rahman and Verlet performed simulations using a realistic continuous potential for systems comprising 864 argon atoms in 1964 and 1967, respectively. Another significant advancement occurred when Berne and colleagues investigated molecular dynamics simulations of diatomic liquids, exploring the time dependence of molecular reorientation in these systems through various studies conducted between 1968 and 1971.

Following these endeavors, Stillinger and Rahman conducted pioneering molecular dynamics simulations of liquid water in 1971, 1972, and 1974. Shortly thereafter, Karplus and his team reported the first molecular dynamics calculations of proteins in 1976 and 1977. The explicit treatment of molecular systems was made possible by the development of techniques for maintaining specific bonding patterns, either through stiff intramolecular forces or by imposing holonomic constraints into the simulation.

The field of molecular dynamics has greatly benefited from advancements in high-performance computing. While the original Alder and Wainwright calculations necessitated the use of a *supercomputer* at Lawrence Livermore National Laboratory in California, such as the UNIVAC system, modern molecular dynamics simulations with force fields can be conducted on desktop computers. However, a significant milestone in molecular dynamics, known as ab initio or first-principles molecular dynamics, as introduced by Car and Parrinello in 1985, currently relies on large-scale high-performance supercomputing resources.

In ab initio molecular dynamics calculations, interatomic interactions are computed directly from the electronic structure *on the fly* as the simulation progresses, enabling explicit treatment of chemical bonding breaking and forming events. The computational overhead associated with solving the electronic Schrödinger equation using commonly employed approximation schemes is substantial, necessitating the use of these resources.

The field of molecular dynamics is dynamic and rapidly evolving, with the immediate availability of free software packages capable of conducting various types of molecular dynamics calculations significantly expanding the user base of this methodology.

2.3 Numerical methods for solving Newton's equations of motion

By utilizing numerical methods, one can discretize the continuous equations of motion and integrate them numerically to predict the behavior of dynamical systems over time. Some commonly used numerical methods for solving Newton's equations, which we will elaborate on in subsequent sections, include: the Euler method, the Runge-Kutta method, the Leapfrog method, the Verlet method, and the Velocity Verlet method. All these methods fall under the category of finite-difference methods (FDM), which approximate derivatives in ordinary differential equations (ODEs) or partial differential equations (PDEs) using finite differences.

2.3.1 Euler method

The Euler Method is expressed as $y_{n+1} = y_n + h \cdot f(t_n, y_n)$, where y_n is the approximate value of the solution at time t_n. h is the step size. $f(t_n, y_n)$ is the derivative of y with respect to t evaluated at t_n and y_n.

This method involves iteratively updating the approximate solution y_n at each time step t_n by adding the product of the step size h and the derivative of y with respect to t at t_n and y_n.

For Newton's equations of motion, which typically involve second-order ODEs, the Euler Method can be applied by first converting them into a system of first-order ODEs.

Newton's second law can be expressed as a first-order ODE for velocity (v): $\frac{dv}{dt} = \frac{F}{m}$. Additionally, the velocity v is related to the particle's position (x) by another first-order ODE: $\frac{dx}{dt} = v$.

Now, applying the Euler Method to this system involves discretizing time into small steps (h) and updating the velocity and position at each step: $v_{n+1} = v_n + h \cdot \frac{F}{m}$ and $x_{n+1} = x_n + h \cdot v_n$.

These equations allow us to numerically approximate the velocity and position of the particle at each time step n, providing a solution to Newton's equations of motion under the given force F. In molecular dynamics, the step size used for numerical integration is commonly referred to as the *time step*, typically denoted by Δt.

2.3.2 Runge-Kutta method

Runge-Kutta methods are a family of numerical techniques used for solving ODEs. One of the most widely used Runge-Kutta methods is the fourth-order Runge-Kutta method (RK4). RK4 involves four intermediate steps to approximate the solution at each step. It evaluates the derivative of the solution function at various points within the time interval, combining these derivatives to obtain a weighted average that gives a more accurate estimate of the solution.

The general form of the fourth-order Runge-Kutta method for solving the initial value problem $\frac{dy}{dt} = f(t, y)$ with initial condition $y(t_0) = y_0$ is:

Step 1. Estimating the slope at the initial point: $k_1 = \Delta t \cdot f(t_n, y_n)$.

Step 2. Estimating the slope at the midpoint of the interval, using k_1 as an estimate: $k_2 = \Delta t \cdot f(t_n + \frac{h}{2}, y_n + \frac{k_1}{2})$.

Step 3. Repeating step 2, but now using k_2 as an estimate: $k_3 = \Delta t \cdot f(t_n + \frac{h}{2}, y_n + \frac{k_2}{2})$.

Step 4. Estimating the slope at the end of the interval, using k_3 as an estimate: $k_4 = \Delta t \cdot f(t_n + h, y_n + k_3)$.

Step 5. Combining the slopes to obtain the weighted average: $y_{n+1} = y_n + \frac{1}{6}(k_1 + 2k_2 + 2k_3 + k_4)$.

Newton's equations of motion can be represented as a system of first-order ODEs (see above). Now, applying the fourth-order Runge-Kutta method (RK4) involves updating the velocity and position of the particle at each time step using a weighted average of four intermediate slopes.

This process is iterated over each time step to approximate the particle's trajectory over time, providing a numerical solution to Newton's equations of motion.

2.3.3 Leapfrog method

Unlike the Euler method, which updates positions and velocities at the same time step, the Leapfrog method employs a staggered approach, updating positions and velocities alternately. The basic algorithm of the leapfrog method for solving ODEs can be summarized as follows:

Step 1. Updating velocities to $v_{1/2} = v_0 + \frac{1}{2}a(x_0)\Delta t$, where $a(x_0)$ is the acceleration at x_0 and Δt is the step size.

Step 2. Updating positions to $x_1 = x_0 + v_{1/2}\Delta t$.

Step 3. Updating velocities to $v_1 = v_{1/2} + \frac{1}{2}a(x_1)\Delta t$, where $a(x_1)$ is the acceleration at x_1.

It continues the process for each step until reaching the desired endpoint. To apply the leapfrog method to solve Newton's equations of motion, we first need to rewrite them as a system of first-order ODEs (see above), followed by its discretization protocol to predict the positions and velocities of particles over time.

2.3.4 Verlet and Velocity Verlet methods

The Verlet method is a widely utilized approach for its simplicity and efficiency in integrating equations of motion. The Verlet method updates particle positions and velocities at discrete time steps, relying on their Taylor series expansion of the current

states and accelerations. The position of a particle at time $t + \Delta t$ is computed as $x_{t+\Delta t} = x_t + v_t \cdot \Delta t + \frac{1}{2} a_t \cdot \Delta t^2$.

Simultaneously, the velocity is updated as $v_{t+\Delta t} = v_t + \frac{a_t + a_{t+\Delta t}}{2} \cdot \Delta t$. This equation adjusts the velocity for the next time step based on the current acceleration and the average acceleration over the time interval Δt.

While the Verlet algorithm's simplicity is attractive, it lacks explicit velocity evolution, which can be considered somewhat less refined. Expanding upon the Verlet method, the Velocity Verlet method offers enhanced accuracy and stability by explicitly updating both positions and velocities. In this method, the velocity is first updated at the midpoint of the time step: $v_{t+\frac{1}{2}\Delta t} = v_t + \frac{a_t}{2} \cdot \Delta t$.

Subsequently, the acceleration at the new position $x_{t+\Delta t}$ is computed. Finally, the velocity at the end of the time step is determined by combining the velocity at the midpoint with the average acceleration: $v_{t+\Delta t} = v_{t+\frac{1}{2}\Delta t} + \frac{a_t + a_{t+\Delta t}}{2} \cdot \Delta t$.

The Verlet and Velocity Verlet algorithms adhere to a critical property essential for the long-term stability of numerical solvers. The property is time-reversibility, which dictates that if we initialize the system with positions $r_1(t + \Delta t), ..., r_N(t + \Delta t)$ and velocities $v_1(t + \Delta t), ..., v_N(t + \Delta t)$, stepping backward in time by a duration of $-\Delta t$ should lead us back to the initial state $r_1(t), ..., r_N(t)$ and $v_1(t), ..., v_N(t)$. Time-reversibility reflects a fundamental symmetry of Newton's equations, which any numerical integrator should uphold.

2.4 Choosing the initial conditions

At this point, it is pertinent to discuss the selection process for initial conditions in molecular dynamics calculations. Establishing these conditions can pose a challenge, particularly depending on the system's complexity. For instance, in the case of a basic liquid, one approach might involve initializing coordinates resembling the solid phase of the substance and subsequently transitioning to a liquid state under appropriate thermodynamic conditions.

Alternatively, random initial coordinates can be employed, with a constraint on particle distance to mitigate strong repulsive forces initially. In molecular liquids, bond lengths and bend angles may be determined by holonomic constraints or set to equilibrium values. However, for more intricate systems like molecular crystals or biological macromolecules, initial coordinates are typically derived from experimental X-ray crystal structures available in databases such as the Cambridge Structure Database [89], the Inorganic Crystal Structure Database [90], or the Protein Data Bank [91].

Using experimental structures may necessitate providing missing data, such as the coordinates of hydrogen atoms unresolvable through experimentation. In the case of biological systems, it is often essential to immerse the macromolecule in a water bath. In this scenario, coordinates from a well-equilibrated pure water simulation may be employed. Following immersion, excess water molecules within a certain proximity to any atom in the macromolecule are removed, while retaining crystallographic waters bound

within the molecule. Subsequently, re-establishing equilibrium is imperative, typically involving energy adjustment to achieve a desired temperature and volume adjustment to maintain a specific pressure level.

After defining the initial coordinates, the next step is to establish the initial velocities. Typically, this involves drawing velocities from a Maxwell-Boltzmann distribution, ensuring that the velocities sampled adhere to any constraints placed on the system.

The Maxwell-Boltzmann distribution, described by the probability distribution function $f(v) = 4\pi \left(\frac{m}{2\pi kT}\right)^{3/2} v^2 e^{-\frac{mv^2}{2kT}}$, k being Boltzmann's constant, delineates the likelihood of particle velocities in a thermal system. This function elucidates the statistical nature of particle velocities, crucial for understanding gas diffusion, effusion, and equilibrium dynamics. Derived from kinetic theory, it provides a fundamental link between temperature T and the distribution of particle speeds v.

Once the initial conditions are defined, all the necessary information to commence a simulation is accessible, allowing for the utilization of one of the algorithms elaborated above like the Velocity Verlet algorithm to integrate the equations of motion.

2.5 Conservative and nonconservative forces

Newton's equations of motion can be reformulated into alternative frameworks known as Lagrangian and Hamiltonian mechanics, provided the forces acting on the system are conservative. Therefore, it is pertinent to distinguish between conservative and nonconservative forces before discussing these formulations.

In mechanics, conservative forces are distinguished by their property of conserving mechanical energy within a system. These forces exhibit path-independence, meaning that the work done by the force is solely dependent on the endpoints of the motion, regardless of the path taken. Mathematically, the work W done by a conservative force can be expressed as the negative change in potential energy ΔU: $W = -\Delta U$. Alternatively, it can be expressed as the negative line integral of the force over the path: $W = -\int_A^B \vec{F} \cdot d\vec{s}$, where $\vec{F}$ represents the conservative force, $d\vec{s}$ denotes an infinitesimal displacement vector, and A and B are the initial and final positions, respectively. Common examples of conservative forces include gravitational and electrostatic forces.

Conservative forces can be expressed as the gradient of a scalar field. The fundamental theorem of calculus for line integrals states that the line integral of a conservative vector field over a closed path is zero: $\oint_C \mathbf{F} \cdot d\mathbf{s} = 0$. Now, let us consider a closed path C and apply this theorem. Using the definition of conservative forces, we have: $\oint_C \mathbf{F} \cdot d\mathbf{s} = -\Delta U$.

Since this integral is zero for any closed path, it follows that $\Delta U = 0$ for any closed path. This implies that the change in potential energy U around any closed path is zero, which means that the potential energy U is constant throughout space. Therefore, we can define a scalar field U such that $\nabla U = \mathbf{F}$, and thus, conservative forces can indeed be expressed as the gradient of a scalar field.

On the other hand, nonconservative forces are characterized by their path-dependence,

where the work done depends on the specific path taken. For a nonconservative force, the work W is given by the line integral of the force over the path: $W = \int_A^B \vec{F} \cdot d\vec{s}$.

Nonconservative forces often lead to a dissipation of mechanical energy within the system. Frictional forces, such as air resistance or kinetic friction, are prominent examples of nonconservative forces. These forces result in the conversion of mechanical energy into other forms, such as heat or sound. When dealing with conservative forces, classical mechanics allows for the representation of the system's dynamics through equivalent formalisms known as Lagrangian and Hamiltonian mechanics. We will introduce these formalisms further in the following sections.

2.6 Lagrangian formulation of classical mechanics

In the Lagrangian formulation of mechanics, the dynamics of a system are described using the principle of least action, where the action functional S is minimized along the path of motion:

$$S = \int_{t_1}^{t_2} L(\mathbf{q}, \dot{\mathbf{q}}, t)\, dt \tag{2.1}$$

Here, L represents the Lagrangian function, which is the difference between the kinetic and potential energies of the system:

$$L(\mathbf{q}, \dot{\mathbf{q}}, t) = T(\mathbf{q}, \dot{\mathbf{q}}, t) - V(\mathbf{q}, t) \tag{2.2}$$

The Lagrangian depends on the generalized coordinates $\mathbf{q}$, their time derivatives $\dot{\mathbf{q}}$, and possibly time t. Through the principle of least action, the Euler-Lagrange equation is derived:

$$\frac{d}{dt}\left(\frac{\partial L}{\partial \dot{\mathbf{q}}}\right) - \frac{\partial L}{\partial \mathbf{q}} = 0 \tag{2.3}$$

These equations govern the evolution of the system's generalized coordinates $\mathbf{q}$ with respect to time t. By expressing the force term in Newton's second law of motion as the gradient of a scalar field (potential energy) and expanding the Euler-Lagrange equation, we can demonstrate the equivalence between the Lagrangian and Newton's formulations.

2.7 Hamiltonian formulation of classical mechanics

In the Hamiltonian formulation of classical mechanics, the dynamics of a system are described using the Hamiltonian function H, which is defined as the sum of the system's

kinetic energy T and potential energy V, expressed in terms of the generalized coordinates $\mathbf{q}$ and their conjugate momenta $\mathbf{p}$:

$$H(\mathbf{q}, \mathbf{p}, t) = T(\mathbf{q}, \mathbf{p}, t) + V(\mathbf{q}, t) \tag{2.4}$$

The generalized momenta $\mathbf{p}$ are defined as the partial derivatives of the Lagrangian L (see above) with respect to the generalized velocities $\dot{\mathbf{q}}$:

$$\mathbf{p} = \frac{\partial L}{\partial \dot{\mathbf{q}}} \tag{2.5}$$

Through the Hamiltonian's principle, which states that the action functional S is stationary with respect to variations in the trajectory of the system, we derive Hamilton's equations of motion:

$$\begin{aligned} \dot{\mathbf{q}} &= \frac{\partial H}{\partial \mathbf{p}} \\ \dot{\mathbf{p}} &= -\frac{\partial H}{\partial \mathbf{q}} \end{aligned} \tag{2.6}$$

These equations govern the evolution of the generalized coordinates $\mathbf{q}$ and momenta $\mathbf{p}$ with respect to time t, providing an alternative framework to Lagrangian mechanics for analyzing the dynamics of mechanical systems.

By manipulating Hamilton's equations, one can show that the trajectories obtained from both formalisms are equivalent, thus establishing the equivalence between the Hamiltonian formulation of classical mechanics and Newton's equations of motion. However, it requires applying the Legendre transform to the Lagrangian function introduced above. Hence, we briefly introduce the Legendre transform and leave the rest to the reader to prove the equivalency of Hamilton's equations and Newton's equations.

2.8 Legendre transform

Consider a simple function $f(x)$ of a single variable x. Suppose we aim to express $f(x)$ in terms of a new variable s, where s and x are related by $s = f'(x)$, denoted as $g(x)$, with $f'(x) = \frac{df}{dx}$.

Can we determine $f(x)$ at a point x_0 given only $s_0 = f'(x_0) = g(x_0)$? The answer is no. This is because s_0, being the slope of the tangent line to $f(x)$ at x_0, is also the slope of $f(x) + c$ at $x = x_0$ for any constant c. Thus, $f(x_0)$ cannot be uniquely determined from s_0.

However, if we specify both the slope, $s_0 = f'(x_0)$, and the y-intercept, $b(x_0)$, of the tangent line to the function at x_0, then $f(x_0)$ can be uniquely determined. In fact, $f(x_0)$ will be given by the equation of the tangent line at x_0: $f(x_0) = f'(x_0)x_0 + b(x_0)$.

This equation shows how we may transform from a description of $f(x)$ in terms of x to a new description in terms of s. Recognizing that $f'(x) = g(x) = s$ and $x = g^{-1}(s)$, and assuming that $s = g(x)$ exists and is a one-to-one mapping, the function $b(g^{-1}(s))$, given by $b(g^{-1}(s)) = f(g^{-1}(s)) - sg^{-1}(s)$ contains the same information as the original $f(x)$ but expressed as a function of s instead of x. We call the function $f(s) = b(g^{-1}(s))$ the Legendre transform of $f(x)$.

The Legendre transform $f(s)$ can be written compactly as: $f(s) = f(x(s)) - sx(s)$, where $x(s)$ serves to remind us that x is a function of s through the variable transformation $x = g^{-1}(s)$.

2.9 Non-Hamiltonian systems

We have mainly concentrated on systems governed by Hamilton's principle. Nevertheless, it is essential to briefly diverge and examine broader dynamical equations of motion that do not stem from Lagrangian or Hamiltonian functions, known as non-Hamiltonian systems.

Non-Hamiltonian systems are of interest because Hamilton's equations only apply to conservative systems, isolated or under the influence of external fields. However, many physical systems involve non-conservative forces, like frictional forces or damping effects, which cannot be derived from potential functions. Examples include systems subject to frictional forces, damping effects, and chaotic dynamics exemplified by the Lorenz equations.

Non-Hamiltonian systems find relevance when considering a physical system in contact with a larger system, termed a bath, which regulates macroscopic properties like pressure or temperature. By simplifying the bath's microscopic details into fewer variables that couple with the physical subsystem, non-Hamiltonian equations of motion are proposed. These equations generally deviate from Hamiltonian form due to the elimination of the bath's microscopic nature.

We will focus on dynamical systems of the form: $\dot{x} = \xi(x)$. Here, x represents a phase space vector of n components, and $\xi(x)$ is a continuous, differentiable function. A key characteristic of non-Hamiltonian systems is their nonvanishing phase-space compressibility: $\kappa(x) = \sum_{i=1}^{n} \frac{\partial \dot{x}_i}{\partial x_i} \neq 0$.

When the compressibility is non-zero, many theorems about Hamiltonian systems no longer hold. However, certain properties of Hamiltonian systems can still apply to non-Hamiltonian systems under specific conditions. Even systems initially formulated in canonical variables may exhibit nonvanishing compressibility.

An example of a non-Hamiltonian system is the damped forced harmonic oscillator, described by the equation of motion: $m\ddot{x} = -m\omega^2 x - \zeta\dot{x}$.

This system's dynamics include a nonvanishing compressibility, indicating a decrease in phase-space volume over time. If driven by a periodic forcing function, the system reaches a steady state, exhibiting resonant frequencies characterized by large amplitudes.

2.10 Extensions beyond conservative systems

Although the Lagrangian and Hamiltonian formulations are traditionally developed for systems governed by conservative forces, they can be extended to include non-conservative forces, such as friction or velocity-dependent forces. For non-conservative forces that depend on velocity, it may be possible to define a generalized potential function V that incorporates both positions and velocities. In this case, the generalized forces F_j, which represent forces that may not arise from a potential energy function, can be derived from V according to the relation:

$$F_j = \frac{d}{dt}\frac{\partial V}{\partial \dot{f}_j} - \frac{\partial V}{\partial f_j},$$

which equates to Lagrange's equations. By defining the Lagrangian as $L = T - V$, where T is the kinetic energy, Lagrange's equations of the second kind or the Euler–Lagrange equations of motion are obtained:

$$\frac{\partial L}{\partial f_j} - \frac{d}{dt}\frac{\partial L}{\partial \dot{f}_j} = 0.$$

However, the Euler–Lagrange equations can only account for non-conservative forces when an appropriate potential function can be identified. In cases where such a potential cannot be defined, Lagrange's equations, which directly involve generalized forces rather than potentials, offer a more general approach. This discussion, while important, extends beyond the scope of this thesis, and readers are encouraged to consult more advanced references in analytical mechanics for further details.

2.11 Foundation of statistical mechanics

The roots of thermodynamics trace back to the pioneering efforts of Otto von Guericke (1602–1686), who devised the inaugural vacuum pump in 1650, and Robert Boyle (1627–1691), who, building upon von Guericke's invention, identified an inverse relationship between the pressure and volume of a gas at a constant temperature and quantity, establishing what became known as Boyle's Law. The field further evolved during the nineteenth century, propelled by the groundbreaking contributions of R. J. Mayer (1814–1878) and J. P. Joule (1818–1889), who elucidated the concept of heat as a manifestation of energy. Additionally, R. Clausius (1822–1888) and N. L. S. Carnot (1796–1832) introduced the fundamental notion of entropy. These seminal works collectively form the foundation of thermodynamics, culminating in the formulation of its laws.

While rooted in empirical observations, thermodynamics has endured over time as a phenomenological theory of macroscopic matter. Remarkably, its framework remains elegantly self-contained, devoid of any explicit reference to the microscopic constituents of matter. Nevertheless, in previous sections, we introduced the laws of classical mechanics, which dictate that the positions and velocities of all particles within a system

at any given moment determine both its past and future evolution. Through simple examples involving systems with few degrees of freedom and straightforward forces, we demonstrated that Newton's second law of motion provides the means to deduce the trajectories of such systems. Thus, classical mechanics furnishes a comprehensive framework capable of predicting the properties of a system at any instant in time.

To establish a logical foundation for thermodynamics, it is imperative to employ microscopic laws of motion to macroscopic systems. However, this approach encounters two significant hurdles: Firstly, macroscopic systems possess an immense number of degrees of freedom (with 1 mole consisting of approximately 6.022×10^{23} particles). Secondly, real-world systems are characterized by highly intricate interactions. Consequently, while theoretically feasible to predict the microscopic dynamics of any classical system solely based on initial conditions, the sheer complexity of macroscopic systems renders such efforts futile.

Moreover, the highly nonlinear nature of forces in practical systems precludes analytical solutions to equations of motion. Alternatively, attempting numerical solutions on a computer faces memory constraints; storing a single phase space point for a system of 10^{23} particles exceeds current and foreseeable memory capacities. Thus, although classical mechanics encompasses all necessary information for predicting system properties, extracting this information proves seemingly insurmountable.

Beyond the issue of macroscopic system size lies a subtler challenge: the second law of thermodynamics dictates a time direction, specifically, the direction in which entropy increases. This temporal *arrow* appears incompatible with the reversibility inherent in microscopic mechanical laws, giving rise to Loschmidt's paradox, which seemingly pits thermodynamics against microscopic mechanics.

Demonstrating, for instance, that Newton's second law maintains its structure when subjected to a time-reversal transformation $t \to -t$ is straightforward. This transformation entails $\frac{d}{dt} \to -\frac{d}{dt}$, while $\frac{d^2}{dt^2} \to \frac{d^2}{dt^2}$. The presence of time-reversal symmetry suggests that if a mechanical system progresses from an initial condition x_0 at time $t = 0$ to x_t at $t > 0$, and subsequently, all velocities are reversed ($v_i \to -v_i$), the system will revert to its original microscopic state x_0. This holds true for the microscopic principles of quantum mechanics as well. Consequently, discerning whether a *movie* depicting a mechanical system is advancing in the *forward* or *reverse* direction should be impossible.

The reconciliation of macroscopic thermodynamics with microscopic laws necessitated the emergence of a new discipline: statistical mechanics. Rooted in ideas from Clausius and James C. Maxwell, statistical mechanics burgeoned primarily from the contributions of Ludwig Boltzmann and Josiah W. Gibbs. Early advancements stemmed from the recognition that macroscopic observable properties of a system are not heavily contingent upon the intricate dynamical motion of individual particles, but rather on gross averages that attenuate these microscopic intricacies.

Thus, by statistically applying microscopic mechanical laws, a bridge is established between microscopic and macroscopic theories of matter. This concept not only underpins a rational framework for thermodynamics but also facilitates computation of numerous other macroscopic observables. The cornerstone of statistical mechanics is the ensemble concept, representing a collection of systems sharing common macroscopic traits. Averages over an ensemble yield thermodynamic quantities and other equilibrium and

dynamic properties.

2.12 The ensemble concept

The microscopic state refers to the detailed description of a system at the smallest scale, typically involving individual particles such as atoms or molecules. It encompasses the position and velocity of each constituent particle.

Phase space is a mathematical concept to represent all possible states of a physical system. It is a multi-dimensional space where each dimension corresponds to a degree of freedom of the system, such as position or velocity. Therefore, the microscopic state of a system can be thought of as a specific point in phase space, representing the exact configuration of the system at a given moment in time. By considering the evolution of this point in phase space over time, one can understand how the system's microscopic state changes and how it behaves dynamically.

The laws of thermodynamics, when not accounting for the microscopic origins of macroscopic thermodynamic observables, render thermodynamics primarily a phenomenological theory. Now, our aim is to establish this microscopic basis and forge a connection between the macroscopic and microscopic realms. Although solving classical equations of motion for a system of 10^{23} particles with complex, nonlinear interactions governing real systems is impractical, it is worth considering: If we could solve these equations for such a vast number of particles, would the exhaustive microscopic information generated be essential for describing macroscopic observables?

Intuitively, the answer seems to be *no*. While the extensive microscopic information could predict any macroscopic observable, many microscopic configurations can lead to the same macroscopic properties. For instance, linking temperature to the average kinetic energy of individual particles allows for numerous velocity assignments consistent with a given total energy, resulting in the same temperature measure. Each assignment corresponds to a distinct point in phase space and, consequently, a unique microscopic state. Similarly, connecting pressure to the average force per unit area exerted by particles on container walls permits multiple arrangements yielding the same pressure measure, each corresponding to a unique point in phase space.

Consider predicting macroscopic time-dependent properties: starting with a large set of initial conditions drawn from a state of thermodynamic equilibrium and launching trajectories from each, the resulting trajectories would all be distinct in phase space. Despite their uniqueness, these trajectories should converge, in the long run, to the same macroscopic dynamical observables, such as vibrational spectra and diffusion constants.

This idea—that macroscopic observables are insensitive to precise microscopic details—forms the basis of the ensemble concept introduced by Gibbs. Formally, an ensemble comprises systems governed by the same microscopic interactions and sharing common macroscopic properties (e.g., total energy, volume, and number of moles). Each system evolves under microscopic laws from a different initial condition, ensuring each system has a unique microscopic state at any given time. Macroscopic observables are then calculated by averaging over the ensemble.

Ensembles can describe a range of thermodynamic situations, from isolated systems to those in contact with heat baths or particle reservoirs, or coupled to pressure control mechanisms. In classical ensemble theory, every macroscopic observable of a system is directly linked to a microscopic function of the system's coordinates and momenta. For example, temperature is connected to the average kinetic energy in kinetic theory. Denoting A as a macroscopic equilibrium observable and a(x) as a microscopic phase space function, their relationship within the ensemble is established through an averaging procedure, which reads:

$$\langle A \rangle = \frac{1}{N} \sum_{i=1}^{N} a(x_i) \tag{2.7}$$

where $\langle A \rangle$ denotes the ensemble average of the macroscopic observable A, $a(x_i)$ represents the microscopic phase space function that can be used to calculate A for the i-th microstate x_i, and N is the total number of microstates considered in the ensemble.

Recall our earlier question: If we could solve the equations of motion for a vast number of particles, would the detailed microscopic information be necessary for describing macroscopic observables? While previously answered in the negative, the opposite viewpoint also holds weight: all information required to describe a physical system is encoded in its microscopic equations of motion. While solving these equations for 10^{23} particles is unfeasible, numerical solutions for systems with particle numbers ranging from 10^2 to 10^9, depending on interaction complexity, are possible. Molecular dynamics offers valuable insights into complex phenomena, despite not reaching truly macroscopic scales.

Ensembles in statistical mechanics encompass various frameworks for describing the behavior of physical systems at equilibrium. The three primary ensembles—canonical, microcanonical, and grand canonical—differ in their constraints and the variables they hold constant.

Microcanonical ensemble, also known as the NVE ensemble, represents a statistical scenario wherein the total energy and the number of particles in the system are fixed to specific values. Each member of this ensemble is obliged to possess an identical total energy and particle count. For the system to maintain statistical equilibrium, it must remain entirely isolated, incapable of exchanging energy or particles with its surroundings.

Canonical ensemble, alternatively termed the NVT ensemble, characterizes a statistical ensemble where the energy is not precisely determined, but the number of particles remains constant. Instead of energy, the temperature is specified. This ensemble is suitable for describing a closed system that is, or has been, weakly thermally connected to a heat reservoir. To uphold statistical equilibrium, the system must remain completely closed, unable to exchange particles with its environment, yet it may interact weakly thermally with other systems characterized by ensembles with the same temperature.

Grand canonical ensemble, also referred to as the μVT ensemble, represents a statistical ensemble where neither the energy nor the particle number is fixed. Instead, the temperature and chemical potential are specified. This ensemble is apt for describing an open system, one that is, or has been, weakly connected to a reservoir (such as thermal,

chemical, radiative, or electrical contact). The ensemble maintains statistical equilibrium if the system interacts weakly with other systems characterized by ensembles with the same temperature and chemical potential.

In the following discussion, we will provide a brief overview of each ensemble and explore their applications in physical systems.

2.12.1 Microcanonical ensemble

This ensemble encompasses all microscopic states existing on the constant energy hypersurface $H(x) = E$. This observation implies a close relationship between the microcanonical ensemble and classical Hamiltonian mechanics. In the latter, it has been established that the equations of motion preserve the total energy, denoted as $\frac{dH}{dt} = 0$, leading to $H(x) = \text{const}$.

Consider a scenario where we have a system evolving according to Hamilton's equations. Given that the equations of motion conserve the Hamiltonian $H(x)$, a generated trajectory will produce microscopic configurations belonging to a microcanonical ensemble with energy E. Furthermore, let us suppose that with an infinite duration, the system with energy E can explore all configurations on the constant energy hypersurface. A system demonstrating this property is termed as ergodic and can be utilized to construct a microcanonical ensemble.

In essence, dynamical systems offer a potent approach for generating an ensemble along with its associated averages. This forms the foundation of the molecular dynamics methodology, which has emerged as one of the most widely utilized techniques for addressing problems in statistical mechanics.

2.12.2 Canonical ensemble

The microcanonical ensemble comprises a series of isolated systems, each characterized by fixed values of particle number N, volume V, and total energy E (see above). As all members share the same underlying Hamiltonian $H(x)$, the phase space distribution across the constant energy hypersurface $H(x) = E$ is uniform, while it remains zero off the hypersurface. Consequently, the entire ensemble can be generated through a dynamical system evolving in accordance with Hamilton's equations of motion, under the assumption of ergodicity—wherein the dynamical system explores all points on the constant energy hypersurface over an infinite duration. Leveraging this assumption, a molecular dynamics calculation can yield a microcanonical distribution.

However, the primary drawback of the microcanonical ensemble lies in its departure from the conditions typically encountered in experimental settings, where total energy remains constant. Hence, there arises a necessity to devise ensembles featuring different sets of thermodynamic control variables to better align with common experimental conditions. An exemplary alternative is the canonical ensemble, wherein the thermodynamic control variables consist of constant particle number N, constant volume V, and constant temperature T. These parameters delineate a system in thermal contact with an infinite heat source, thus reflecting more conventional experimental setups.

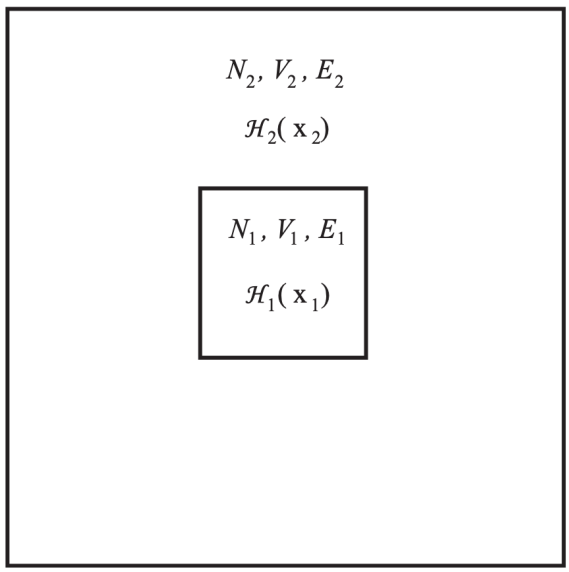

Figure 2.1: A system (system 1) in contact with a thermal reservoir (system 2). System 1 has N1 particles in a volume V1; system 2 has N2 particles in a volume V2. This image and caption are sourced from ref. 92.

In the canonical ensemble, we presume that a system can solely transfer heat with its surroundings. To demonstrate further, we examine two systems in thermal connection. We designate the physical system as *System 1* and the surroundings as *System 2* (refer to Fig. 2.1). System 1 is assumed to encompass N_1 particles within a volume V_1, while System 2 houses N_2 particles within a volume V_2. Moreover, System 1 possesses an energy E_1, and System 2 holds an energy E_2, thus yielding a total energy $E = E_1 + E_2$. System 2 is deliberately considered much larger than System 1, ensuring $N_2 \gg N_1$, $V_2 \gg V_1$, and $E_2 \gg E_1$. Often termed as a thermal reservoir, System 2 can exchange energy with System 1 without significantly altering its own energy state. The thermodynamic *universe*, constituted by the combination of System 1 and System 2, is addressed within the microcanonical ensemble. Consequently, the total Hamiltonian $H(x)$ of the universe is delineated as the sum of contributions from System 1 and System 2, denoted as $H_1(x_1) + H_2(x_2)$, where x_1 represents the phase space vector of System 1, and x_2 signifies the phase space vector of System 2.

It can be shown that the mere solution of Hamilton's equations for the total Hamiltonian $H(x) = H_1(x_1) + H_2(x_2)$ would result in the separate conservation of $H_1(x_1)$ and $H_2(x_2)$, owing to the separability of the Hamiltonian. However, the microcanonical distribution, proportional to $\delta(H(x) - E)$, enables the exploration of all conceivable energies E_1 and E_2 satisfying $E_1 + E_2 = E$, without necessitating an explicit potential coupling between the two systems. Given the capacity for energy exchange between the two systems, the conservation of $H(x_1)$ and $H(x_2)$ independently is not anticipated.

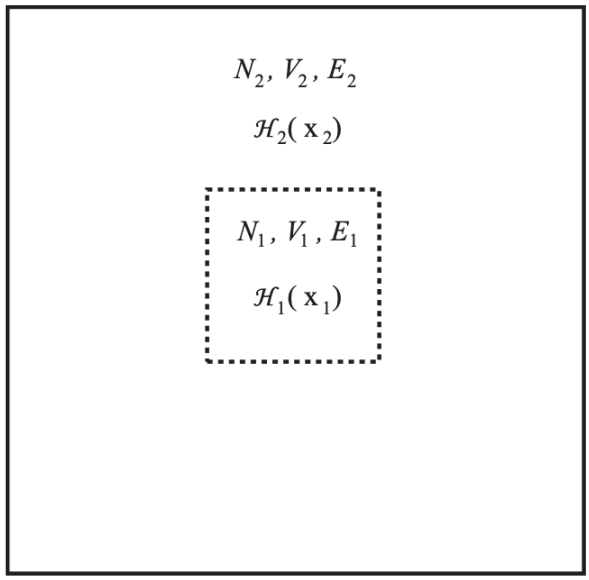

Figure 2.2: Two systems in contact with a common thermal reservoir at temperature T. System 1 has N1 particles in a volume V1; system 2 has N2 particles in a volume V2. The dashed lines indicate that systems 1 and 2 can exchange particles. This image and caption are sourced from ref. 92.

2.12.3 Grand canonical ensemble

The microcanonical and canonical ensembles we have explored share a common characteristic: they maintain a fixed particle number N as one of the controlling variables. However, the grand canonical ensemble diverges from this pattern by allowing fluctuations in the particle number while holding the chemical potential μ constant.

Why is such an ensemble necessary? Numerous physical situations involve systems where the particle number fluctuates. These include phenomena such as liquid-vapor equilibria, capillary condensation, and, notably, in fields like molecular electronics and batteries, where a device is linked to an electron source. In computational molecular design, there is a need to explore a broad *chemical space* of compounds to optimize specific properties (e.g., binding energy to a target), necessitating variation in both the number and chemical identity of constituent atoms. Additionally, in some instances, working within the grand canonical ensemble simply proves to be more convenient. Moreover, given that all ensembles become equivalent in the thermodynamic limit, we have the flexibility to select the ensemble that best suits the requirements of the specific problem at hand.

Given that the grand canonical ensemble utilizes μ, V, and T as its control parameters, it is convenient to conceptualize this ensemble as akin to a canonical ensemble linked with a particle reservoir, which instigates fluctuations in the particle count. As the terminology suggests, a particle reservoir refers to a system capable of accepting or releasing particles without significantly altering its own particle number. Hence, envisioning two systems

interconnected with a shared thermal reservoir at temperature T becomes apt: System 1, with N_1 particles and volume V_1, and System 2, with N_2 particles and volume V_2. These two systems possess the capacity to exchange particles, with System 2 serving as the particle reservoir, thereby ensuring $N_2 \gg N_1$ (refer to Fig. 2.2).

2.13 Free energy

In the microcanonical ensemble, we consider the control variables as the particle number N, volume V, and total energy E. The entropy $S(N, V, E)$ is a *state function* dependent on these variables. A state function is a property that depends only on the current state of a system and not on how that state was reached. It essentially describes the condition or configuration of the system at a particular moment, regardless of the path taken to reach that condition.

The thermodynamic variables obtained from partial derivatives of the entropy are: $\frac{1}{T} = \left(\frac{\partial S}{\partial E}\right)_{N,V}$, $\frac{P}{T} = \left(\frac{\partial S}{\partial V}\right)_{N,E}$, and $\frac{\mu}{T} = \left(\frac{\partial S}{\partial N}\right)_{V,E}$.

In terms of energy E, these relations become: $T = \left(\frac{\partial E}{\partial S}\right)_{N,V}$, $P = -\left(\frac{\partial E}{\partial V}\right)_{N,S}$, and $\mu = \left(\frac{\partial E}{\partial N}\right)_{V,S}$.

To transform from the microcanonical to the canonical ensemble, the later equations are preferred, as they directly provide the temperature T instead of $1/T$. The aim is to transform the function $E(N, V, S)$ into a function of N, V, and T. Since $T = \partial E/\partial S$, one can apply the Legendre transform method. The new function, denoted as $A(N, V, T)$, is given by:

$$A(N, V, T) = E(N, V, S(N, V, T)) - T\frac{\partial S(N, V, T)}{\partial T} = E(N, V, S(T)) - TS(N, V, T) \quad (2.8)$$

This function $A(N, V, T)$ is known as the *Helmholtz free energy*. Physically, when a thermodynamic transformation of a system from state 1 to state 2 occurs along a reversible path, the work needed equals the change in Helmholtz free energy ΔA.

By applying a similar Legendre transformation, the volume in the Helmholtz free energy $A(N, V, T)$ can be transformed into the external pressure P, resulting in a new free energy denoted as $G(N, P, T)$:

$$G(N, P, T) = A(N, V(P), T) - V(P)\frac{\partial A}{\partial V} \quad (2.9)$$

Utilizing the relation $P = -\frac{\partial A}{\partial V}$, we derive:

$$G(N, P, T) = A(N, V(P), T) + PV(P) \quad (2.10)$$

This function $G(N, P, T)$ is recognized as the *Gibbs free energy*. This Legendre transformation converts the canonical ensemble into another ensemble, known as the *isothermal-isobaric (NPT)* ensemble.

It is important to note that free energy functions, balancing energetic and entropic terms, determine whether a process is thermodynamically favorable (with a decrease in free energy) or unfavorable (with an increase in free energy). It is worth noting that, however, they do not dictate the time scale of the process.

It is now evident that free energy holds significant importance in statistical mechanics. However, rather than focusing solely on absolute free energy values, the emphasis often lies in discerning the difference between the free energies of two thermodynamic states.

Throughout this thesis, we will repeatedly discuss free energy differences in various contexts, as detailed in subsequent chapters. Numerous techniques have been developed for calculating free energies, with two prominent methods featuring prominently in our work: *steered molecular dynamics* and *thermodynamic integration*. These techniques will be introduced in the following sections.

For a comprehensive understanding of free energy calculation methods, readers are encouraged to consult refs. 92 and 93.

2.13.1 Steered molecular dynamics

Let us first introduce the concept of the *partition function* and elucidate its significance in statistical mechanics.

The partition function is a fundamental concept in statistical mechanics. At its core, the partition function Z is a mathematical function that encapsulates all the information about the possible states of a system. It accounts for the different energy levels and degeneracies (multiplicities) of these states.

The partition function is typically calculated as the sum or integral over all possible states of the system, weighted by their Boltzmann factors. For discrete systems, the partition function is given by:

$$Z = \sum_i e^{-\beta E_i} \tag{2.11}$$

where E_i represents the energy of the i-th state, and $\beta = \frac{1}{k_B T}$ is the inverse temperature, with k_B being the Boltzmann constant and T the temperature.

For continuous systems, the partition function is expressed as an integral:

$$Z = \int e^{-\beta E} \, d\Gamma \tag{2.12}$$

where E represents the energy of a state, and $d\Gamma$ represents the phase space volume element.

The partition function counts the number of possible microscopic states accessible in a specific ensemble's phase space. Each ensemble has its unique partition function, determined by the macroscopic properties defining that ensemble. It can be shown that the system's thermodynamic properties are computed using different partial derivatives of the partition function.

The use of steered molecular dynamics (SMD) to compute free energy can be summarized as follows. For a comprehensive discussion, readers are referred to ref. 94, from which the following formulations have been obtained. The change in free energy between two states, where $\lambda = \lambda_0$ and $\lambda = \lambda_1$, can be expressed as: $\Delta A = \Delta A_{\lambda_1} - \Delta A_{\lambda_0} = -\frac{1}{\beta} \ln \frac{Z_{\lambda_0}}{Z_{\lambda_1}}$, where Z is the partition function for the system with the given value of the reaction coordinate λ, such that $Z_{\lambda_1} = \int d\mathbf{q} \exp[-\beta H(\mathbf{q}, \lambda = \lambda_1)]$, and the Hamiltonian depends on the positions of all atoms $\mathbf{q}$ and the reaction coordinate λ.

In 1997, Jarzynski demonstrated that this change in free energy between two states can be precisely related to the ensemble average of the Boltzmann-weighted work performed in numerous non-equilibrium transformations from initial to final states:

$$\Delta A = -\frac{1}{\beta} \ln \langle e^{-\beta W} \rangle \tag{2.13}$$

where W denotes the external work executed in changing the reaction coordinate λ from λ_0 to λ_1 in a time-dependent manner. The Jarzynski equality only demands that the initial configurations be drawn from the equilibrium ensemble with $\lambda = \lambda_0$, and it is worth noting that the final states with $\lambda = \lambda_1$ do not pertain to an equilibrium ensemble.

In SMD simulations, the reaction coordinate is typically not constrained to a specific value; instead, it is restrained to a particular center (often according to a harmonic potential of force constant k) that changes with a constant velocity v during a simulation of the irreversible transformation from λ_0 to λ_1:

$$V(\mathbf{q}, t) = \frac{1}{2} k[\lambda(t) - \lambda'(\mathbf{q})]^2 \tag{2.14}$$

where the prime notation denotes the evaluation of the reaction coordinate for a given microscopic state $\mathbf{q}$ of the system, as opposed to the time-dependent value of the reaction coordinate center, which is $\lambda(t) = \lambda_0 + vt$.

Despite introducing an additional biasing potential to the system, the underlying potential of mean force (PMF) $G(\lambda)$ can still be recovered using Jarzynski's equality and re-weighting estimators similar to the weighted histogram analysis method (WHAM). Alternatively, if the force constant k is sufficiently large (referred to as the *stiff-spring approximation*), such that $\lambda'(\mathbf{q}) \approx \lambda(t)$, the PMF $G(\lambda)$ of the system without the presence of a biasing potential can be approximated by the following relation:

$$\frac{1}{2}(\Delta A''(t))^2 G[\lambda = \lambda(t)] \approx \Delta A(t) - \frac{2kv^2}{\beta} - A(t) \tag{2.15}$$

It is noteworthy that, generally, if k is large, the higher-order terms in Equation 2.15 become negligible. Conventionally, when invoking the Jarzynski equality, ΔA is estimated using the so-called Jarzynski estimator:

$$\Delta \hat{A} = -\frac{1}{\beta} \ln \frac{1}{N} \sum_{i=1}^{N} e^{-\beta W_i} \tag{2.16}$$

2.13.2 Thermodynamic integration

We first briefly introduce *free energy perturbation theory*. Let us start by examining how a system moves from one state to another in terms of its free energy. We denote these states generally as A and B. At a microscopic level, these two states are characterized by their potential energy functions, $U_A(\mathbf{r}_1, \ldots, \mathbf{r}_N)$ and $U_B(\mathbf{r}_1, \ldots, \mathbf{r}_N)$ respectively. The Helmholtz free energy difference between states A and B is straightforwardly expressed as $\Delta A_{AB} = A_B - A_A$. The two free energies A_A and A_B can be defined in terms of their respective canonical partition functions Q_A and Q_B. Thus, $A_A = -kT \ln Q_A$ and $A_B = -kT \ln Q_B$. Consequently, the free energy difference is:

$$\Delta A_{AB} = A_B - A_A = -kT \ln \left(\frac{Q_B}{Q_A} \right) = -kT \ln \left(\frac{Z_B}{Z_A} \right) \tag{2.17}$$

where Z_A and Z_B represent the configurational partition functions for states A and B, respectively: $Z_A = \int d^N \mathbf{r} \exp\left(-\beta U_A(\mathbf{r}_1, \ldots, \mathbf{r}_N)\right)$ and $Z_B = \int d^N \mathbf{r} \exp\left(-\beta U_B(\mathbf{r}_1, \ldots, \mathbf{r}_N)\right)$.

The approach of free energy perturbation paints a scenario where configurations sampled from the canonical distribution of state A swiftly transition to state B by a mere alteration of the potential from U_A to U_B. However, when there is insufficient overlap between states A and B, introducing a series of intermediate states can define an optimal transformation path, depicting a gradual transition from A to B. *Thermodynamic integration* is an alternate method where the system smoothly transitions, adiabatically, from A to B.

In this method, an adiabatic path is established, ensuring the system fully relaxes at each stage. To facilitate this transition, we introduce an *external* parameter λ to parameterize the adiabatic path. This parameter defines a new potential energy function, sometimes termed a *metapotential*, represented as:

$$U(\mathbf{r}_1, ..., \mathbf{r}_N, \lambda) = f(\lambda) U_A(\mathbf{r}_1, ..., \mathbf{r}_N) + g(\lambda) U_B(\mathbf{r}_1, ..., \mathbf{r}_N) \tag{2.18}$$

Here, $f(\lambda)$ and $g(\lambda)$ are switching functions, ensuring $U(\mathbf{r}_1, ..., \mathbf{r}_N, 0) = U_A(\mathbf{r}_1, ..., \mathbf{r}_N)$ and $U(\mathbf{r}_1, ..., \mathbf{r}_N, 1) = U_B(\mathbf{r}_1, ..., \mathbf{r}_N)$. The concept behind this mechanism is akin to an imaginary external control initiating the system in state A ($\lambda = 0$) and gradually transitioning

it by switching off potential U_A while activating potential U_B. This process concludes at $\lambda = 1$, with a common choice for $f(\lambda)$ and $g(\lambda)$ being $f(\lambda) = 1 - \lambda$ and $g(\lambda) = \lambda$.

To compute the free energy difference ΔA_{AB}, we consider the canonical partition function of a system described by the potential $U(\mathbf{r}_1, ..., \mathbf{r}_N, \lambda)$ for a particular λ:

$$Q(N, V, T, \lambda) = C_N \int dNpdNr \exp\left(-\beta \sum_{i=1}^{N} \frac{p_i^2}{2m_i} + U(\mathbf{r}_1, ..., \mathbf{r}_N, \lambda)\right) \tag{2.19}$$

This partition function yields a free energy via: $A(N, V, T, \lambda) = -kT \ln Q(N, V, T, \lambda)$. We have previously demonstrated that derivatives of A with respect to N, V, or T provide the chemical potential, pressure, or entropy, respectively. However, what does the derivative with respect to λ signify for $A(N, V, T, \lambda)$? According to the above equation: $\frac{\partial A}{\partial \lambda} = -kT\frac{\partial Q}{\partial \lambda} = -kT\frac{\partial Z}{\partial \lambda}$. Computing the derivative of Z with respect to λ, we get: $\frac{kT}{Z}\frac{\partial Z}{\partial \lambda} = -\langle\frac{\partial U}{\partial \lambda}\rangle$. The free energy difference ΔA_{AB} can be straightforwardly derived as: $\Delta A_{AB} = \int_0^1 \frac{\partial A}{\partial \lambda} d\lambda$, which yields:

$$\Delta A_{AB} = \int_0^1 \langle\frac{\partial U}{\partial \lambda}\rangle_\lambda d\lambda \tag{2.20}$$

where $\langle \ldots \rangle \lambda$ denotes an average over the canonical ensemble described by the distribution $\exp[-\beta U(\mathbf{r}_1, \ldots, \mathbf{r}_N, \lambda)]$ with λ fixed at a particular value.

The specific selection of $f(\lambda) = 1 - \lambda$ and $g(\lambda) = \lambda$ can be easily understood as:

$$\Delta A_{AB} = \int_0^1 \langle U_B - U_A\rangle_\lambda d\lambda \tag{2.21}$$

This relationship recalls the connection between work and free energy from the second law of thermodynamics. If, during the transformation from state A to state B, work W is performed on the system, then $W \geq \Delta A_{AB}$, where equality holds solely for a reversible path. This inequality is referred to as the *work–free–energy inequality*. Since reversible work corresponds to a change in potential energy, the above equation serves as a statistical version of the inequality for the case of equality. It indicates that the free energy difference is the ensemble average of the microscopic reversible work required to transition the potential energy of each configuration from U_A to U_B along the selected λ-path. Notably, the thermodynamic integration formula, denoted as Equation 2.20, remains independent of the choice of $f(\lambda)$ and $g(\lambda)$, consistently yielding the reversible work via the free energy difference. However, the flexibility in selecting the λ-path can be leveraged to design more efficient adiabatic switching algorithms beyond the simple choice of f(λ) = 1 - λ and g(λ) = λ.

In practice, the implementation of the thermodynamic integration formula involves selecting a set of M λ values from the interval [0, 1], followed by conducting full molecular dynamics (or another integrator like Monte Carlo) calculations at each λk to generate the average $\frac{\partial U}{\partial \lambda_k}$. Subsequently, these values are substituted into Equation 2.20, and the

result is numerically integrated to derive the free energy difference ΔA_{AB}. The chosen values λk can be evenly spaced or a set of Gaussian quadrature nodes, depending on the anticipated variation of $A(N, V, T, \lambda)$ with λ for specific $f(\lambda)$ and $g(\lambda)$.

Chapter 3

Breakdown of universal scaling for nanometer-sized bubbles in graphene[¶]

In this chapter, we report the formation of nanobubbles on graphene with radius of the order of 1 nm, using ultra-low energy implantation of noble gas ions (He, Ne, Ar) into graphene grown on a Pt(111) surface. We show that the universal scaling of the aspect ratio, which has previously been established for larger bubbles, breaks down when the bubble radius approaches 1 nm, resulting in much larger aspect ratios. Moreover, we observe that the bubble stability and aspect ratio depend on the substrate onto which the graphene is grown (bubbles are stable for Pt but not for Cu) and trapped element. We interpret these dependencies in terms of the role of the adhesion energies between the three constituents: graphene, substrate and noble gas atoms.

3.1 Introduction

Owing to its unrivaled elasticity and strength [37, 95], graphene is able to hold matter at extreme pressures in the form of bubbles with dimensions down to the nanometer scale [52, 96–98]. These bubbles offer new opportunities to explore chemistry and physics under the extreme conditions that both graphene and the trapped matter are subject to, for example, high-pressure chemical reactions [48, 99] and strain-induced pseudomagnetic fields [100–102]. Similar nanobubbles in other 2D materials such as MoS_2 and h-BN are also being investigated as single photon emitters for quantum communication [103, 104].

While previous research has mostly dealt with bubbles with a radius of few nm and larger, the sub-nanometer regime remains largely unexplored. Here we report the formation of graphene nanobubbles with radius down to below 1 nm, filled with He, Ne and Ar. Delving into the physical mechanisms determining the stability and shape of these sub-nanometer bubbles reveals that they constitute a fundamentally different regime, exhibiting extreme aspect ratios and pressures (estimated to exceed 30 GPa). The unique properties of this sub-nanometer regime open an unexplored ground for applications of nanobubbles in 2D materials.

[¶] This chapter contributed to the paper: Breakdown of universal scaling for nanometer-sized bubbles in graphene. Nano Letters **21**, 8103–8110 (2021).

The properties of graphene bubbles with radius of few nm and larger are relatively well understood on the basis of elasticity theory, graphene's elastic properties and its van der Waals attraction to the substrate [52]. In this regime, bubbles have been observed on various substrates (*e.g.*, Ir, Pt, h-BN, SiO_2) with a variety of trapped substances (*e.g.*, water, noble gases, hydrocarbons) [52, 96, 98, 105, 106], which do not appear to significantly affect the bubble stability [52, 98]. Substrate and trapped substance do affect key properties, such as shape (in particular the aspect ratio) and the pressure inside the bubble [52, 98]. This dependence is largely determined by the balance of the adhesion energies: between graphene and the substrate (γ_{GS}), between the substrate and the trapped substance (γ_{Sb}) and between the graphene and the trapped substance (γ_{Gb}) [52]. A particularly striking feature demonstrated for nanobubbles in the few nm regime and larger is that the aspect ratio exhibits universal scaling:

$$\frac{h_{\max}}{R} = \left(\frac{\pi\gamma}{5c_1 Y}\right)^{1/4}, \qquad \gamma = \gamma_{GS} - \gamma_{Sb} - \gamma_{Gb}, \tag{3.1}$$

where $h_{\max}$ is the bubble maximum height, R is the bubble radius at the base, c_1 is a constant (0.7) and Y the Young modulus [52]. Here, by combining scanning tunneling microscopy (STM) measurements with molecular dynamics (MD) simulations and density functional theory (DFT) calculations, we show that this universal scaling breaks down at small R (near 1 nm and below). We also observe that the bubble stability is strongly dependent on the substrate. We interpret these dependencies in terms of adhesion energies (γ_{GS}, γ_{Sb} and γ_{Gb}). Moreover, extreme values of pressure inside these sub-nm bubbles (exceeding 30 GPa) are predicted by our MD simulations.

3.2 Experimental details and basic characterization

Our samples consist of epitaxial graphene grown by chemical vapor deposition (CVD) on epitaxial Pt(111) and Cu(111) thin films grown on sapphire(0001) substrates [107, 108]. Nanobubbles are formed by implanting noble gas ions (He, Ne and Ar), with a kinetic energy of 25 eV, with perpendicular incidence with respect to the surface. Bubbles were found to only form for graphene on Pt(111) (Fig. 3.1), not for graphene on Cu(111) (Fig. 3.2). In the following we will focus on Pt(111), and return to Cu(111) further below when discussing how the bubble stability depends on the substrate. Ion implantation has been previously used to form graphene nanobubbles of noble gases [96, 105, 106].

In contrast to the previous studies, where ion beams with energies of 500 eV and higher were used, our approach is based on ultra-low energy (ULE) ion implantation. Such low energies are crucial to minimize irradiation-induced damage. Based on our MD simulations, we selected 25 eV (surface normal incidence) as sufficiently high for a significant fraction of the ions to be transmitted through the graphene layer, but sufficiently low to minimize carbon atom displacements (*i.e.*, formation of vacancies and related point defects). While ULE ion implantation has been previously used for doping of graphene (*e.g.*, with B and N [109–111]) where vacancies are required (which allows for substitu-

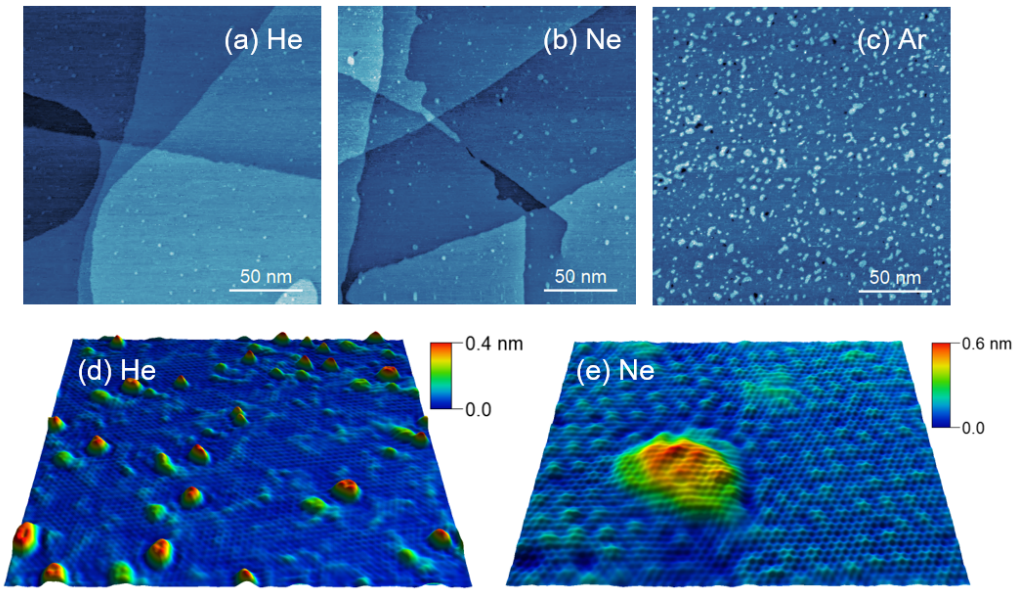

Figure 3.1: STM micrographs showing (a) He, (b) Ne and (c) Ar bubbles in graphene/Pt(111). STM micrographs (50×50 nm^2 for (d) and 10×10 nm^2 for (e)), with atomic resolution, showing a continuous graphene atomic lattice, in particular, over the bubble.

tional incorporation of the dopant atoms). Such defects must be avoided in the context of the present work so that the intrinsic elastic properties of graphene are maintained.

The graphene bubbles observed in our samples are identified as nanometer scale protrusions on the surface of graphene (grown on Pt(111), implanted with the noble gases) as shown in the STM topographies in Fig. 3.1. The fact that the graphene lattice can be resolved even over these protrusions confirms that the implanted noble gases are intercalated (Fig. 3.1e), i.e., that the protrusions are not due to matter deposited on top of graphene. The fraction of surface that is covered by bubbles (for the same implanted fluence) was found to vary between implanted noble gas elements (Fig. 3.1a-c). This dependence is likely due to the different transmission and backscattering probabilities for the different elements. The high structural order of our irradiated samples is supported by our atomic resolution STM measurements on as-implanted samples (Fig. 3.1e) and by the integrity of the moiré superstructure in most of the surface with only minor disorder (Figs. 3.1d,e).

3.3 Breakdown of universal scaling at low radius

The radius and aspect ratio of each bubble, for the different elements (He, Ne and Ar), are plotted in Fig. 3.3. A clear trend is observed for all three gases. For larger R values (> 1 nm), the aspect ratio tends to converge to a constant value of about 0.2, which is in agreement with the universal scaling previously observed for bubbles with radius of few

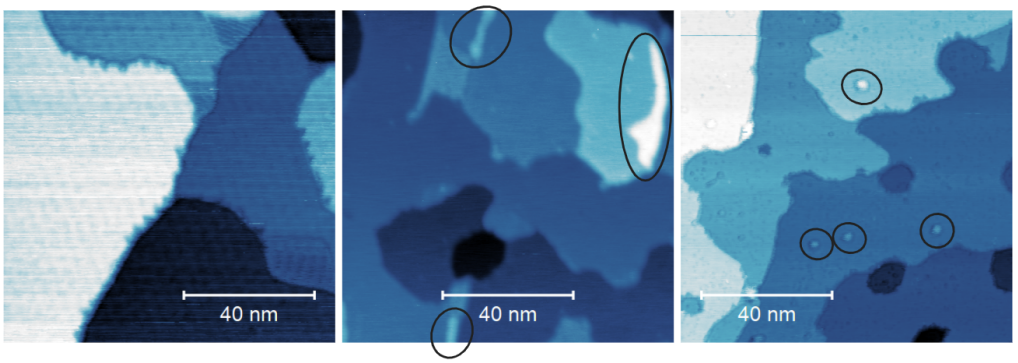

Figure 3.2: STM topographies of (left) pristine graphene on Cu(111) and helium implanted graphene on Cu(111) exhibiting: (middle) bubble/wrinkles in terrace edges and (right) bubbles trapped in dip-like defects on the Cu surface. These bubbles/wrinkles are indicated by black ellipses.

nm and larger [52]. However, as R approaches the sub-nanometer regime, the universal scaling breaks down, showing an increase in the aspect ratio and approaching 1 for Ne bubbles. From the experimental data in Fig. 3.3 we calculated, for each gas (He, Ne, Ar), an average value for $h^0_{\max}$ (from the 10% smallest bubbles) and an average value for $\frac{h_{\max}}{R}\Big|_{R\gg 1\,\mathrm{nm}}$ (from the 10% largest bubbles). These values are compiled in Table 3.1.

This breakdown of universal scaling can be explained by the existence of a minimum value for $h_{\max}$ ($h^0_{\max}$), corresponding to one atomic layer of the trapped gas atoms. As R approaches this regime, $h_{\max}$ becomes a constant value ($h^0_{\max}$), and consequently $h_{\max}/R$ transits into a $\sim 1/R$ dependence. This is illustrated in Fig. 3.3c by the fit to the experimental $h_{\max}/R$ data with the function ($h_{\max}/R = c/R$), where c (around 3 to 4 Å) is comparable to $h^0_{\max}$. This $\sim 1/R$ fit crosses the value corresponding to $\frac{h_{\max}}{R}\Big|_{R\gg 1\,\mathrm{nm}}$ (dotted line) around 1-2 nm, above which the universal scaling regime is valid and $h_{\max}/R$ becomes constant, given by equation 3.1.

This behavior is well reproduced by our MD simulations of bubbles with varying number of trapped atoms (from 800, with R of a few nm, down to a few atoms, with R below 1 nm - Fig. 3.3). In particular, for the smallest bubbles with a small number of trapped atoms (of the order of 10), the monolayer-like configuration is clearly observed in our MD simulations (Fig. 3.4), while for the larger bubbles, the trapped atoms are distributed over multiple layers of gas atoms (Fig. 3.4). The significant spread in aspect ratio for a given radius (experimental data points in Fig. 3.3) is likely due to a varying strength of the adhesion between graphene and the Pt surface (γ_{GS}) over the sample surface. Such non-homogeneity can result from the varying (relative) orientation of the graphene and Pt lattices (the graphene layers grown on Pt are polycrystalline), as well as possible local variations in graphene-Pt adhesion due to point defects in graphene.

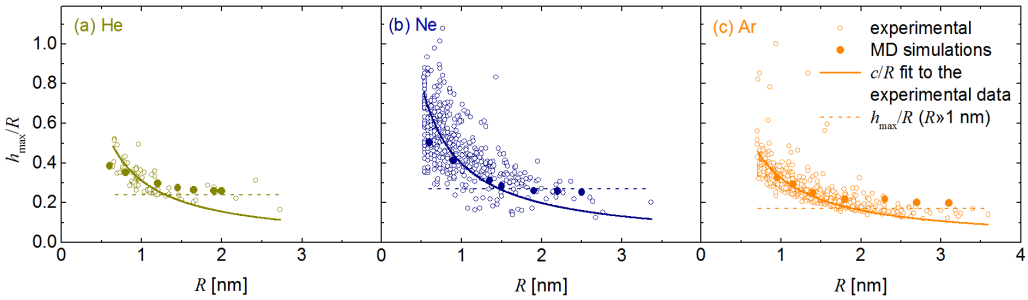

Figure 3.3: $h_{\max}/R$ as a function of R obtained from STM micrographs as those shown in Fig. 3.1 (empty circles) and from MD simulations (filled circles), for (a) He, (b) Ne and (c) Ar bubbles in graphene/Pt(111). Each experimental data point corresponds to one bubble. The solid line is a fit with the function ($h_{\max}/R = c/R$). The dotted line corresponds to the value of $\left.\frac{h_{\max}}{R}\right|_{R\gg 1\,\mathrm{nm}}$.

Table 3.1: Aspect Ratio and Related Parameters. $h^0_{\max}$ and $\left.\frac{h_{\max}}{R}\right|_{R\gg 1\,\mathrm{nm}}$ are obtained from the data in Fig. 3.3. $h^0_{\max}$ is the average of $h_{\max}$ taken over the 10% smallest bubbles. $\left.\frac{h_{\max}}{R}\right|_{R\gg 1\,\mathrm{nm}}$ is the average $\frac{h_{\max}}{R}$ taken over the 10% largest bubbles. The values inside the brackets are the standard deviation associated with the respective averages. $\langle \Delta z \rangle$ is the average z-motion amplitude obtained from the MD simulations, for the smallest bubbles (radius of ~ 6 Å for He and Ne, and ~ 9 Å for Ar). γ is calculated using equation 3.1 with $\frac{h_{\max}}{R}$ given by $\left.\frac{h_{\max}}{R}\right|_{R\gg 1\,\mathrm{nm}}$. r_{vdW} is the van der Waals radius (from ref. 112).

element	$h^0_{\max}$ [Å]	r_{vdW} [Å]	$\langle \Delta z \rangle$ [Å]	$\left.\frac{h_{\max}}{R}\right\|_{R\gg 1\,\mathrm{nm}}$	γ [eV·Å^{-2}]
He	2.9(±0.5)	1.43	0.31	0.24(±0.05)	0.08
Ne	3.5(±0.8)	1.58	0.49	0.27(±0.07)	0.13
Ar	3.1(±0.6)	1.94	0.29	0.17(±0.03)	0.02

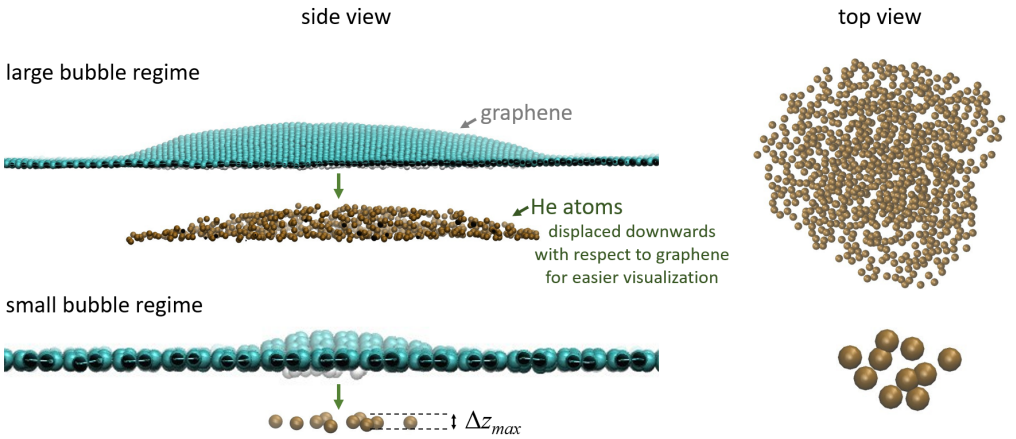

Figure 3.4: Top and side view of examples of large and small He bubbles, simulated using MD. The He atoms are shown displaced downwards, away from the graphene layer, for easier visualization. In the small bubble regime, the He atoms are distributed in a monolayer-like configuration (*i.e.*, without being on top of each other), but still with a significant out-of-plane motion amplitude (Δz_{max}).

3.4 Dependence on Trapped Element

Let us first consider the $R \gg 1$ nm regime, where the universal scaling given by equation 3.1 [52] applies and thereby extract γ (given in Table 3.1) for each gas (He, Ne and Ar). Although the values of $\frac{h_{\max}}{R}$ for $R \gg 1$ nm for He, Ne and Ar are different, the spread over the various bubbles (reflected in a large standard deviation) blurs out these differences. Nevertheless, the data strongly suggest that this quantity does depend on the trapped element. Such a scenario can be understood as due to a variation in γ, that is, higher for Ne ($\gamma \sim 0.13$ eV/Å^2) than for He (~ 0.08 eV/Å^2) and Ar (~ 0.02 eV/Å^2). Taking $\gamma_{GS} = 0.25$ eV/Å^2 for graphene on Pt [113], implies that $\gamma_{Sb} + \gamma_{Gb}$ is of the order of γ_{GS} for Ar (giving $\gamma = 0.02$ eV/Å^2), but significantly smaller for He and Ne. In other words, in the bubble configuration, the interaction (of van der Waals nature) of the gas atoms with the Pt surface or with the graphene layer appears to be more repulsive for Ne compared to He and Ar.

A similar trend is observed in the low-R regime, where the Ne bubbles clearly reach higher h_{max} values than for He and Ar bubbles (Fig. 3.3), and $h^0_{\max}$ also being larger (although with a significant spread over various bubbles) for Ne than for He and Ar (Table 3.1). This is particularly noteworthy, as it does not follow the same trend as the van der Waals radius (r_{vdW}), which increases from He, to Ne, to Ar (Table 3.1). Moreover, $h^0_{\max}$ values are significantly larger than what one would expect for a rigid atomic monolayer, that is, the van der Waals radius of the gas atoms (Fig. 3.5). These two facts can be understood as being a result of out-of-plane motion of the gas atoms, even for small bubbles (monolayer-like), which is indeed observed in our MD simulations (Fig. 3.4). The average z-motion amplitude (averaged over time and over the trapped atoms) obtained from the MD simulations, for the smallest bubbles ($\langle \Delta z \rangle$ in Table 3.1)

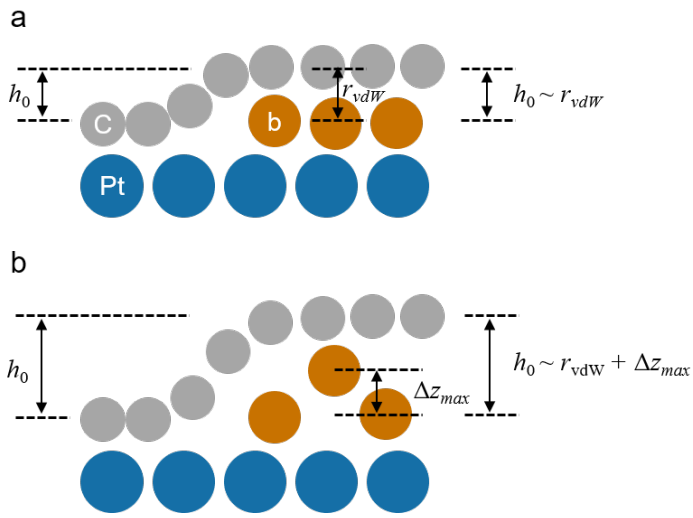

Figure 3.5: Schematics illustrating the relation between the bubble height in the small-bubble limit (h_0) measured with STM, the van der Waal radius of the trapped atoms (r_{vdW}) and the maximum out-of-plane motion amplitude (Δz_{max}): (a) When $\Delta z_{max} \sim 0$, $h_0 \sim r_{vdW}$ and (b) when $\Delta z_{max} > 0$, $h_0 \sim r_{vdW} + \Delta z_{max}$.

follows the trend observed for $h^0_{\max}$, that is, being significantly larger for Ne than for He and Ar. This out-of-plane motion forces $h^0_{\max}$ to be larger than the van der Waals radius (Fig. 3.5b), that is, larger than that associated with a rigid atomic monolayer (Fig. 3.5a), by an amount Δz_{max} that depends on γ_{Sb} and γ_{Gb}. In other words, the weaker the binding of the trapped atoms to the graphene layer and to the Pt surface, the more the gas atoms are allowed to move out-of-plane, and therefore the more the sub-nm bubbles deviate from a rigid atomic monolayer.

3.5 Extreme Pressure

The breakdown of the universal scaling, leading to extreme aspect ratios, is likely to be associated with other unusual physical properties in these sub-nanometer bubbles. Although probing such properties is beyond the scope of this letter, it is worthwhile discussing pressure as an example, in particular since it can be obtained from our MD calculations. According to the general understanding of surface-induced pressure in solids, the pressure scales with the ratio of surface area to the volume of the solid phase [114]. For the bubbles under consideration here, as R decreases and the atoms inside the bubbles become more monolayer-like, the surface-to-volume ratio ($\sim \Delta z^{-1}$) increases dramatically, since $\Delta z \rightarrow 0$. One can therefore expect the pressure to also increase dramatically in the limit of small R. Our MD calculations show exactly that (Fig. 3.6), that is, a diverging behavior with decreasing R, reaching remarkably high values of up to ~30 GPa. These values were obtained using the stress tensor-based method [115], as recently applied to nanobubbles in graphene [98], with pressure being given by:

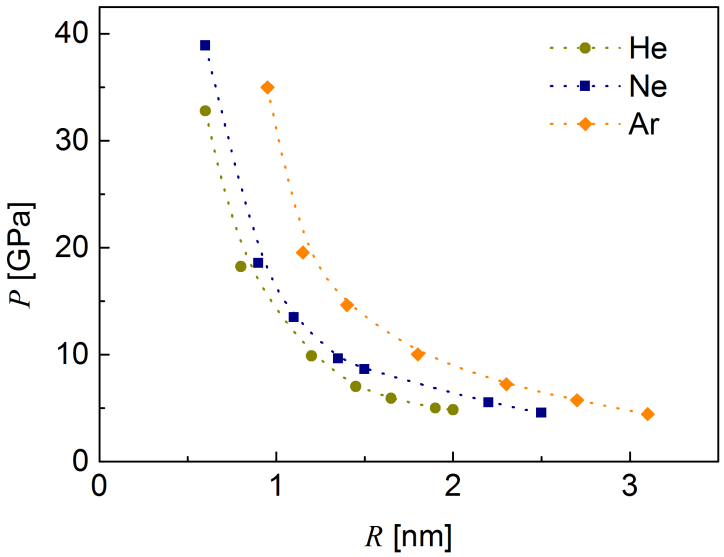

Figure 3.6: Pressure estimated from the MD simulations for He, Ne and Ar bubbles in graphene/Pt(111), as a function of bubble radius. The lines are guides to the eye.

$$P_{vdW} = - < \frac{Tr(\sigma)}{3V_b} > \tag{3.2}$$

where P_{vdW} is the van der Waals pressure, $Tr(\sigma)$ is the trace of the virial stress tensor and V_b is the volume available to the gas atoms. We note that this method, based on the virial stress tensor, is more general and more appropriate in the present case compared to other methods based on membrane theory and plate theory. These methods are based on elasticity theory, which is valid in the large bubble limit, but tends to overestimate the pressure for small bubbles [98].

3.6 Stability on Pt *versus* Instability on Cu

As mentioned above, unlike for Pt, bubbles are not observed on Cu flat terraces. It appears that only the atoms that are trapped in defects (*e.g.*, dips and terrace edges, as shown in Fig. 3.2) are immobilized as intercalated species. The remainder is likely to escape *via* graphene defects (*e.g.*, holes). This bubble instability for graphene on Cu is confirmed in our MD simulations: If a bubble configuration (similar to those in Pt) is given as the initial state, the time evolution shows graphene peeling off the Cu surface, resulting in the dispersion of the trapped gas atoms. This instability can be easily understood as due to the much weaker adhesion of graphene to Cu (γ_{GS} = 0.045 eV/Å^2 [116]) compared to Pt (0.251 eV/Å^2 [113]), that is, the Cu-graphene binding is too weak to sustain the high pressures associated with the bubbles. In order to assess if the gas-metal adhesion (γ_{Sb}) also plays a role in this stability difference, we used density functional theory (DFT) to calculate the adsorption energy and the adsorption distance of isolated He, Ne and Ar

atoms on Pt(111) and Cu(111) surfaces [56]. Although the adsorption energies are indeed larger for Pt than for Cu when comparing the gas elements one by one, it still does not explain the observed difference in stability. For example, the adsorption energies of Ar on Cu (for which bubbles are not stable) are larger than those of He on Pt (for which stable bubbles are observed). We therefore conclude that bubbles are not stable on flat Cu terraces due to the much weaker adhesion of graphene to Cu as compared to Pt.

3.7 Simulation parameters for molecular dynamics

We simulated the nanobubbles using molecular dynamics (MD). The simulation system comprised a graphene sheet spanned over Pt(111) and Cu(111) substrates, between which a varying number (from 6 to 800 atoms) of noble gas atoms (He, Ne and Ar) were inserted. The graphene sheet dimensions were 7.5×7.5 nm^2 and at the beginning, the middle region of the graphene was manually lifted to form an artificial bubble so that the trapped atoms could be accommodated. The substrate and the graphene sheet were modeled using the EAM [117] and Airebo potential [118] while the trapped materials, as well as the interactions among the substrate, graphene sheet and trapped materials, were modeled using 12/6 Lennard-Jones (LJ) potential. The LJ parameters were set according to ref. 119 for the trapped gases, ref. 120 for C and ref. 121 for Pt and Cu, and the cross parameters were calculated using Kong's formula [122]. The LJ interactions were cut off at 10 Å distances.

The system was initially subjected to an energy minimization using conjugate-gradient algorithm, followed by gradually heating the system from frozen to room temperature using Nose-Hoover thermostat. Next, the NVT simulation at room temperature was continued until the system exhibited steady state after which the quantities of interest were calculated. The MD simulations were carried out using the Lammps package [123] with Velocity-Verlet discretization of the Newtonian equation of motion and 1 fs time-step. The average out-of-plane motion amplitudes ($\langle \Delta z \rangle$) for the smallest bubbles was obtained by time-averaging among several states in equilibrium. The pressure inside the bubbles was calculated using the stress formulation [115].

3.8 Conclusion

To conclude, using ULE implantation of noble gas ions (He, Ne and Ar), we produced nanobubbles on graphene with varying radius, from few nm down to sub-nanometer. These nanobubbles are stable for graphene on Pt, but not for graphene on Cu. While the bubble aspect ratio behaves differently for the different elements, the universal scaling behavior (that was previously established for larger bubbles) breaks down in all three cases, for bubble radius around 1 nm, as the bubble height approaches a minimum corresponding to about an atomic monolayer. We interpret the observed dependencies on substrate and trapped element in terms of the adhesion energies between the three constituents: graphene, substrate and trapped noble gas element.

In addition to providing insight on the spatial distribution of the trapped atoms and its relation to the bubble morphology and stability, molecular dynamics calculations also allowed us to estimate the van der Waals pressure inside the bubbles. The extremely high pressures that we obtained, exceeding 30 GPa for the smallest bubbles, illustrate the unique characteristics of this sub-nanometer bubble regime (achievable using ultra-low energy ion implantation) compared to the previously studied nanobubbles. These unique properties offer new opportunities, for example, to study physical states of matter and chemical reactions under high (van der Waals) pressure, or electronic phenomena associated with strain-induced pseudomagnetic fields in graphene.

Since the behavior reported here is largely determined by the adsorption energies between the three constituents (2D material, substrate and trapped substance), one can expect similar behavior for other 2D materials (*e.g.,* transition metal dichalcogenides such as MoS_2), which expands even further the range of possible applications. In particular, since the bubble formation is based on ion implantation, our approach is compatible with virtually any implanted element, 2D material, and substrate.

Chapter 4

Indentation of graphene nanobubbles[¶]

In this chapter, we present the results of our molecular dynamics simulations, which are used to investigate the effect of an AFM tip when indenting graphene nanobubbles filled with a noble gas (i.e., He, Ne, and Ar) up to the breaking point. The failure points resemble those of viral shells as described by the Föppl–von Kármán (FvK) dimensionless number defined in the context of elasticity theory of thin shells. At room temperature, He gas inside the bubbles is found to be in the liquid state while Ne and Ar atoms are in the solid state although the pressure inside the nano bubble is below the melting pressure of the bulk. The trapped gases are under higher hydrostatic pressure at low temperatures than at room temperature.

4.1 Introduction

Van der Waals heterostructures consist of atomically flat thin materials which adhere to each other by van der Waals attraction [23]. The presence of contaminants is inevitable while fabricating these heterostructures. Contaminants may include several materials spanning from e.g. noble gases to water and hydrocarbons. Strong adhesion between the layers may squeeze out the contaminants into nano scale bubbles [34, 52, 98]. These bubbles were regarded as a signature of the adhesion between the layers. They were used in the investigation of the elastic properties of two-dimensional materials and to study the properties of highly confined materials [42, 43, 45, 46, 49, 50].

AFM nano indentation has been used to study the mechanics of thin materials including nano bubbles, as well as viral shells such as protein aggregates [52, 124]. Nano indentation may also be used to determine the hydrostatic pressure of the materials trapped inside the bubbles. An important question is: up to which size the bubble response against indentation can be described by continuum theories?

Here, we use molecular dynamics (MD) simulations to study the nano indentation of graphene nano bubbles. The noble elements He, Ne and Ar were used as trapped materials. We found that the bubbles exhibit structural failure upon high indentation. The

[¶] This chapter contributed to the paper: Indentation of graphene nano-bubbles. Nanoscale **14**, 5876–5883 (2022).

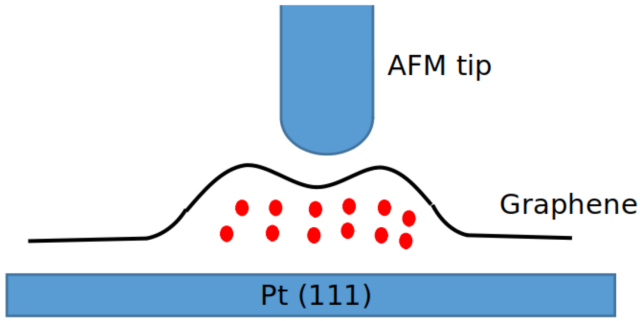

Figure 4.1: Schematic of the nano bubble system. Trapped materials are confined between the Pt substrate and the graphene sheet. A spheroidal tip was placed above the bubble which caused deformation of the graphene sheet.

failure deformation points and the linear response regime are well described by continuum theories. Furthermore, the bubbles exhibit resilience against periodic deformations prior to their failure points. The hydrostatic pressure of the trapped material was found to be highly sensitive to temperature, which was mostly due to the influence of temperature on the bubbles' geometry. In contrast to He, Ne and Ar elements show crystalline structure below their melting pressure at room temperature which is a distinct signature of the effect of very strong confinement on the properties of the trapped materials.

4.2 Simulation details

The simulated system consists of a substrate made of Platinum (Pt-111), a graphene sheet above the substrate, and a noble material trapped between the substrate and graphene. The substrate dimensions was taken to be 10×10×1 nm and the graphene sheet dimensions are 7.5×7.5 nm. At the start of the simulation, the graphene central region was manually lifted to form an artificial bubble which was filled by one of the three noble materials: He, Ne and Ar. A spheroidal surface tip with sphere radius of 2 nm (which corresponds to the smallest commercial AFM tip) made of silicon was placed above the graphene bubble. The tip had a FCC atomic structure with a lattice constant of 5.43 Å. Fig. 4.1 shows schematically the simulated system.

EAM [125] and AIREBO [117] potentials were used for the substrate and the graphene, respectively. The cut-off radii of the AIREBO potential were set to 0.2 nm, which has been demonstrated to eliminate non-physical strain hardening [126, 127] during strong stretching in graphene [128, 129]. We examined the potential by stretching a pristine graphene sheet and observed brittle breaking with a fracture stress of $\sim$ 107 GPa that agrees with the experimental results [130]. The trapped materials, as well as the van der Waals interactions among all elements were modelled using the 12/6 Lennard-Jones (LJ) potential. The employed LJ coefficients for different materials are summarised in table 4.1, while the cross parameters were calculated using the Lorentz-Bertholet mixing rule. The van der Waals interactions were cut off at 9.8 Å.

Table 4.1: Parameters for the interaction potentials

Atom type	σ_i (Å)	ϵ_i/k_B (K)	Ref.
Pt	2.54	7910	121
C	3.41	28	120
He	2.55	10	119
Ne	2.82	32	119
Ar	3.47	114	119
Si	3.33	103	121

The graphene and the trapped materials were initially subjected to an energy minimisation using the conjugate-gradient algorithm [131]. Then, their temperature was gradually increased from zero to the desired temperature after which NVT simulation was continued until the bubbles geometry, namely, its radius and maximum height, exhibited a steady configuration. Next, the tip was moved down with a constant velocity of 0.2 Å/ps until the tip touched the graphene and deformed it. We found the tip speed results in a strain rate of $\sim 9 \times 10^{-4}$ ps^{-1} in the graphene bond length (in the area under the indentation), which is typical in MD simulations [132]. During the simulations, we reduced the tip speed until we observed that further reducing the speed had little impact on the results. To explore the effect of temperature, we repeated the simulations at two temperatures including room temperature (T = 300K), and a low temperature (T = 5K). The newtonian equations of motion were integrated using the velocity-verlet algorithm with a time step of 1 fs. All simulations were carried out using the Lammps [123] package. Graphical snapshots are created using the Ovito software [133].

4.3 The bubble geometry

Once the bubbles exhibited a steady geometry, we measured the radius and maximum height of the bubbles filled by He, Ne or Ar at two temperatures: 5K and 300K. Moreover, to examine different bubble dimensions for each trapped element, the simulations were performed for two different number of trapped atoms N_t = 800 and N_t = 1100. Initially, the tip was placed sufficiently above the bubbles (more than the LJ cut-off radius) so that it did not affect the bubbles prior to the indentation. To measure the bubble radius and height, we plotted the cross section of the graphene sheets and heuristically defined the radius from the points where graphene started to move out of plane and the height was defined as the maximum vertical distance of graphene from the plane it defines away from the bubble.

The results for the bubble radius and maximum height for different trapped materials, as well as for the two temperatures and N_t are summarised in table 4.2. In general, the bubbles seem to follow the universal scaling in their height to radius aspect ratio [52]. It is worth mentioning that the bubbles' radius are sufficiently larger than 1 nm below which we recently have shown that a breakdown in the universal scaling is envisaged [56]. Notice that the aspect ratio values are in quantitative agreement with experiment (see Table (1) of ref. 56 for the large bubble regime). When comparing the bubbles radius for the same N_t, the Ar bubbles have the largest radius, followed by Ne and then He

Table 4.2: The radius and height of the graphene nano bubbles for different trapped elements, temperature and number of trapped atoms N_t

	T = 300K			T = 5K		
Gas/N_t	R(Å)	h(Å)	h/R	R(Å)	h(Å)	h/R
He/800	28.60	6.41	0.22	28.10	6.13	0.22
Ne/800	33.50	7.32	0.22	31.89	7.99	0.25
Ar/800	44.61	9.11	0.20	40.99	9.22	0.22
He/1100	33.48	7.33	0.22	33.33	7.42	0.23
Ne/1100	39.70	7.91	0.20	37.18	8.87	0.24
Ar/1100	48.21	9.92	0.21	46.60	10.92	0.23

bubbles. We attribute this to the van der Waals radius of the trapped elements which is the largest for Ar and the smallest for He (see table 4.1). For the same N_t and trapped material, the bubble acquire a larger radius at room temperature as compared to the low temperature results. This can be related to the higher adhesion energy γ between graphene and the substrate at low temperatures. Specifically, when temperature is high, the graphene atoms have higher kinetic energy with stronger vibrations, thereby having lower effective adhesion to the substrate. This resembles the effect of temperature in the standard capillary phenomenon. Therefore, at higher temperatures when the adhesion between graphene and the substrate (γ_{SG}) is lower, the trapped materials could detach the graphene sheet from the substrate more easily, thereby creating bubbles with a larger radius.

For the same trapped material and N_t, the low temperature bubbles exhibit higher maximum heights. To understand this, we should note that the bubbles boundaries are not clamped in the simulations, yet it is the interplay between γ_{SG} and the trapped materials hydrostatic pressure which determines the bubbles volume. The pressure is in turn influenced by the adhesion energy [52]. Our calculations show that the hydrostatic pressure of the trapped materials is surprisingly larger at low temperature than at room temperature (see the trapped materials: pressure and aggregation state section). Thus, when the bubbles exert higher pressures on the trapped materials at low temperatures, and concurrently, exhibit lower radius, it will lead to higher maximum heights as can be seen in table 4.2. This is especially noteworthy as at higher temperature, one would expect a higher maximum height because gas atoms have larger mobility and their structures are more out-of-plane [56]. Nevertheless, pressure induced by enhanced adhesion dominates such that the maximum height is higher at low temperature.

Further, if we accept that the trapped materials pressure is given by $P = \frac{4\pi\gamma}{5c_\nu h_{max}}$ (see Eq. (23) of ref. 52), where c_ν is a constant (≈ 1.7) which depends on the graphene poisson ratio, we find that the adhesion energy γ will be higher at low temperature to the extent that it compensates for both the higher pressure and maximum height. The latter equation was obtained by analytically minimizing the total energy of the nano-bubble system with respect to the bubble radius and maximum height, and empirically correlating the free parameters to the experimental data [52]. The total energy includes the elastic energy of the deformed graphene, the free energy of the trapped materials, and the vdW energy necessary to separate the graphene from the substrate [52].

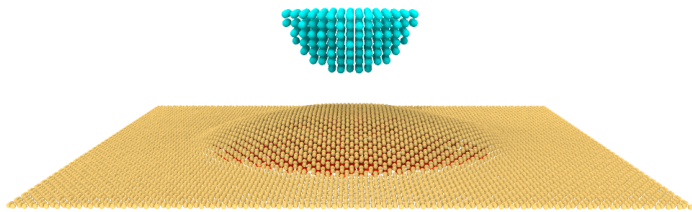

Figure 4.2: Schematic of the MD simulation system before the indentation for Ar bubble with $N_t = 1100$. A spheroidal surface tip with sphere radius of 2 nm made of silicon was placed above the graphene bubble.

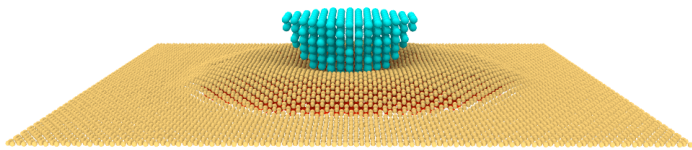

Figure 4.3: Schematic of the MD simulation system during the indentation for Ar bubble with $N_t = 1100$. The tip deforms the bubble until the point that the graphene sheet breaks.

4.4 Indentation force-deformation curves

Once the bubbles have reached their steady geometrical shape, we start moving down the tip. After touching graphene, the tip deformed the bubble until the point that the bubble eventually breaks and the graphene sheet ruptures. Snapshots from MD are shown in Figs. 4.2-4.5 which demonstrate the deformation and failure of the bubble as a result of the indentation. Fig. 4.6 illustrates the variation of the vertical force applied on the tip as the tip moves down and deforms the bubble at room temperature. Here, the horizontal axis is the indentation depth (δ) normalised by the corresponding bubble radius (R), and the vertical axis is the vertical component of the total force on the tip normalised by ($\sqrt{\kappa Y}$). Here, κ is the bending stiffness and Y is the two-dimensional Young modulus of the graphene sheet which at room temperature are equal to $\kappa = 0.24$ nN-nm and $Y = 340$ N/m.

As expected, the curves are ascending, that is, the indentation force increases with increased deformation. It can be seen that the curves are initially linear, and gradually become nonlinear for higher deformations. At least two partial drops (at $\delta/R \approx 0.06$ and 0.13) are discernible in the curves after which the curves become highly nonlinear followed by a dramatic drop. The partial drops in the curves are associated with the

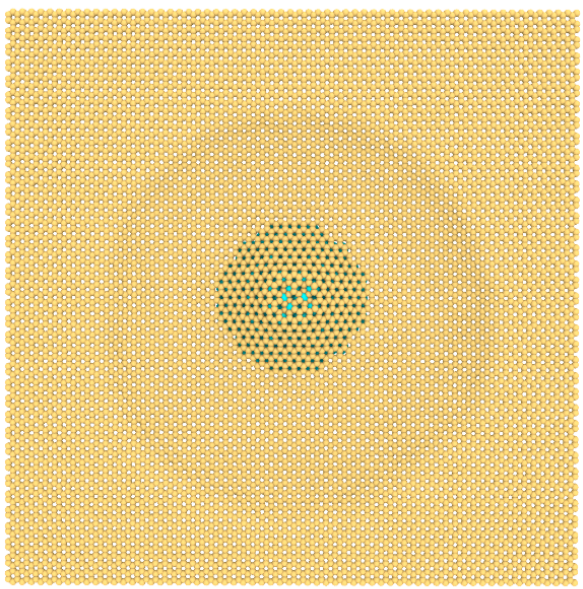

Figure 4.4: Schematic of the MD simulation system seen from the bottom for Ar bubble with $N_t = 1100$. The time frame is shown just before the graphene failure. The carbon bonds are under strong stretch. The substrate atoms are not shown here for a better illustration.

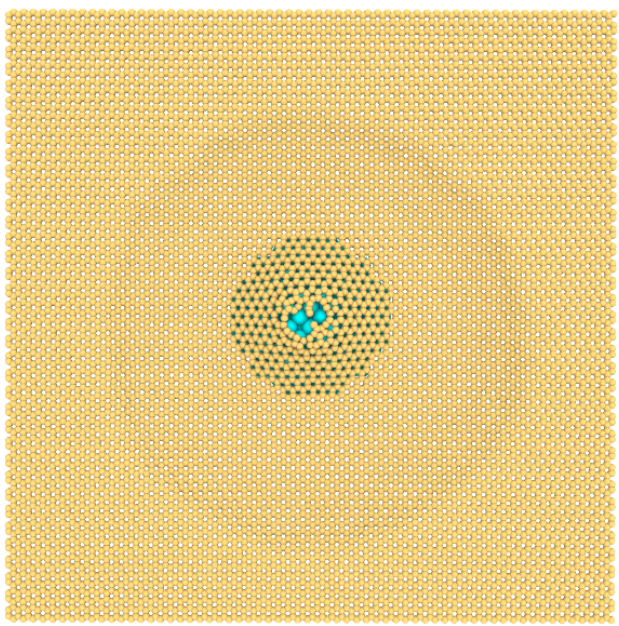

Figure 4.5: Schematic of the MD simulation system seen from the bottom after the graphene failure for Ar bubble with $N_t = 1100$. The substrate atoms are not shown here for a better illustration.

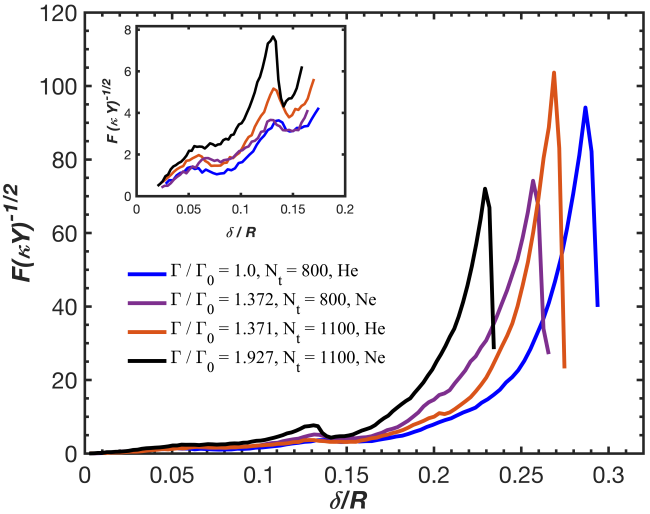

Figure 4.6: The force applied on the tip versus the bubbles deformation. The bubbles break at high deformations. The failure points can be described by Föppl–von Kármán (FvK) dimensionless number $\Gamma = \frac{YR^2}{\kappa}$. The inset magnifies the region of the partial drops associated with buckling transitions.

points where the energy of two different shapes of the graphene nanobubble cross each other which are commonly referred to as buckling transitions in the engineering literature [134] (see the inset of Fig. 4.6). The dramatic drop of the curves at high deformation are attributed to the failure of the graphene bubble.

Being similar in nature to pressurised vessels, one can ask oneself whether elasticity theory of thin shells [135] (TST) is helpful in interpreting the indentation of our bubbles. One important dimensionless number in TST is the so-called Föppl–von Kármán (FvK) number $\Gamma = \frac{YR^2}{\kappa}$ which for a perfect sphere represents the ratio of the magnitude of the in-plane stretching to the out-of-plane bending forces. In our problem, κ and Y are the same for all bubbles, so the bubble radius solely determines the FvK number (Γ). Using the aforementioned values for κ and Y, the FvK number for our He bubble with $N_t = 800$ at room temperature is calculated as Γ = 11,588 (which we will refer to Γ_0 hereinafter). The FvK values for the other bubbles normalised to Γ_0 are given as legend in Fig. 4.6. Interestingly, we see that the failure point of the bubbles can be predicted from their FvK number: the higher the FvK number the lower δ/R for bubble failure. This is valid to the extent that the FvK number of the He bubble with N_t = 1100 is quite close and slightly higher than that of the Ne bubble of N_t = 800, and the He bubble fails for a slightly lower δ/R. Interestingly, this description is similar to what has been reported in experiments on failure of viral shells [58]. Notice that, the failure force is not affected by the FvK number but it is affected by the trapped material.

Similar curves are found for low temperature (T = 5K) which is illustrated in Fig. 4.7. Contrary to room temperature, all the curves fail almost at the same δ/R (≈ 0.27). The Γ values in the legend of Fig.4.7 were calculated based on the κ and Y values at room temperature. Basically, these material properties depend on temperature, and specially

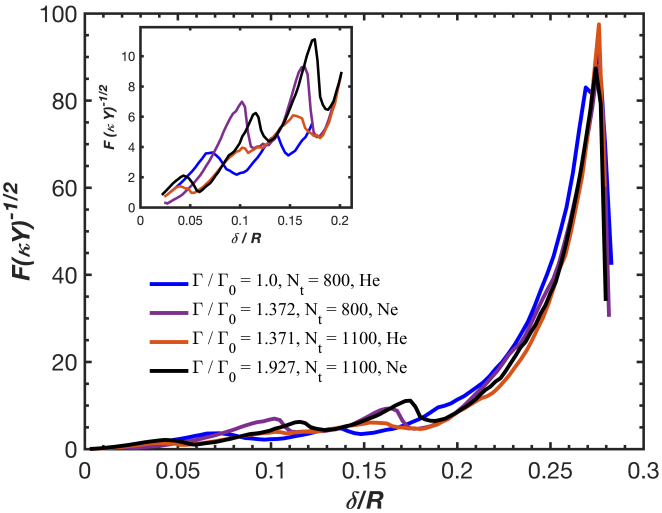

Figure 4.7: The force applied on the tip versus the bubbles deformation at T = 5K. The inset magnifies the region of the partial drops associated with the buckling transitions.

in the case of the bending stiffness, the issue is still under debate and the literature on it is controversial [136–138]. To further investigate this issue, we examined the local strain rates of Ne bubbles with N_t = 800 and N_t =1100 at room temperature and low temperature. Figs. 4.8-4.11 illustrate strain rates of the bond length across the graphene sheet for these four bubbles just before the graphene sheet failed. The maximum local strain for N_t = 800 bubbles is larger than for N_t = 1100 bubbles at both temperatures (see the maximum strain rate in the colour bars next to the contour plots). While the precise quantitative values of the local strain rates highly depend on the failure definition, as well as how often the MD data are extracted, the difference between the maximum local strain rates associated with the two N_t numbers is higher at low temperature than at room temperature. The difference at low temperature is four times larger. Therefore, at room temperature, bubbles rupture at relatively close deformations, so that when the deformation rate is normalised with the bubble radiuses (x-axis of Fig. 2), the difference between bubbles of different diameters (and consequently different FvK numbers) will be readily apparent. On the contrary, the failures at low temperature occur at different deformations such that after normalisation, the influence of deformation is canceled out by the influence of radius, and the curves drop at the same breaking point.

Additionally, it is evident that the maximum local strain rates are higher at low temperatures than at room temperatures (Figs. 4.10 and 4.11 compared to Figs. 4.8 and 4.9). It is in accordance with the fact that fracture stress of graphene increases with decreasing temperature [139]. In order to explain why the maximum strain rates at room temperature are close to each other as opposed to the results at low temperatures, we attribute it to graphene's increased flexibility at room temperature. By having ripples with enhanced amplitudes at room temperature, graphene becomes more adaptable, so that the area under stress in both N_t numbers becomes similar. At low temperature, graphene becomes rigid and N_t numbers (and radiuses) begin to show their influence. It is worth noting that at both temperatures, the influence of N_t numbers is more pronounced at the bubble

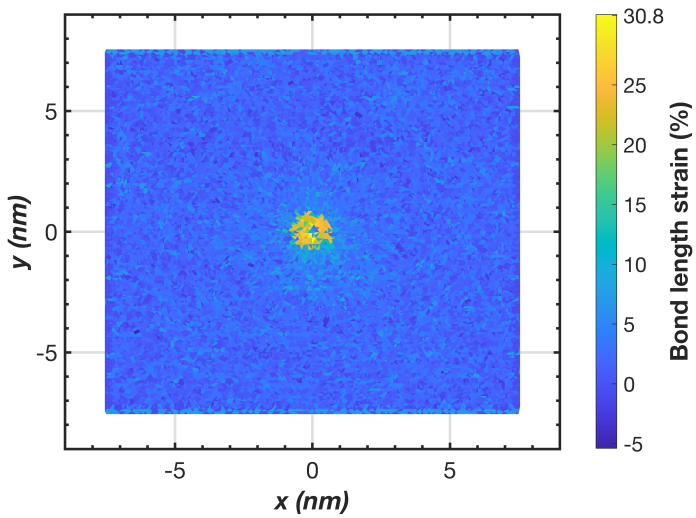

Figure 4.8: Strain rates of bond length across the graphene sheet for Ne bubble with N_t = 800 at room temperature.

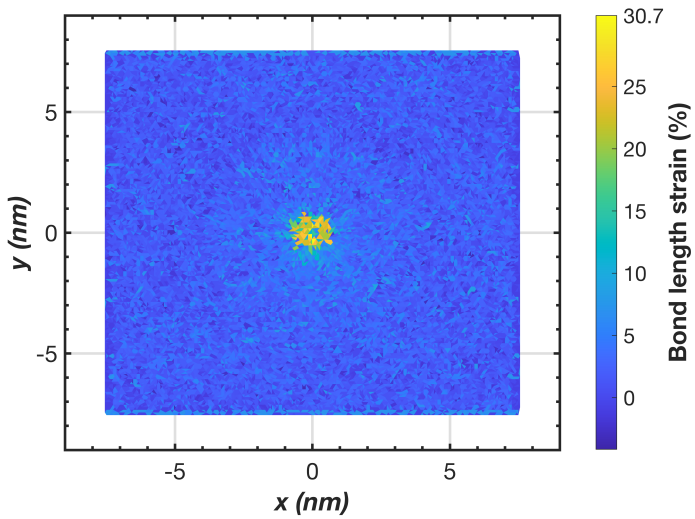

Figure 4.9: Strain rates of bond length across the graphene sheet for Ne bubble with N_t = 1100 at room temperature.

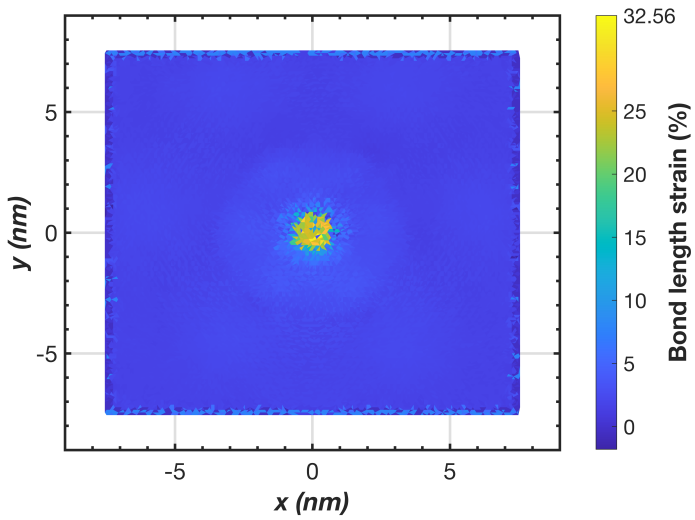

Figure 4.10: Strain rates of bond length across the graphene sheet for Ne bubble with N_t = 800 at T = 5K.

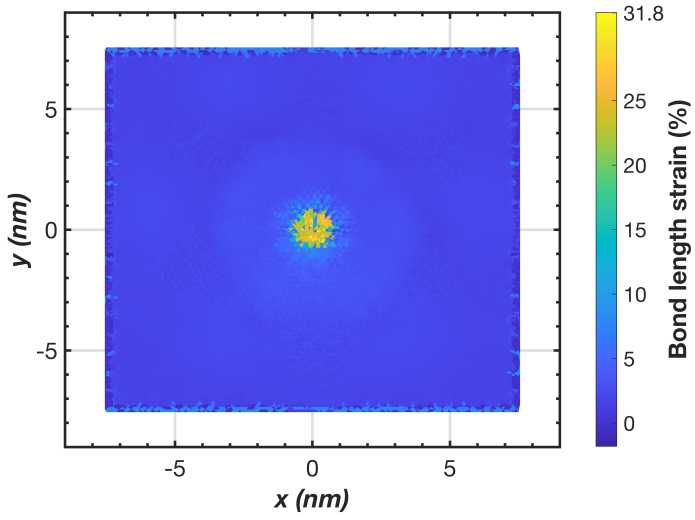

Figure 4.11: Strain rates of bond length across the graphene sheet for Ne bubble with N_t = 1100 at T = 5K.

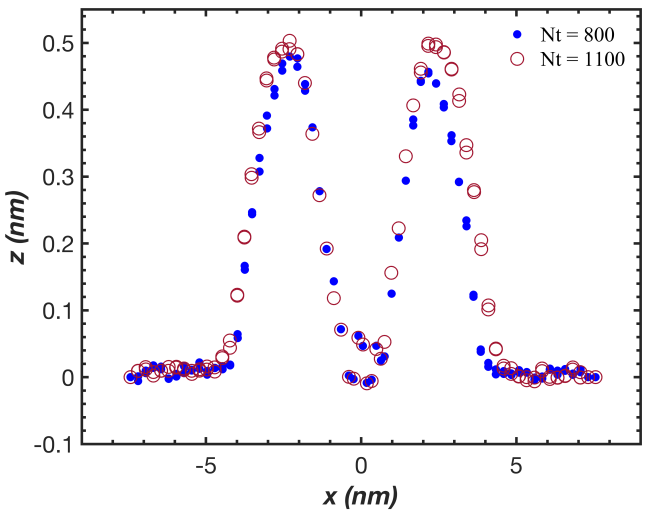

Figure 4.12: Cross section of the Ne bubble profile at the time frame before the graphene failure for N_t = 800 and N_t = 1100 at room temperature.

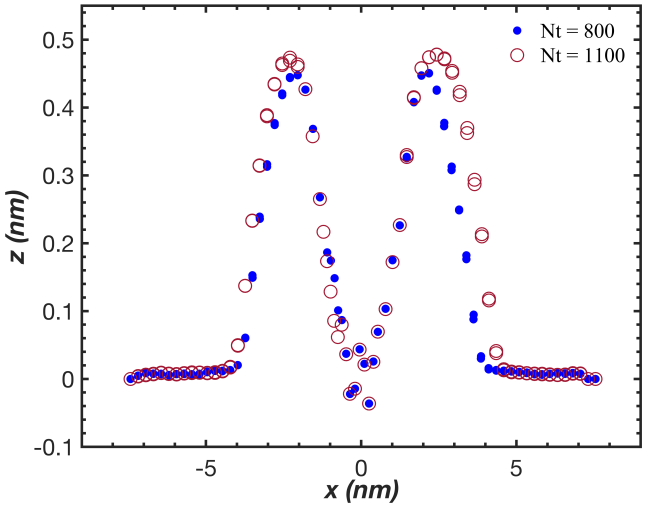

Figure 4.13: Cross section of the Ne bubble profile at the time frame before the graphene failure for N_t = 800 and N_t = 1100 at T = 5K.

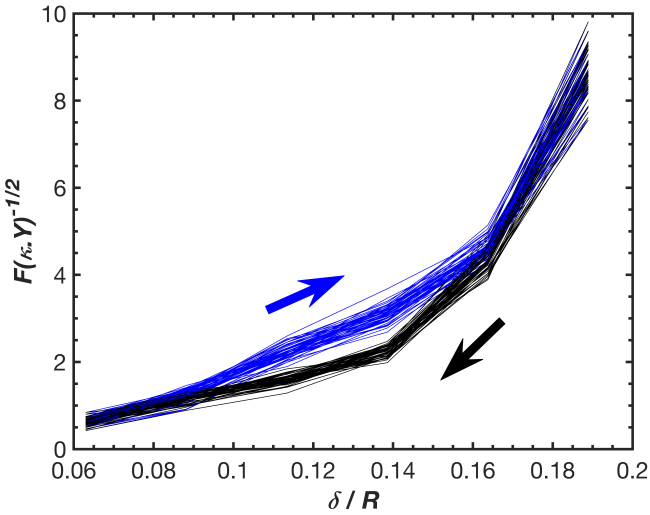

Figure 4.14: The force-displacement curve for periodic indentation after 50 cycles for a Ne bubble with number of trapped atoms $N_t = 800$ at room temperature. The bubble is resilient against fatigue. Irreversibility in the curves develops after the partial buckling transitions resulting in hysteresis in the curves.

edges rather than the stress area (see Figs. 4.12 and 4.13). A quantitative investigation of how the breaking point is sensitive to the changes of FvK number over a continuous temperature range is beyond the scope of the current work. Nevertheless, we expect that the sensitivity gradually decreases from room temperature to a point of insensitivity at low temperature. It is envisioned that at higher temperatures, the sensitivity will increase until a saturation asymptote.

Lastly, we investigated the reversibility of the deformations, and whether or not our graphene nano bubbles are vulnerable against periodic indentations, similar to the concept of fatigue. For this purpose, we applied a cycling back and forth indentation to the Ne bubble of $N_t = 800$ at room temperature until the deformation $\delta/R = 0.20$ which is before the bubble failure, yet after the two partial buckling transitions. Fig. 4.14 illustrates the resulted force-deformation curves after 50 cycling indentations. The bubble indeed exhibits resilience against fatigue while clear hysteresis can be observed. The hysteresis starts to develop after the first bucking transition, before which the deformations are reversible for small indentation. We also examined the fatigue and reversibility for the same bubble at low temperature. Its graph is similar to Fig. 4.14 and is given in Fig. 4.15.

4.5 Elasticity theory of thin shells (TST)

For small indentations when the relation between the indentation force and the deformation is still linear, TST predicts the total free energy H of a pressurised shell of a perfect sphere system as

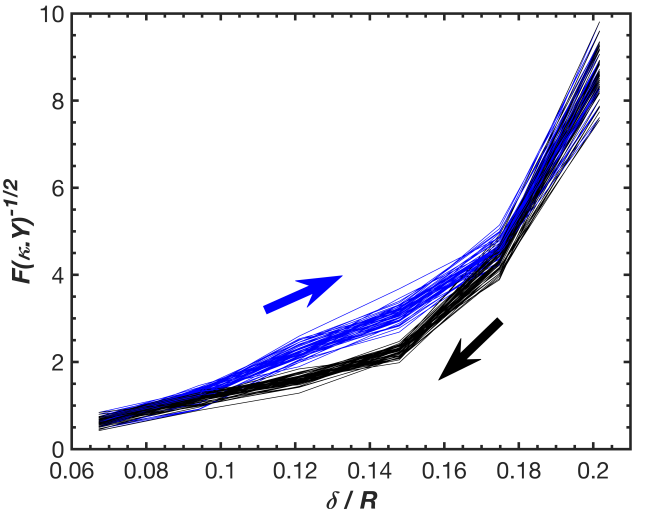

Figure 4.15: The force-displacement curve for periodic indentation after 50 cycles for Ne bubble with N_t = 800 at T = 5K.

$$H = \int dS\{\frac{1}{2}\kappa(\Delta\zeta)^2 + \frac{1}{2}\tau(\Delta\zeta)^2 + \frac{1}{2}\gamma(\frac{2\zeta}{R})^2\} \tag{4.1}$$

where $\zeta = \zeta(r)$ is the indentation profile, τ the osmotic pressure, and dS the surface differential. Minimizing the energy with respect to the indentation profile yields $F.R \approx 8\sqrt{\kappa Y}\zeta$ for the case of zero osmotic pressure. This means that the shell acts like a simple harmonic spring with a spring constant of $K_1 = 8\sqrt{\kappa Y}/R$. Nevertheless, by taking into account the osmotic pressure, two springs in series are formed, one originates from the shell elasticity and the other from the inside pressure.

Table 4.3 summarises the K_1 values calculated for the four bubbles shown in Fig. 4.6, as well as the slope of their curve (K_{MD}) before the first buckling transition where the curves are linear. Comparing the results, we see that TST relatively underestimates the slope of the curves, however the values are still of the same order of magnitude.

One should note that our nano bubbles are not perfect spheres which violates the initial assumption of Eq. 4.1. Moreover, the bubbles support hydrostatic pressures of the order of GPa (see the trapped materials: pressure and aggregation state). Therefore, the calculated K_1 values from TST, while neglecting the osmotic pressure, are expected to underestimate the slope of the curves.

Comparing the K_{MD} results, we can see that the values for N_t = 800 are higher than for N_t = 1100. The low N_t bubbles have smaller radius, thereby having higher shell spring constant as is evident in the K_1 formula. Nevertheless, the K_{MD} values of the Ne atoms are clearly larger than for the He bubbles, even comparing the Ne bubble of N_t = 800 and He bubble of N_t = 1100 whose shape were rather identical (refer to table 4.2). We will show in the followings that, for the same N_t, the trapped materials hydrostatic pressure are distinctly larger for the Ne bubbles than for the He bubbles. Hence, the higher K_{MD}

Table 4.3: Force-deformation curves slope calculated from MD and continuum theories

N_t	800		1100	
Gas	He	Ne	He	Ne
K_{MD} (N/m)	88.66	98.23	56.49	82.44
$K_{1,TST}$ (N/m)	25.27	21.57	21.58	18.20
$K_2 = \pi PR$ (N/m)	13.48	16.69	14.17	16.77

values for the Ne bubbles further emphasises the significance of the spring originating from the trapped materials hydrostatic pressure.

Alternatively, using the analytical methods of ref. 140, the force-deformation slopes (F/δ) can be estimated as $K_2 = \pi PR$. Values of K_2 for the same bubbles are also summarised in table 4.3. The latter relation has been obtained by ignoring the shell out of plane bending energy and we restricted ourselves to the in-plane stretching energy. The length scale κ/Y representing the ratio of the bending to stretching forces is ~ 0.25 Å for graphene, which is far below our smallest bubbles maximum heights (6.4 Å). Therefore, ignoring the bending energy is a reasonable approximation. Arithmetic summation of the K_1 and K_2 values, as two springs in series, would get us closer to the K_{MD} values. We conclude that the TST relations for perfect spheres provides us with a simple interpretation of the force-deformation slopes for small deformation.

Using TST in interpreting the force-deformation slopes after the buckling transitions where the curves exhibit highly nonlinear behaviour involves solving the highly nonlinear sets of differential equations known as the Föppl–von Kármán equations . These equations cannot be solved analytically and necessitates numerical computations such as finite-element analysis which are beyond the scope of our study. This further points out the significance of molecular simulations in studying the mechanics of graphene nano bubbles.

It is worth noting that TST commonly predicts nonlinearity of the force-deformation curves in deformations beyond the length scale $\sqrt{\kappa/Y}$. For our smallest bubble (He bubble of $N_t = 800$), this yields $\delta/R \approx 0.01$, while our nano bubbles exhibited linear behaviour until $\delta/R \approx 0.05$ (see Fig. 4.6), which further extends the applicability of the continuum theory.

4.6 The trapped materials: pressure and aggregation state

Graphene nano bubbles have been known to withstand extreme hydrostatic pressures [96]. Since the pressure of the trapped materials originates from the van der Waals adhesion between the graphene sheet and the substrate, it is customary to refer to it as the van der Waals pressure [52]. Next, we calculate the trapped materials hydrostatic pressure during the indentation of the bubbles.

The pressure values were calculated using the stress formulation [115] that was found to be valid for systems even away from either equilibrium or homogeneity. Fig. 4.16 illustrates the values of the pressures for Ne bubbles versus the tip displacement, for

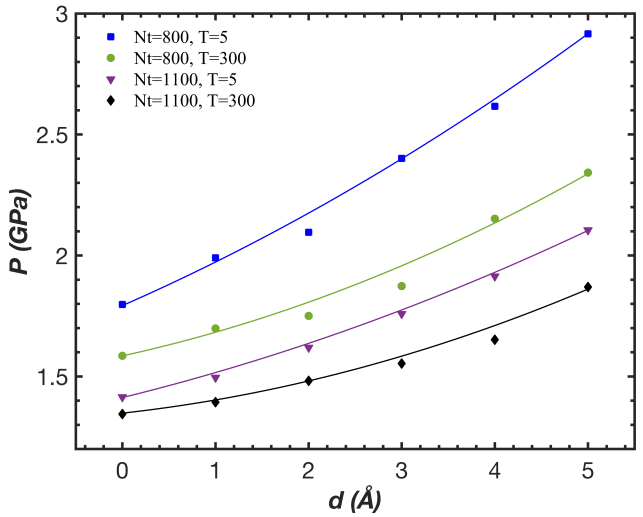

Figure 4.16: Trapped materials hydrostatic pressure for Ne bubbles as function of tip displacement for different N_t and temperatures. The curves are guide to the eye.

different values of N_t and temperature. The pressure values for He and Ar bubbles are illustrated in Figs. 4.17 and 4.18. It is worth reviewing how the pressure is calculated here. Under hydrostatic condition, a simple force balance for an infinitesimal volume inside the system yields the hydrostatic pressure [115] to be as $P = \frac{1}{3}(\sigma_{xx} + \sigma_{yy} + \sigma_{zz})$ where σ_{xx}, σ_{yy} and σ_{zz} are the internal normal stress components. The normal stress can then be determined with the summation of two terms including: the interatomic forces and the momentum flux due to the inner-diffusion of the atoms.

In the following we will find that the trapped materials of Ne and Ar bubbles are in the solid state, and exhibit a crystalline structure. For He bubbles they are in the liquid state with restricted inter-diffusion. Therefore, atomic movements away from their crystalline lattices are not anticipated, and the bubbles' pressure stems from the first term of the normal stress, that is, the interatomic interactions. Comparing the results, we notice that the pressure of Ne bubbles, for the same N_t, are larger than for He and Ar bubbles. The stronger interatomic interaction of Ne atoms as compared to He atoms results in higher pressure inside the Ne bubbles than He bubbles. Ar bubbles, on the other hand, although have stronger interactions, acquire much larger volumes which suppresses the effect of atomic interactions resulting in a lower pressure of Ar bubbles than Ne bubbles.

Surprisingly, the pressure graphs show that the trapped materials have higher pressure at low temperature than at room temperature. We found in table 4.2 that the bubble radius is smaller at low temperature. Graphene compresses the trapped materials in the radial direction more at low temperature than at room temperature, and it is as if a substance is subjected to an external compression ensuing normal stresses inside the substance. A possible argument could be that some of the trapped materials are in the solid state, and therefore the force balance of the stress formulation should involve shear stresses as well, as solids, contrary to liquids, withstand shear stresses at equilibrium. Our MD calculations shows shear stresses for all bubbles that are one order of magnitude smaller

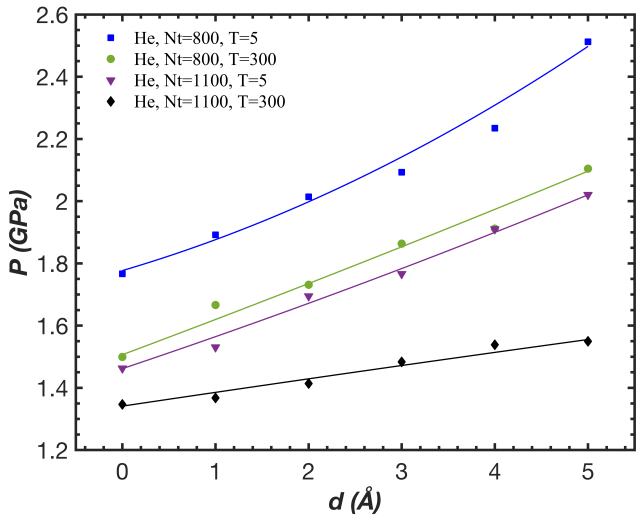

Figure 4.17: Trapped materials hydrostatic pressure for He bubbles as function of tip displacement for different N_t and temperatures. The curves are guide to the eye.

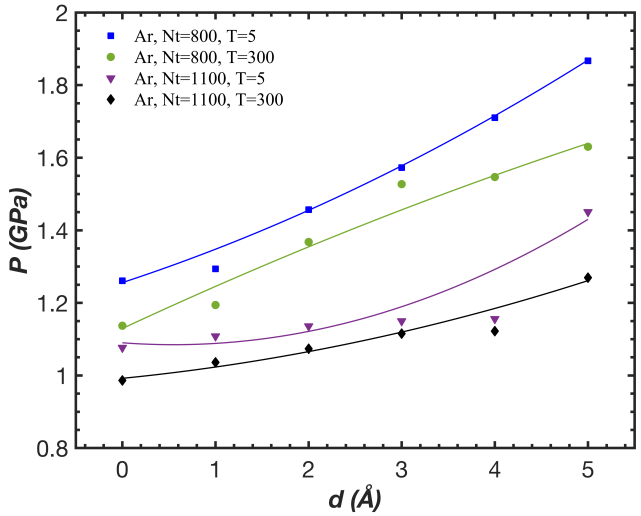

Figure 4.18: Trapped materials hydrostatic pressure for Ar bubbles as function of tip displacement for different N_t and temperatures. The curves are guide to the eye.

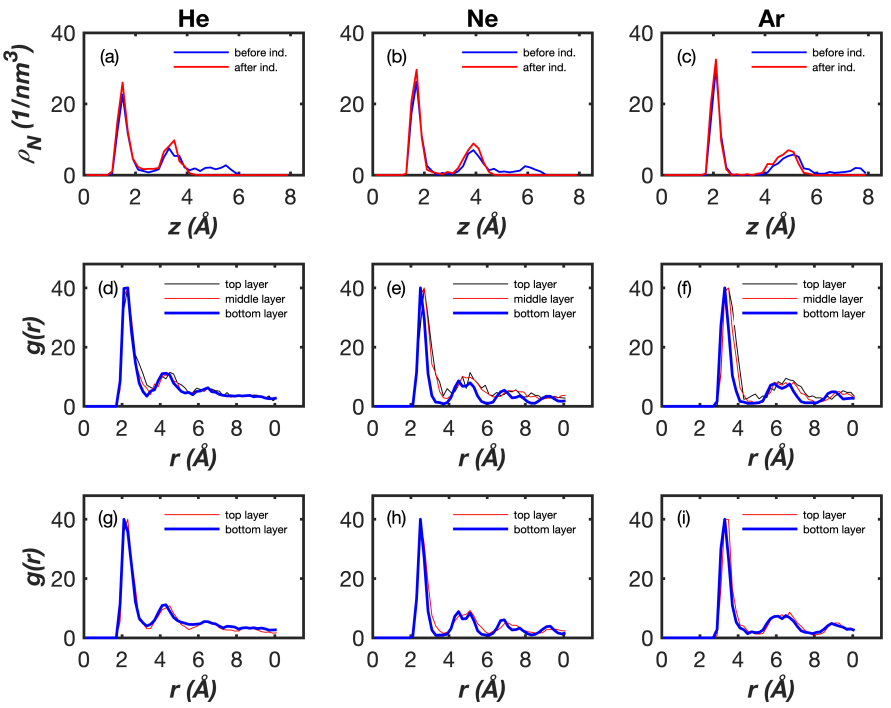

Figure 4.19: Number density graphs for bubbles at room temperature before and after the indentation. The trapped materials apparently exhibit a layered structure. Indentation reduces the number of materials layers by one (a-c). Radial distribution function (RDF) for each of the three layers of trapped materials before the indentation (d-f) and the two layers of trapped materials after the indentation (g-i). The He atoms show a liquid state while Ne and Ar atoms exhibit a more crystalline structure.

than the normal stresses, therefore would have minor influence on the force balance.

The pressure values increase with increased indentation. As expected, with increasing external force from the tip, the normal stresses inside the trapped material increases, and consequently the pressure increases. Moreover, we will show in the following that the indentation increases the trapped materials' surface to volume ratio, and the pressure in a solid material is expected to increase with increased surface to volume ratio [114].

To further understand the structure and aggregation state of the trapped materials at room temperature, we calculated the radial distribution function (RDF) and the number density distribution of the trapped materials (in the direction perpendicular to the substrate) for times before the indentation and after the indentation in the last time frames prior to the graphene failure. Fig. 4.19 (a-c) illustrates the number density distributions before and after the indentation. The graphs exhibit a layered structure. The trapped material has three distinct layers before the indentation which is reduced to two layers upon indentation. This explains the increase of the trapped materials surface to volume ratio.

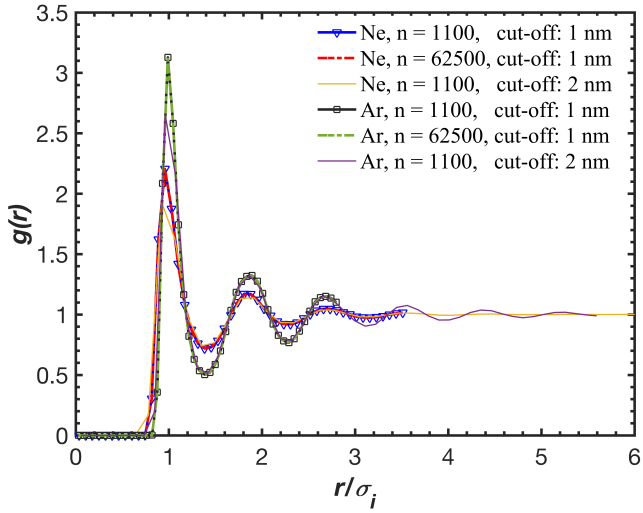

Figure 4.20: Radial distribution functions for Ne and Ar gases simulated with Lennard-Jones (LJ) potential in an isothermal-isobaric (NPT) ensemble (at room temperature and corresponding bubble pressure) for different system size and MD cut-off radius.

Fig. 4.19 (d-f) illustrates the RDF graphs for each of the three layers of the trapped materials (identified in the number density graphs) before the indentation. The curves of the three layers are more or less the same. We depicted the curves for the bottom layers which contain the majority of atoms in each bubble with thicker lines for a better illustration. RDF graphs exhibit only a second peak for He atoms while there are additional peaks for Ne and Ar atoms indicating that He atoms are in the liquid state while Ne and Ar atoms are in the solid states. A look at our MD trajectories confirm that Ne and Ar form a stable crystalline structure, while He show a more disordered atomic arrangement yet with restricted dynamic arrangements. We conclude that Ne and Ar are in the solid state and He is in the liquid state.

Similarly, Fig. 4.19 (g-i) shows the RDF graphs for the two layers of trapped materials after the indentation. The curves for each material are similar to those before the indentation suggesting that the influence of indentation on the trapped materials' aggregation state is not that significant. The plotted results are for $N_t = 800$, while the results for $N_t = 1100$ are very similar.

We compare the trapped materials' pressure with the solidification pressure of their bulk condition. Parameterisations of Simon's law for He [141], Ne [142] and Ar [141] yield solidification pressure at room temperature of $P_s = 12.09$ GPa for He, $P_s = 4.79$ GPa for Ne, and $P_s = 1.35$ GPa for Ar. Interestingly, the calculated pressure of Ne and Ar bubbles (1.59 GPa and 1.14 GPa, respectively) are below their bulk solidification pressure. We attribute this to the effect of strong confinement which further elucidates the effect of confinement on the materials properties.

Lastly, in order to verify that the solidification results from the effect of confinement and not from the LJ model, we performed a few extra simulations. With the same LJ parameters used here, we simulated Ne and Ar gases in an isothermal-isobaric (NPT) ensemble

(at room temperature and the corresponding bubble pressures) within a periodic box. The uncertainty in the prediction of melting lines in LJ models can be attributed to the size effect or the MD interaction cut-off [143]. Therefore, we repeated the simulations with two different numbers of atoms (1100 and 62500), using 1 nm or 2 nm cut-off distances in each case. Fig. 4.20 illustrates RDF graphs for different cases showing that the gases are in the liquid state, so we can infer that the solidification of the trapped materials inside the bubbles originates from confinement.

4.7 Conclusions

We investigated the effect of nano indentation of graphene nano bubbles using molecular dynamics simulation. The bubbles structural failure can be predicted from the elastic properties of graphene and the bubbles radius in terms of the Föppl–von Kármán (FvK) dimensionless number. The continuum elasticity theory of thin shells qualitatively explains the linear response of the bubble against the force applied from the indentation tip. The bubbles do not degrade while being subjected to cycling deformations when below the failure point. Ne and Ar atoms inside the nano-bubble are ordered into a crystalline state for pressures lower than their bulk melting pressure because of the highly confinement. This study sheds light on the important feature of nano-indentation of nano-bubbles.

Chapter 5

Flat nanobubbles encapsulated by hexagonal boron nitride[¶]

Different-shaped nanoscopic bubbles emerge when encapsulated within two-dimensional hexagonal boron nitride (hBN). Within these hBN bubbles, flat islands manifest, corresponding to specific molecular monolayers. Upon heating, these bubbles rapidly transition from flat to round shapes. Our experimental findings are supported by molecular dynamics simulations, highlighting the crucial role of hydrogen bonds in shaping these nanoscopic structures. Furthermore, our study unveils the chaotic behavior exhibited during heating, showcasing a diverse array of bubble shapes influenced by the heating rate.

5.1 Introduction

In the synthesis of structures comprising layers of two-dimensional (2D) materials, the presence of unavoidable environmental impurities becomes trapped between these 2D layers. Driven by van der Waals attraction among these sheets, these impurities compress into microscopic and nanoscopic bubbles. These bubbles have gained considerable attention in both scientific and technological applications in recent years [53, 57, 144–146].

Within the spectrum of 2D materials, boron nitrides exhibit fascinating thermal, electrical, and mechanical properties, some of which surpass even those of graphene [147–149]. Previous investigations were predominantly focused on graphene membranes, with less attention given to boron nitride, an ionic material that is softer and more easily deformable than graphene. Hence, the exploration of bubbles formed in monolayer hexagonal boron nitride (hBN) holds significant importance.

The shape of these nanobubbles is intricately influenced by a complex interplay of factors, including the elastic properties of the 2D materials, the adhesion between the 2D material and the substrate, and the hydrostatic pressure exerted by the trapped substances [52, 59]. Theoretical and experimental studies suggest that hBN bubbles with a radius smaller than 200 nm tend to adopt a round shape [52]. As these bubbles grow in size, they exhibit

[¶] The experimental results of this chapter are from the group of Prof. Irina Grigorieva at the University of Manchester.

a tendency toward triangular shapes with smooth edges, eventually transitioning into pyramid formations for bubbles at the microscale [52].

Drawing on the theory of elasticity of membranes, Khestanova et al. [52] demonstrated that for round-shaped bubbles, the bubble geometry adheres to a universal aspect ratio (height-to-radius). This ratio is influenced by the adhesion energy between the two crystals and the Young's modulus of the deformed two-dimensional crystal. Notably, nanobubbles in monolayer hBN on graphene consistently display an aspect ratio ranging between 0.10 and 0.15. Through scanning tunneling microscopy (STM) measurements and molecular dynamics (MD) simulations, however, we have uncovered that the universal scaling breaks down as the bubble radius approaches 1 nm or less [56]. Nevertheless, our recent experiments unveil intriguing, previously unobserved results: nanobubbles formed by a monolayer of hBN on an hBN substrate display small, flat islands at only two distinct heights (~0.4 nm and ~0.8 nm). When subjected to heat, these flat bubbles transform into round shapes.

In this chapter, we briefly introduce some experimental observations, followed by presenting the results of our molecular dynamics simulations to delve into the underlying physics of these phenomena. It is revealed that, in addition to the previously mentioned criteria, the distribution of hydrogen bonds between the atoms of the trapped substances and the nitride acceptors within the hBN sheets plays a pivotal role in determining bubble shapes. Additionally, the influence of heating on altering bubble shapes is found to be chaotic, with different shapes envisioned based on the speed at which the heating occurs.

5.2 Experimental Setup and Procedures

Bubbles formed by a monolayer of hexagonal boron nitride hBN on an hBN substrate exhibit small, flat islands at only two distinct heights (approximately 0.4 nm and 0.8 nm) across various standard samples. These heights correspond to one and two monolayers of trapped molecules (see Fig. 5.1). Furthermore, when subjected to heat, these flat bubbles undergo a transformation into round shapes. Specifically, at 160 °C, the height abruptly shifts from approximately 0.4 to 0.9 nm (see Fig. 5.2).

5.3 Molecular Dynamics Simulations

5.3.1 Methodology and Parameters

We employ molecular dynamics simulations to investigate the geometry of nanobubbles formed within hexagonal boron-nitride (hBN) heterostructures. The trapped materials within these nanobubbles are simulated using decane ($C_{10}H_{22}$) hydrocarbon molecules. Additionally, for comparative analysis, we conduct simulations involving nanobubbles composed of graphene sheets or containing water molecules.

The literature reports varying values for the static charges on boron and nitrogen atoms in hBN sheets, ranging from 0 to 1.05e [150–154]. The ambiguity arises from challenges in

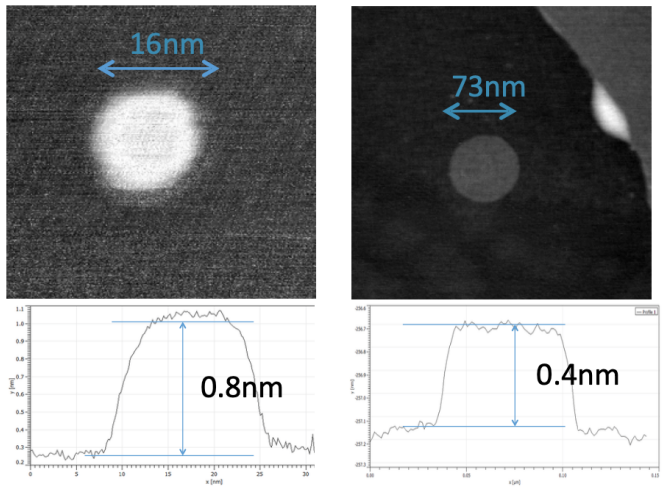

Figure 5.1: Small, flat islands showcasing two characteristic heights in hBN bubbles.

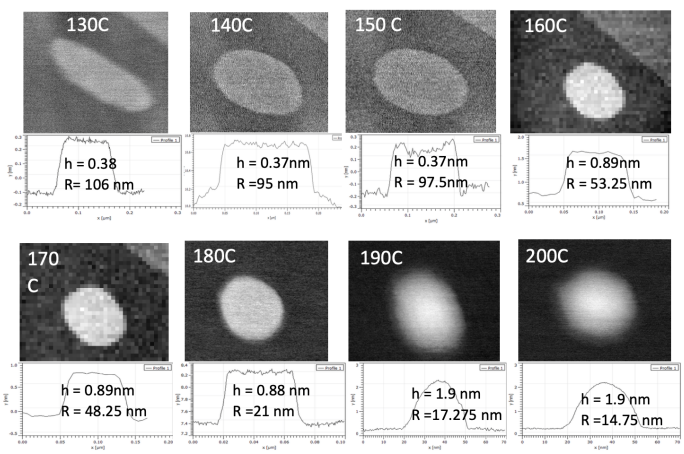

Figure 5.2: The transition from flat to round bubbles observed after baking at 160 °C.

distinguishing electron densities between atoms of different elements. In our simulations, we adopted a mid-value of 0.42e for static charges. Importantly, we verified that our primary findings exhibit consistency across the range of static charges.

To simulate the bonds, angles, and dihedrals of the decane molecules, Optimized Potentials for Liquid Simulations (OPLS) [155] have been used. The water molecules were also simulated using the SPC/E model. An optimised Tersoff potential [156] has been used for hBN or graphene sheets. We calculate non-bonded interactions using the Lennard-Jones (LJ) formula for van der Waals and the point charge electrostatic formula for electrostatic interactions. The parameters for the non-bonded interactions between all of the species, including the inter-layer interactions between hBN and graphene sheets are set as gathered by ref. 157. The Lorentz-Berthelot mixing rules are used to calculate cross parameters.

We utilized the particle-particle particle-mesh (P^3M) algorithm [158] to accurately compute long-range electrostatic interactions in k-space with a precision of 1×10^{-4}. The SHAKE algorithm was employed to maintain the rigidity of water molecules. The simulations were conducted employing LAMMPS [123], utilizing the velocity-Verlet discretization of the Newtonian equation of motion with a time step of 1 fs.

5.3.2 Results and Discussion

5.3.3 Room Temperature Simulations

Our molecular dynamics investigations proceeded as follows. Initially, we simulated 150 decane molecules confined between two hBN sheets at room temperature. Fig. 5.3 shows the cross section of the nanobubble profile. With one layer of hydrocarbon molecules and a height of 0.49 nm, the bubble profile exhibits a predominantly flat morphology.

We extended our simulations to investigate a nanobubble filled with 1000 water molecules at room temperature (see Fig. 5.4). Similar to the hydrocarbon-filled bubble, this configuration also reveals a flat profile with only one layer of trapped materials, measuring a height of 0.39 nm.

Comparing this water-filled bubble with its counterpart formed between graphene layers, which is anticipated to have an aspect ratio of approximately 0.15 [52], the hBN-encased bubble stands out for its distinctly flat profile. Further exploration involved repeating the simulation with the atomic charges of the hBN atoms turned off. In this case, the bubble adopted a spherical shape with a height of 0.87 nm and a radius of 4.79 nm (aspect ratio of 0.18, as expected; see Fig. 5.5).

This observation leads us to hypothesize that the partially negatively charged nitride atoms in the hBN sheets serve as acceptors, forming hydrogen bonds with the hydrogen atoms of the water molecules. This configuration allows the water cluster to arrange itself to maximize the interface with the hBN sheets, resulting in a one-atomic-layer bubble. When atomic charges are turned off, a spherical bubble shape emerges due to the interplay between van der Waals attraction between sheets, pressure from trapped materials, and the elastic properties of the sheets [52, 59].

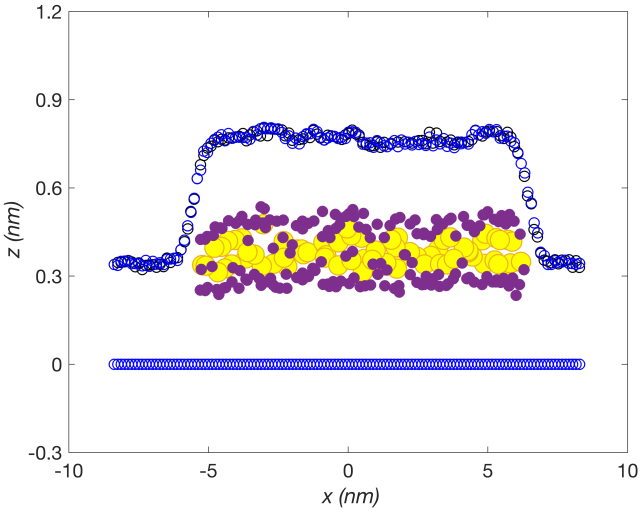

Figure 5.3: Cross-section of the nanobubble profile with top and bottom layers made of hBN. The trapped material consists of decane hydrocarbon molecules, denoted by large (carbon) and small (hydrogen) circles.

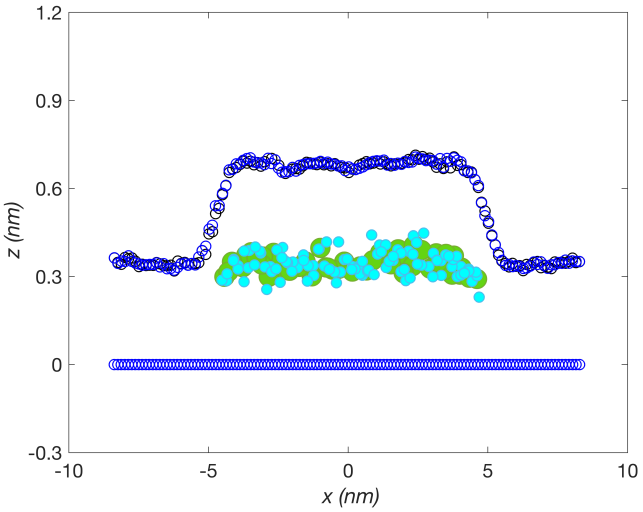

Figure 5.4: Cross-section of the nanobubble profile with top and bottom layers made of hBN. The trapped material consists of water molecules, denoted by large (oxygen) and small (hydrogen) circles.

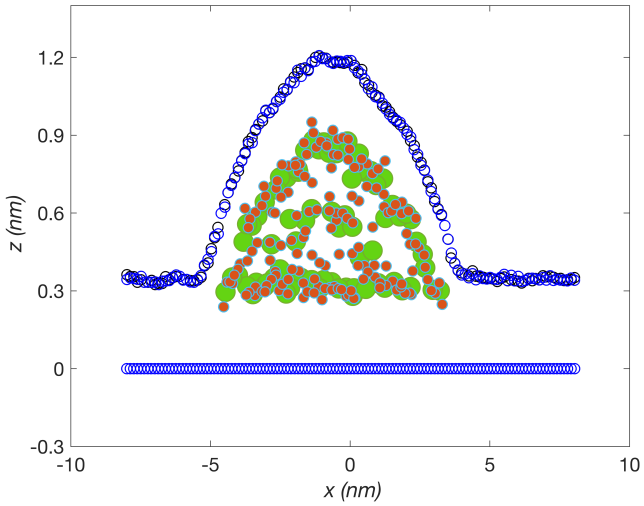

Figure 5.5: Cross-section of the nanobubble profile with top and bottom layers made of hBN. The trapped material consists of water molecules, denoted by large (oxygen) and small (hydrogen) circles. In the hBN layers, atomic charges are artificially turned off.

As an additional demonstration, we conducted simulations of a bubble containing 1000 water molecules at room temperature. However, in this case, instead of hBN sheets, two graphene sheets constituted the bubble. As anticipated, the result is a spherical bubble (see Fig. 5.6) with a height of 0.73 nm and a radius of 5 nm (aspect ratio of 0.15).

In another scenario, we simulated an intermediate situation where a bubble, filled with 1000 water molecules at room temperature, consists of an hBN sheet on the top and a graphene sheet on the bottom (see Fig. 5.7). Once again, the observed profile is flat, with a single layer of water molecules measuring 0.4 nm in height. This outcome suggests that hydrogen bonds with only one layer are adequate to maintain the flattened structure of the bubble.

Having established the crucial role of hydrogen bonds, we investigated whether a similar scenario arises with bubbles filled with decane hydrocarbon molecules. Given that the hydrogen atoms of decane molecules also form hydrogen bonds with the nitride acceptors of hBN sheets, we repeated the simulation of the aforementioned bubble (150 decane molecules) between two hBN layers, with artificially turned-off atomic charges (see Fig. 5.8). Interestingly, the resulting bubble profile remains flat, in contrast to our observations with water. To further explore this phenomenon, we replicated the simulation for 150 decane molecules between two graphene sheets (see Fig. 5.9) and between a top hBN sheet and a bottom graphene sheet (see Fig. 5.10), all conducted at room temperature.

All the aforementioned bubbles exhibit flat profiles with a consistent height of 0.49 nm. This prompts the question: why do bubbles containing water differ in behavior from those containing decane molecules? We attribute this distinction to the hydrostatic pressure exerted by the trapped materials inside the bubble. Qualitatively, pressure is proportional to $\rho T/M$, where ρ denotes density, T is temperature, and M represents molecular mass. Given that decane has lower density and much higher molecular mass than water, the

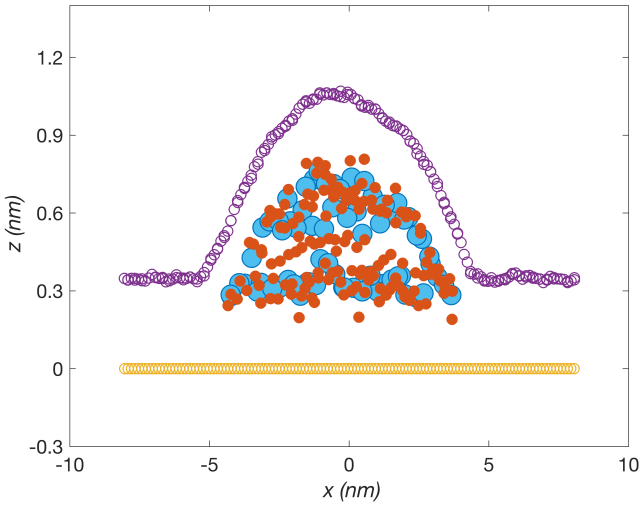

Figure 5.6: Cross-section of the nanobubble profile with top and bottom layers made of graphene. The trapped material consists of water molecules, denoted by large (oxygen) and small (hydrogen) circles.

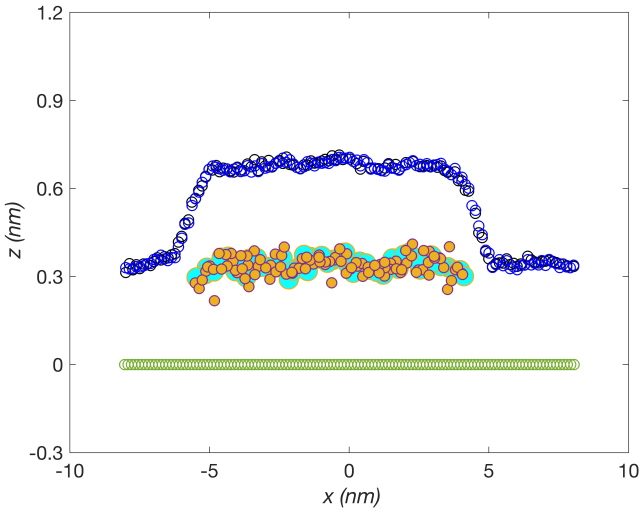

Figure 5.7: Cross-section of the nanobubble profile with the top layer made of hBN and the bottom layer made of graphene. The trapped material consists of water molecules, represented by large circles (oxygen) and small circles (hydrogen).

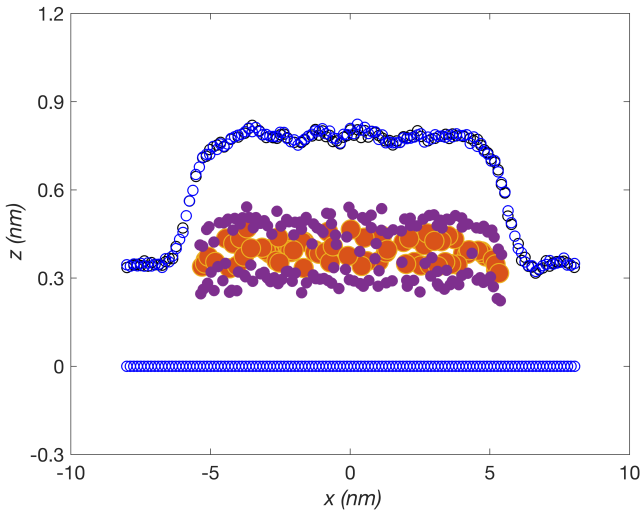

Figure 5.8: Cross-section of the nanobubble profile with top and bottom layers made of hBN. The trapped material consists of decane hydrocarbon molecules, denoted by large (carbon) and small (hydrogen) circles. In the hBN layers, atomic charges are artificially turned off.

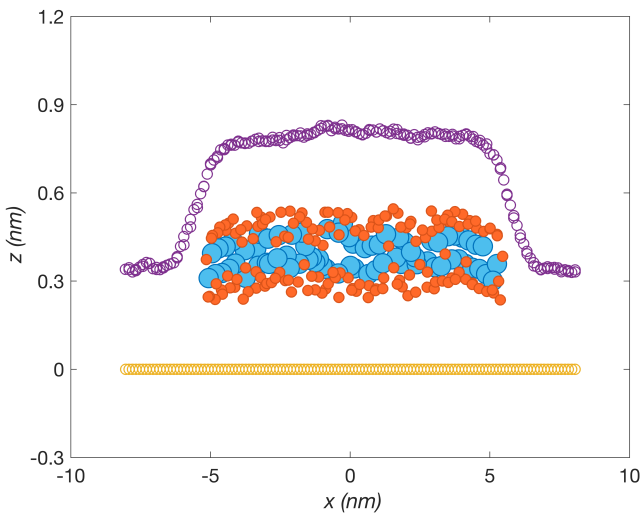

Figure 5.9: Cross-section of the nanobubble profile with top and bottom layers made of graphene. The trapped material consists of decane hydrocarbon molecules, denoted by large (carbon) and small (hydrogen) circles.

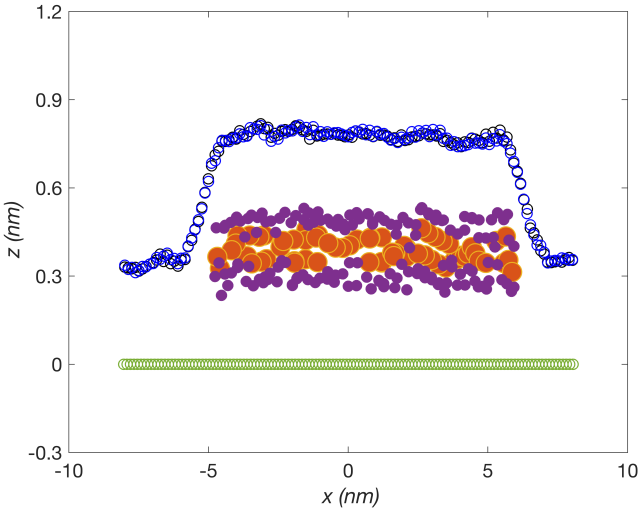

Figure 5.10: Cross-section of the nanobubble profile with the top layer made of hBN and the bottom layer made of graphene. The trapped material consists of decane hydrocarbon molecules, denoted by large (carbon) and small (hydrogen) circles.

bubble containing decane at room temperature is expected to have lower hydrostatic pressure than its water-filled counterpart. This can be attributed to the heavy decane molecules exhibiting less inertia and weaker collisions with the boundary layers, leading to a lower pressure generation compared to water, as per kinetic theory. Consequently, bubbles containing decane have a reduced tendency to overcome the elastic response of the bubble layer and gain height compared to bubbles containing water.

5.3.4 Annealing Simulations

Considering the relevance of baking procedures in pertinent experiments, we explored the effects of increasing the temperature, starting with bubbles filled with water. At an elevated temperature of 170 °C, we simulated a bubble with both top and bottom layers consisting of hBN sheets containing 1000 water molecules (see Fig. 5.11). Intriguingly, the previously flat profile transformed into a spherical bubble (compare Figures 5.4 and 5.11). With the rise in water temperature inside the bubble, the associated increase in hydrostatic pressure overcame the influence of hydrogen bonds, resulting in a taller bubble [59]. The aspect ratio of the bubble (radius to height) is 0.17. Subsequently, we gradually decreased the temperature back to room temperature. Surprisingly, the bubbles maintained their spherical shape, and this profile closely resembled that observed at 170 °C (not shown here).

In the subsequent phase, we conducted simulations for bubbles containing 1000 water molecules placed between two graphene sheets (see Fig. 5.12) and between a top hBN sheet and a bottom graphene sheet (see Fig. 5.13). In both scenarios, as anticipated, the bubbles exhibited a spherical shape at 170 °C. Upon gradually cooling the bubbles back to room temperature, the spherical profile persisted (not shown here). Notably, all of

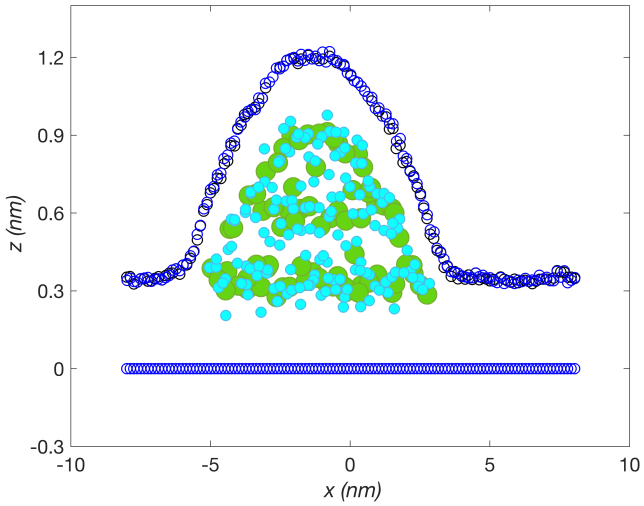

Figure 5.11: Cross-section of the nanobubble profile with top and bottom layers made of hBN. The trapped material consists of water molecules, denoted by large (oxygen) and small (hydrogen) circles. The temperature has been raised to 170 °C.

these bubbles maintained a consistent height of around 0.9 nm.

Subsequently, we investigated hydrocarbon-filled bubbles at an elevated temperature. Specifically, we increased the temperature of the bubble containing 150 decane molecules between hBN layers to 170 °C. Intriguingly, we observed different bubble shapes depending on the rate of heating. For instance, using a Nose-Hoover thermostat damping factor of 0.2 ps (200 times the MD time-step), a flat bubble akin to room temperature (see Fig. 5.3) was maintained (see Fig. 5.14). However, with a faster heating rate of 0.1 ps damping factor, the bubble profile doubled in height, forming two layers of hydrocarbon molecules (see Fig. 5.15). This latter bubble had a height of 0.89 nm, and even after cooling it back to room temperature, the same two-layer configuration persisted. It is noteworthy that in Fig. 5.15, the bubble's profile is not smoothly spherical; rather, it exhibits a distinct two-layer structure with flat edges on both layers.

In our exploration, we delved into the effects of even faster heating on the hydrocarbon-filled bubble. For this, we repeated the simulation with a thermostat damping factor reduced to 0.05 ps. Interestingly, the resulting profile once again exhibited a flat, one-layer configuration similar to that observed in Fig. 5.14. This underscores the highly chaotic nature of the system, where nonlinear responses are expected.

Our overarching conclusion is that the system's behavior is sensitive to the heating conditions, leading to both single-layer and two-layer hBN bubbles containing hydrocarbon molecules after the baking process. The intricate interplay of non-bonded attractions between sheets, hydrostatic pressure exerted by trapped materials, the elastic response of bubble layers, and hydrogen bonding between hydrogen atoms of hydrocarbon molecules and nitride acceptors of the hBN sheets is highly sensitive to initial conditions, determining whether a single or two-layer configuration of the hBN bubble is realized.

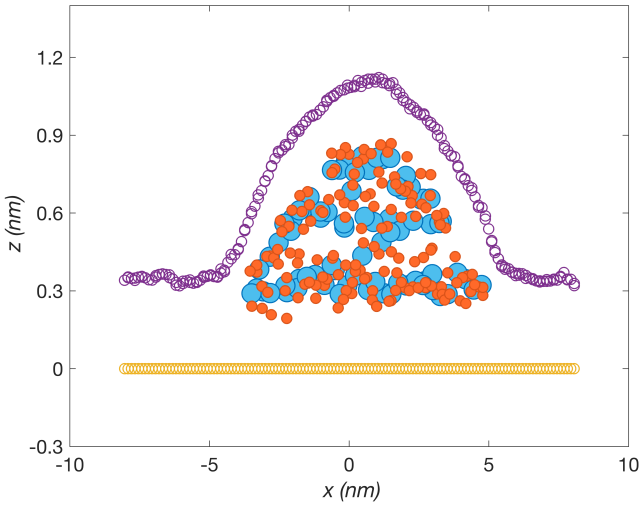

Figure 5.12: Cross-section of the nanobubble profile with top and bottom layers made of graphene. The trapped material consists of water molecules, denoted by large (oxygen) and small (hydrogen) circles. The temperature has been raised to 170 °C.

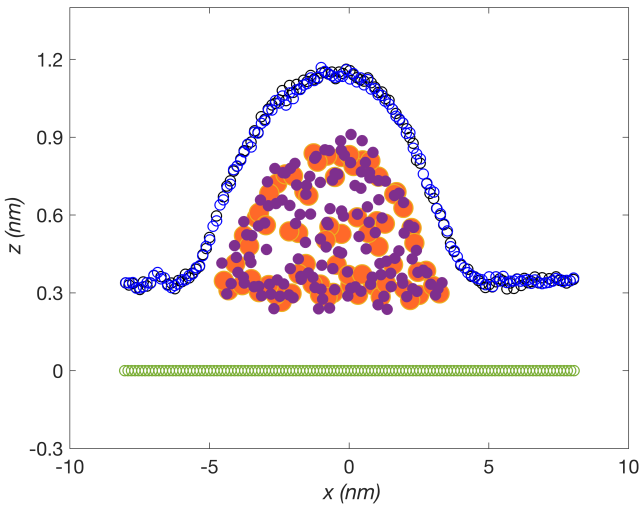

Figure 5.13: Cross-section of the nanobubble profile with the top layer made of hBN and the bottom layer made of graphene. The trapped material consists of water molecules, denoted by large (oxygen) and small (hydrogen) circles. The temperature has been raised to 170 °C.

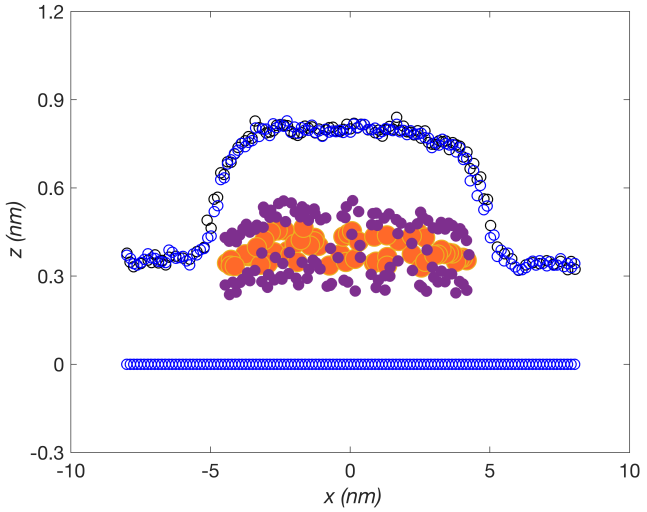

Figure 5.14: Cross-section of the nanobubble profile with top and bottom layers made of hBN. The trapped material consists of decane hydrocarbon molecules, denoted by large (carbon) and small (hydrogen) circles. The temperature has been raised to 170 °C with a thermostat damping factor of 0.2 ps.

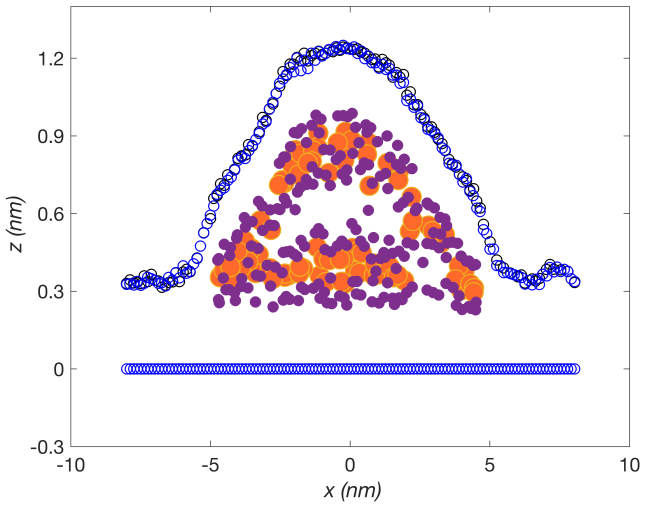

Figure 5.15: Cross-section of the nanobubble profile with top and bottom layers made of hBN. The trapped material consists of decane hydrocarbon molecules, denoted by large (carbon) and small (hydrogen) circles. The temperature has been raised to 170 °C with a thermostat damping factor of 0.1 ps.

In our final exploration, we sought to understand if substituting smaller hydrocarbon molecules would yield different results. Therefore, we conducted a comprehensive set of simulations, repeating all the aforementioned scenarios but replacing the 150 decane molecules with 240 hexane (C_6H_{14}) molecules—maintaining an equivalent total number of atoms. Remarkably, the results for hexane molecules were nearly identical to those observed for decane molecules.

5.4 Conclusion

The prevalence of hydrogen bonding imparts a greater tendency for hBN bubbles to maximize the interface with trapped materials compared to graphene nanobubbles. The kinetic movements and higher hydrostatic pressure of water-filled bubbles make them more prone to deviate from a single-layer conformation compared to hydrocarbon-filled bubbles. Notably, when water is present, baked bubbles exhibit a consistent spherical shape. In contrast, the presence of hydrocarbons introduces a chaotic element, and depending on the rate of heating, both single-layer and two-layer configurations have been observed, underscoring the nonlinear and sensitive nature of the system.

Chapter 6

Cation controlled permeation of charged polymers through nano-capillaries[¶]

Molecular dynamics simulations are used to study the effects of different cations on the permeation of charged polymers through flat capillaries with heights below 2 nm. Interestingly, we found that, despite being monovalent, Li^+, Na^+, and K^+ cations have different effects on polymer permeation, which consequently affects their transmission speed throughout those capillaries. We attribute this phenomenon to the interplay of the cations hydration free energies and the hydrodynamic drag in front of the polymer when it enters the capillary. Different alkali cations exhibit different surface versus bulk preferences in small clusters of water under the influence of an external electric field. This study presents a tool to control the speed of charged polymers in confined spaces using cations.

6.1 Introduction

Charged polymers are prevalent in nature and industry. They can be produced when polyelectrolytes dissociate. Polyelectrolytes have ionizable functional groups. Upon dissolution of polyelectrolytes in water, the ionizable groups will dissociate, and while dispersing counter-ions in the water, polyelectrolytes will turn into charged polymers. DNA and most proteins are examples of these macromolecules [159]. The highly solvable characteristics of charged polymers make them beneficial to a wide range of industrial applications, including drug delivery [12–14], nano reactors [15, 16], and cell biology [17, 18].

Experiments have revealed entropically driven movement of polyelectrolytes when they tend to become unstructured which motivates the study of charged polymers inside confinement [160]. Furthermore, through the translocation inside nanoscale spaces, charged polymers can be detected, processed, and sequenced [22, 61–63]. Nanocapillaries at molecular scales have been made possible due to recent advances in fluidics fabrication [1–11]. The slit pores of few molecular diameters provide enhanced control over confinement [60]. Due to this, they have attracted a lot of attention. In highly confined capillaries,

[¶]This chapter contributed to the paper: Cation-controlled permeation of charged polymers through nanocapillaries. Physical Review E **107**, 034501 (2023).

how the polymer attempts to permeate the capillary might have just as much influence on its transmission as the behavior of the polymer inside the capillary itself. Earlier studies conducted on macromolecules' translocation where mostly limited to spaces of the order of 10 nm and beyond [161–163]. Here we investigate a very different regime with polymer transmission in narrow capillaries below 2 nm.

Conventional theories such as the de Gennes regime [164], the Odijk regime [165], Manning [166] and Poisson−Boltzmann [167] might not be applicable in strong confinements, and furthermore they do not consider the details of ionic interaction and the specifity of counterions. Molecular simulations do not have those restrictions. We used molecular dynamics (MD) simulation to investigate how different cations of Li^+, Na^+, and K^+ influence the permeation of a charged polymer through a capillary with a 1.8-nm height. Since C and H atoms are ubiquitous constituents of charged polymers, we used a hydrocarbon molecule ($C_{10}H_{22}$) with artificial electrical charge on its atoms as a representative of a charged polymer. This particular polymer molecule was chosen in order to have a characteristic size comparable and smaller than the capillary size so that it will not feel an entropic barrier when it is permeating through the capillary. Interestingly, we found that the aforementioned cations, although being monovalent, had different influences on the polymer permeation. This, in turn, affected the dynamics of the polymer when transmitted inside the capillary. Our study shows that the permeation and transmission speeds of charged polymers in confined capillaries can be modulated by varying the type of cation.

6.2 Simulation details

The simulation system is schematically shown in Fig. 6.1. The system consists of two reservoirs connected by a narrow capillary made of two graphene sheets. The reservoirs are filled with water with a bulk density of 1000 kg/m^3. KCl, LiCl and NaCl are used as electrolytes which are dispersed inside the reservoirs. The polymer initially was put in the corner of the feed (left) reservoir. The reservoirs' dimensions are 5.3 nm × 5.3 nm × 5.0 nm assuring enough space to accommodate ample ions up to 1M concentration. The capillary length is 6.3 nm having a height of 1.8 nm. Periodic boundary condition is applied along the z direction.

Each polymer atom was given an artificial electric charge of -0.5e. The system atoms feel an applied body force proportional to their charge, which is similar as in the case of a uniform electrical field. When the polymer is exposed to the electric field, it starts permeating through the capillary. The direction of the electrical field was set such that it pulls the negatively charged polymer into the capillary and the permeate (right) reservoir.

The simulations were carried out using the LAMMPS package [123]. The water molecules were modeled using the SPC/E model. The ions were considered point-charged particles. Van der Waals interactions were modeled using the Lennard-Jones (LJ) potential, and the OPLS [155] force field was used to describe the bond, angle, and dihedral potentials of the hydrocarbon molecule. Table 1 summarizes the LJ coefficients, while for cross parameters Lorentz-Bertholet mixing rules were applied. Van der Waals interactions were cut off at 9.8 Å, and the long-range electrostatic interactions were calculated by utilizing the particle-particle particle-mesh (pppm) algorithm in k-space [158]. To accel-

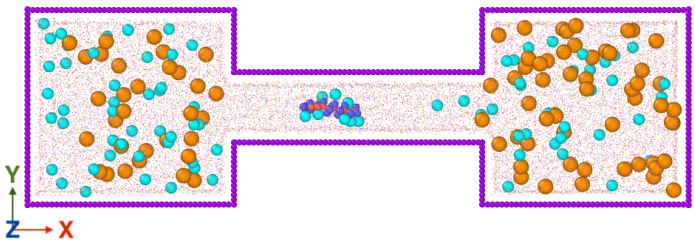

Figure 6.1: Schematic of the simulation setup. The feed and permeate reservoirs are connected by a narrow flat capillary. External electrical field is applied on the charged particles pulling a negatively charged polymer from the feed reservoir into the capillary and subsequently it diffuses into the permeate reservoir. Cyan and orange particles represent cations (K^+, Na^+, Li^+) and anions (Cl^-), respectively. For ease of illustration, water molecules are depicted as tiny points.

erate the simulations, bonds and angles constraints were applied to the water molecules according to the Shake algorithm [168, 169]. The Newtonian equations of motion were discretized by using the velocity-vervet algorithm with a time-step of 0.5 fs. Using Nose-Hoover's thermostat (with 20 fs damping parameter), time integrations were performed in canonical ensemble (NVT) at room temperature. The initial coordinates of the particles were generated using the VMD [170] and Packmol [171] packages. The schematic of the simulation system (Fig. 6.1) was produced using the Ovito software [133].

The bulk versus surface solvation of a cation (K^+ or Li^+) within a spherical cluster of water composed of 186 molecules was investigated using steered molecular dynamics (SMD). Free energy is calculated as described in ref. 172 and ref. 67. The cation is bonded to a simple harmonic spring with a constant of 49 kcal/mol.Å. The spring equilibrium distance from the center of mass of the cluster was gradually increased in intervals of 1 Å so that the cation gradually moved from the center to the surface. In each interval, the system is initially relaxed for 50 ps, and then an NVT simulation is performed for 5 ns at room temperature, and the average force felt by the spring is calculated. The free energy can be calculated by numerically integrating the force versus the distance.

The simulations were repeated using two models, one non-polarisable and one polarisable. For the non-polarisable model, a simple point charge model is used for water (SPC/E) and cations (similar to that used for the main results), together with LJ and Coulomb forces. The polarisable model is based on the ReaxFF parameterised for electrolyte solutions together with the standard Qeq charge distribution. The cut-off radius for SMD simulations is taken large i.e. 10 nm. To avoid evaporation of water molecules from the surface of the cluster, an illusory spherical wall with a radius of 1.4 nm was considered around the cluster, interacting only with water molecules according to the LJ formula (with oxygen parameters). However, the energy contributions from the interaction with the wall are not included in the calculation of energy. The other simulation details are similar to those for the main MD simulations.

Table 6.1: Parameters for the interaction potentials

Atom type	σ_i (Å)	ϵ_i (kcal/mol) $\times 10^3$	Ref.
C (decane)	3.50	65	155
H (decane)	2.49	30	155
O (water)	3.12	169	173
H (water)	0	0	174
C (graphene)	3.41	55	120
K	3.31	99	175
Na	2.58	99	175
Li	1.51	166	175
Cl	4.40	99	175

6.3 Results and discussion

Figs. 6.2(a-d) show the time-displacement curves of the polymer center of mass for four different applied electrical fields, which are equivalent to applying voltages of, respectively, 5V, 12V, 25V, and 50V across the entire system. For each case, calculations were performed with five different KCl concentrations. Note that the polymer encounters a barrier when trying to permeate through the capillary. For instance, for the lowest voltage (5V) we observe that for all KCl concentrations, the polymer moves towards the capillary mouth but is not able to enter the capillary. In the following, we will examine the origins of such an entry barrier. For larger voltages, the KCl concentration within the reservoirs influences the polymer transmission considerably: the smaller the KCl concentration, the larger the polymer entry probability, and the faster the polymer transmission.

The probability of permeation and transmission speed are higher for larger voltages, as one would expect (see Fig. 6.2). However, it is intriguing that polymer transmission speed correlates inversely with reservoir ion concentration. This is similar to what occurs in DNA translocation through nanopores with heights of about 10 nm [64]. Therefore, we may hypothesize that the counter-cations (K^+ here) which have settled on the polymer surface reduced its effective charge and in doing so reduces the effective force acting on the polymer.

In order to explore further, additional simulations were performed using LiCl and NaCl electrolytes as well. The time-displacement curves of Li^+ and Na^+ as cations are depicted in Figs. 6.3 and 6.4, respectively. Li^+ and Na^+ cases also exhibit suppression of transmission at higher concentrations, although the curves for different cations are not the same. Note that similar result were observed earlier in DNA experiments, showing that although potassium, lithium, and sodium are all monovalent cations, their impact on transmission is different [64].

Fig. 6.5 illustrates the polymer transmission mean velocities for different electrolytes and concentrations at 25V and 50V. The mean velocity of polymer was found by fitting a line to the time-displacement curves when polymer is inside the capillary. Interestingly, different cations result in different polymer transmission velocities with the largest for lithium and the smallest for potassium. The trend is in contrast to the observation of

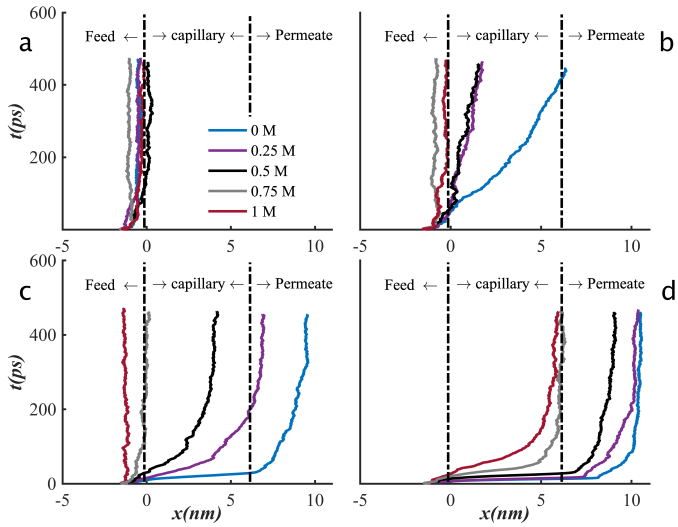

Figure 6.2: Time evolution of the polymer center of mass for five different KCl ion concentrations subjected to different voltages across the system: 5V(a), 12V(b), 25V(c) and 50V (d).

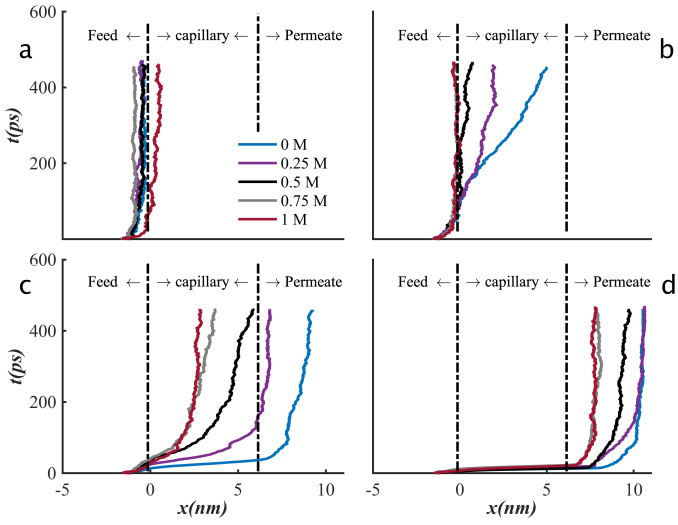

Figure 6.3: Time-displacement curves for the polymer centre of mass for five different LiCl ion concentrations subjected to different voltages across the system: 5V(a), 12V(b), 25V(c) and 50V (d).

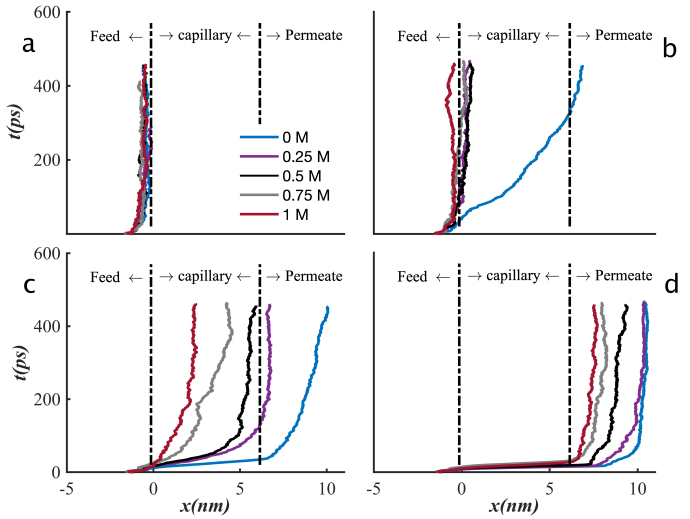

Figure 6.4: Time-displacement curves for the polymer centre of mass for five different NaCl ion concentrations subjected to different voltages across the system: 5V(a), 12V(b), 25V(c) and 50V (d).

DNA translocation in nano-pores, where translocation was slowed when potassium ions were replaced by lithium [64].

To investigate further, we examined the time-displacement curves for three different cases including systems without solute ions, systems with ions, and systems with ions fixed at certain positions (generated initially at random), thus, not able to move. The latter case was investigated to determine whether ions' influence was solely due to their attachment to the polymer surface, or if they would also produce an electrophoretic barrier. Fig. 6.6 shows the time-displacement curve for potassium (a-c) and lithium (d-f) for the three mentioned cases. For each cation, the three columns from left to right, are related to ion concentrations of 0.5M, 0.75M and 1M, respectively. Notice that the x-axis is restricted to the capillary length. Clearly, when lithium is present, all three curves are relatively close to each other, whereas for potassium, the curves of the systems with moving ions are separated from the other two.

In both potassium and lithium electrolytes, the fixed ion curves are very close to the curves in the absence of any ions. This is sufficient to conclude that adhesion of the cations to the surface of the polymer and consequently the reduction of its effective charge dominate the polymer dynamics. Nevertheless, the next question is: why is there such a clear difference in potassium and lithium solutions? Is this related to what is happening inside the capillary or does it originate from what is happening prior the polymer enters the capillary?

Fig. 6.7(a) shows the number of cations within the capillary for both potassium and lithium electrolytes at 50V versus time. The start of the time was set to when the polymer started moving. The bold curves are averaged over the last 2.5 ps and are depicted for the time interval when the polymer resided inside the capillary. It is apparent that in potassium electrolyte, the number of cations inside the capillary, and consequently the number

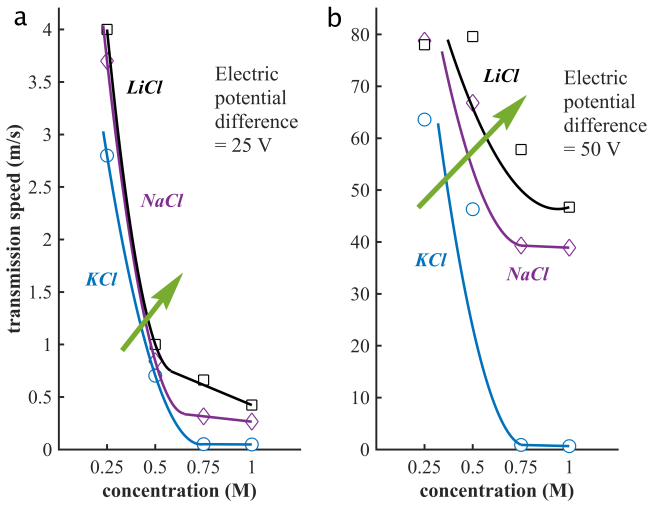

Figure 6.5: Polymer mean velocity inside the capillary versus the cation concentration for KCl, NaCl and LiCl electrolytes at 25V (left) and 50V (right). The curves are guide to the eye.

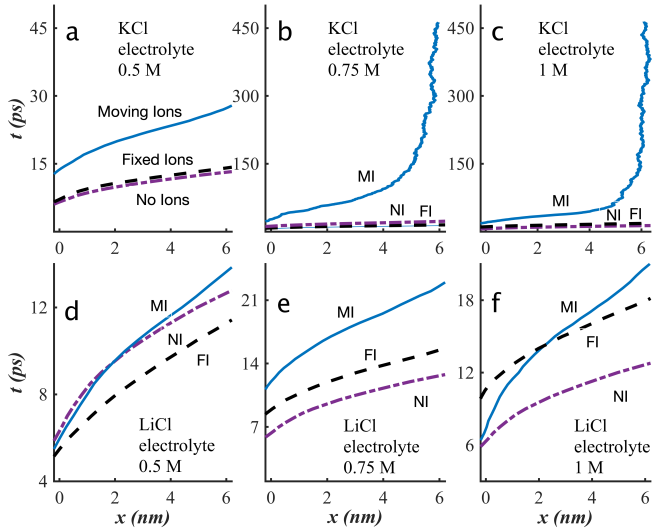

Figure 6.6: Polymer time-displacement curves for three different systems including: without ions, with ions and with ions frozen at particular positions. The upper and lower row, respectively, are for KCl and LiCl electrolytes, and the columns from left to right are for 0.5M, 0.75M and 1M solutes concentrations.

of cations settling on the polymer surface are higher than in lithium electrolyte. Thus, it is understandable why the polymer velocity was lower with potassium electrolytes (see Fig. 6.5). Another important point to note is that the polymer in potassium electrolyte enters the capillary much later than that in lithium electrolyte. Therefore, one can conclude that the main reason for the difference in the systems' behavior is the pre-entering of the polymers into the capillary. Fig. 6.7(b) illustrates the time-displacement curves of the same two cases as Fig. 6.7(a), emphasising the capillary mouth. The polymer enters the capillary quite smoothly in lithium electrolyte, whereas in potassium electrolyte, the polymer experiences a barrier before entering the capillary.

To describe these effects, we hypothesize that the aforementioned barrier is present in both potassium and lithium electrolytes; however, in potassium electrolyte, from the beginning of the polymer movement until it reaches the capillary mouth, a higher number of cations have settled on its surface than in lithium electrolyte. According to our MD trajectories, at the capillary mouth, five K^+ ions stick to the polymer in case of potassium electrolyte, while three Li^+ ions stick to it for lithium electrolyte. Therefore, the polymer in potassium electrolyte has a lower effective charge, so the applied electrical force is less to overcome the barrier. It is for this reason that the polymer enters the capillary noticeably later in the presence of the potassium electrolyte. This delay at the capillary mouth, in turn, causes even more cations to settle on the surface of the polymer, and eventually, the polymer enters the capillary with a higher number of cations and a lower velocity. The reason why a higher number of K^+ ions stick to the polymer before it enters the capillary than Li^+ ions can be attributed to the higher hydration strength of the lithium ions (hydration enthalpy of -520 kJ/mol for lithium as opposed to -322 kJ/mol for potassium [176]). If the ions are to settle on the polymer surface, they need to be dehydrated (at least partially), which is more likely for potassium ions.

In order to examine this hypothesis, we repeated the simulations for two different capillary heights of 1.4 nm and 2.4 nm where we expect higher and lower entrance barriers, respectively. Fig. 6.7(c) depicts the number of cations for the 1.4 nm capillary. For both electrolytes, the number of cations inside the capillary is about the same, and the polymer enters the capillary almost simultaneously. Fig. 6.7(d) illustrates the time-displacement curves of the 1.4 nm capillary emphasising the capillary mouth. Contrary to the 1.8 nm capillary, here, the barrier is also pronounced for the lithium electrolyte. Due to the narrower capillary, the barrier will be even larger causing the polymer in lithium electrolyte also to be held up at the capillary mouth for some time, and eventually its dynamics will be close to the case of potassium electrolyte. Our MD trajectories show that at the capillary mouth, six cations stick to the polymer for both electrolytes.

Fig. 6.7(e) and 6.7(f) illustrate the number of cations inside the capillary and the time-displacement curves emphasising the capillary mouth for the 2.4 nm capillary, respectively. The capillary is wider this time, and the barrier is not pronounced for any of the systems (see Fig. 6.7(f)). This is the reason why in Fig. 6.7(e) the polymer enters the capillary almost simultaneously for both electrolytes. Despite this, Fig. 6.7(e) shows that a larger number of Li^+ ions are present in the capillary. The MD trajectories indicate that those are dispersed ions that enter the capillary due to the capillary's large height (we did not detect them in 1.4 nm and 1.8 nm capillaries). At the capillary mouth, three cations stick to the polymer for both electrolytes. There is still a possibility that some of the dispersed ions inside the capillary may stick to the polymer. The number of such cations is higher in potassium electrolytes, again due to its lower hydration energy. This

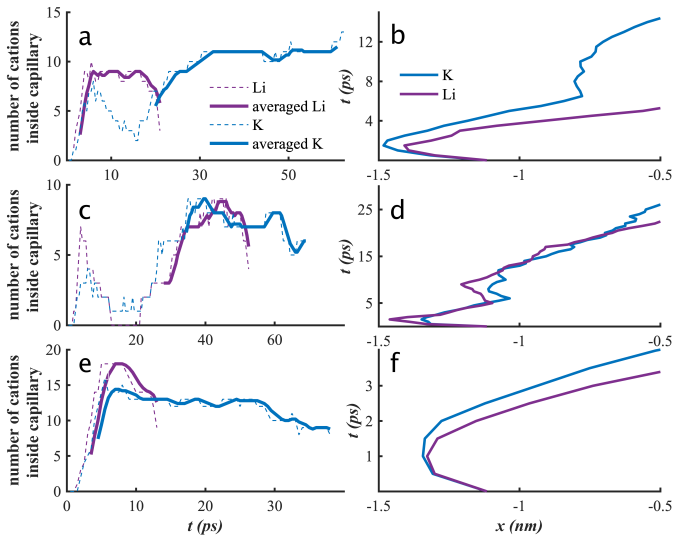

Figure 6.7: (a) Number of cations inside the capillary of height 1.8 nm for potassium and lithium electrolytes versus time. The curves at the time intervals in which the polymer resides inside the capillary are bolded. (b) Time-displacement curves. The capillary gave a bias to lithium electrolyte in a way that the polymer in potassium electrolyte felt a barrier when entering the capillary. Panels (c, d) and (e, f) are the same quantities as (a, b), respectively, for capillaries of height 1.4 nm and 2.4 nm. In the 1.4 nm capillary the polymer felt a barrier in both cases while for the 2.4 nm capillary there is no entrance barrier.

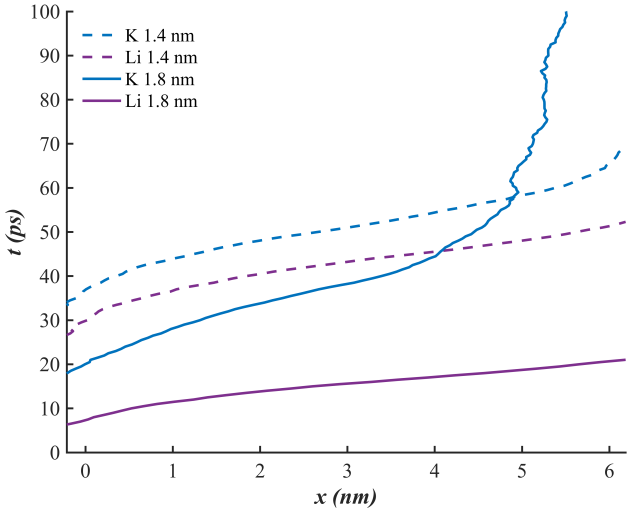

Figure 6.8: Time-displacement curves inside the capillary region for potassium and lithium electrolytes in the capillary of height 1.4 nm. The corresponding curves for the capillary height of 1.8 nm are also shown for comparison.

is why the polymer stays in the capillary much longer for potassium electrolyte than for lithium electrolyte (see Fig. 6.7(e)).

Figs. 6.8 and 6.9 illustrate the time-displacement curves of the polymer for the 1.4 nm and 2.4 nm capillaries. For both figures the corresponding profiles of the 1.8 nm capillary are also shown for comparison. For the 1.8 nm capillary, where the capillary mouth barrier gave a bias to one of the cation types, the curves are diverging, while the curves for the 1.4 nm and 2.4 nm capillaries are rather close to each other.

Using the interplay of ions' hydration energies and capillary mouth barriers, one could design a system for controlling polymer velocity. Unlike the standard capillary effect, where the fluid diffuses into the capillary due to adhesion, the polymer here had to cross a barrier in order to enter the capillary. The capillary mouth barrier is attributed to hydrodynamic drag caused by the water inside the capillary. Indeed, when we modeled the same system without water molecules, the polymer was in a vacuum inside the geometries and moved unimpeded towards the right reservoir. Considering the very short characteristic length of the capillary, the dynamics of water inside the capillary can readily be classified as the standard creeping flow regime (*Reynolds number* $<< 1$). The drag force on the moving object can then be approximated by the Stokes relation ($F = 6\pi r\mu v$), where r and v refer to the radius and velocity of the object, respectively, and μ is the fluid's dynamic viscosity. Deviation from the perfect sphere geometry can be compensated using correction coefficients. Thus, we are able to identify the direct effect of the viscosity of water on the drag force felt by the polymer. Water within highly confined capillaries has been shown to exhibit solid-like properties with a three-fold increase in viscosity compared to bulk water [177, 178]. Therefore, it is expected for the polymer to encounter a noticeable barrier when permeating through the capillary. At this point, we are able to explain the contradiction between our results and the DNA

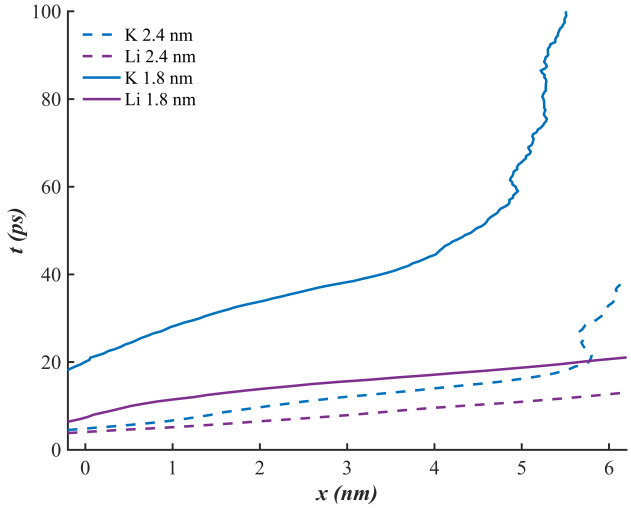

Figure 6.9: Time-displacement curves inside the capillary region for potassium and lithium electrolytes in the capillary of height 2.4 nm. The corresponding curves for the capillary height of 1.8 nm are also shown for comparison.

experiment [64] concerning the trend for cations' influences. In the DNA experiment, the molecule does not experience a significantly enhanced hydrodynamic drag at the pore opening as compared when inside the reservoir. Furthermore, given the experiment's timescale (milliseconds), the cations had ample time to bond with the DNA, so they could simply be regulated based on their interaction strength, which is considerably larger for lithium than potassium (See Table 1 in the Methods section below).

At this stage, we believe we should pay particular attention to the solvation of the cations. The hydration enthalpies discussed above are in fact the results of experiments involving the dehydration of ions in infinite amounts of water. In the present study, the cations are surrounded by small clusters of water. Therefore, results obtained with infinite solvents may not be valid. Additionally, in infinite solvent experiments or continuum theories of dielectrics, the free energy of dehydration is largely assumed to come from enthalpic contributions, and entropy is virtually always ignored [179–181]. In dielectric theory, Born's model estimates that entropy contributes only about 0.5 percent of the enthalpy contribution [182, 183]. However, in studying ions interface solvation in small clusters of water, the entropic contribution is indeed found to be of the same order of magnitude as the enthalpy contribution [66]. It has even been proposed that the bulk hydration of small halides like F^- is driven by entropy [67].

Moreover, the water model used here is a simple charge model (see Methods section) that cannot accommodate induced polarisations, while an accurate study of ionic solvations requires polarisation capabilities for both water and ions. For our purpose, which is to compare the hydration energies of K^+ and Li^+ cations, one appropriate approach would be to examine the surface versus bulk preferences of the cations in a cluster of water under conditions similar to our problem. Surface solvation analysis is useful in that it could reveal how cations prefer to sit at the interface of water and polymer [66].

In the past, interface solvation has been extensively studied, but its conclusions have changed substantially over time. A large dipole moment was initially recognised as critical [68]. Later, it was determined that induced polarisation, coupled with the size and sign of ions, was the major cause of surface solvation [66]. Eventually, the absence of a single explanation for the solvation of various ions was identified [67]. Nevertheless, what is commonly concluded in the literature for alkali cations is that they all favour bulk solvation [69, 180], and their hydration is entirely determined by enthalpy with a negligible contribution from entropy [67]. As a result, we may draw two conclusions. First, the energetics analysis is sufficient to compare the dehydration of potassium and lithium in our problem. Secondly, our simple charge water model (see Methods section) is adequate for this energetic purpose. If the problem was related to large halide ions, which are believed to favour surface solvation, a simple charge water model might result in qualitative and quantitative inaccuracies [66].

Despite these, we cannot still conclude that our model is completely reliable. In our problem, there is a strong external electrical field (3 V/nm equivalent to 50 V for the problem geometry). This strong field, although not yet large enough to make the water conductive, would profoundly alter the solvation and screening properties; even making differences specific to different ions. As far as we are aware, interface solvation has not been fully investigated in the literature in the presence of an external electric field. Therefore, we conducted a steered molecular dynamics (SMD) investigation for the solvation of K^+ and Li^+ cations within a spherical cluster of water (with 1.1 nm radius) containing 186 water molecules, the same order of magnitude as the ratio of the amount of water to the amount of cations found in our reservoirs (See Methods section for details about the simulations). Simulations were conducted for two different situations, without an electric field and with an electric field of 3 V/nm. Each case is repeated for two water models: the non-polarisable simple charge SPC/E model [184] (similar to our other simulations), and the ReaxFF model [185, 186] which is capable of polarising both water and cations.

The results are shown in Fig. 6.10. The figures display the free energy (potential of mean force) and potential energy of the system as function of the distance between the cation and the cluster's center of mass. During SMD simulations, a canonical ensemble (NVT) has been sampled, which indicates that the Helmholtz free energy represents the thermodynamics potential. Details of calculating the free energy are described in the Methods section. The potential energy is determined by summing the van der Waals, electrostatic, and polarisation energies of all species. By neglecting the changes in the system's kinetic energy, the potential energy represents the system's total energy. By subtracting the curves, we can calculate the entropic contribution $TdS(r) = dU(r) - dF(r)$. As water molecules are electrically neutral, the external electric field will not impose any pressure gradients within the system. Additionally, the simulations are performed at a constant temperature. Therefore, we assume that discussing the problem within the framework of equilibrium thermodynamics is relevant.

In the absence of an electric field, as expected, both K^+ and Li^+ cations favour bulk solvation as predicted by both polarisable and non-polarisable models. Additionally, the free energy and energy curves are close to each other, suggesting a subtle role for entropy, as expected. Furthermore, Li^+ has a higher solvation energy than K^+ when the cations are moving away from the cluster. Continuing the free curves to larger radiuses (for example, $r > 2.5$ nm), the curves would approach plateau horizontal behaviour, which

would express the total free energy of desolvation, which is larger for Li^+ than for K^+. More importantly, for either the absence or the presence of electric field, the results of the polarisable and non-polarisable models are quite similar. Therefore, we expect that our simple charge SPC/E model has been reliable for this study.

An interesting observation from the curves when an electric field is present is that potassium favours surface solvation while lithium does not. In turn, this strengthens our hypothesis that K^+ cations are more readily dehydrated than Li^+ cations and settle on the surface of the polymer. As a result, K^+ cations are more easily dehydrated than Li^+ cations, not only due to their lower hydration energy, but also because of a weakening and partial un-occupation of the hydration shells, which occurs for potassium, but not for lithium, due to strong electric fields [187]. These results indicate that alkali cations exhibit different surface versus bulk preferences when an electric field is present, depending on their interactions with the solvent species. It is similar to the behaviour of cations in dimethyl sulfoxide (DMSO) solvent [188], in which the hydration of larger alkalis, which bond less strongly to the solvent, weakens more than the hydration of small ions when present in strong electric fields (same order of magnitude as in our study).

Potassium's surface solvation has occurred in such a manner that its energy curve still continues to increase monotonously. This indicates that it is entropy that has brought the cation to the surface. Since both polarisable and non-polarisable models exhibit the same behaviour, this suggests that surface solvation does not result from polarisation (as has been established for large halides [66, 67]), but rather from the alignment of the dipoles of the water molecules in the direction of the electric field and the perturbation of the hydrogen bond network [187]. When all dipoles are parallel, the entropy of the system is minimal (similar to the concept of freezing in dielectrics [66]). When the K^+ cation is located close to the center of the cluster, its dipole will also orient itself according to the dipoles of the water molecules. As the K^+ cation approaches the surface, it feels agile and perturbs its surrounding dipoles and hydrogen bonds, resulting in an increase in entropy. Due to the strong bond between the Li^+ cation and water, its freedom will not increase that much when it comes to the surface, so no substantial increase in entropy is observed.

In addition, we analysed a hypothetical scenario using our simple charge SPC/E model for potassium in the presence of an electric field, changing the partial charges of the water atoms in order to increase the dipole of the molecule from 2.35D (as per the SPC/E model) to 2.6D. The obtained free energies were almost unchanged, indicating that it is not the magnitude of the dipoles but their alignment that drives the K^+ cation to the surface. With a simple comparison of the hydration enthalpies of potassium and lithium, we were able to accurately assess the true trend to build our hypothesis. Nevertheless, calculating the free energy still strengthens the hypothesis. This is analogous to the pure energetics analysis for interface solvation of halides (with a polarisable force field), which, although quantitatively not quite precise, can qualitatively predict surface versus bulk preference [66].

We have employed ReaxFF parameterised for electrolyte solutions (available in the supplementary information of ref. 189) with the standard Qeq charge distribution model [190]. Considering that even the simple charge model has similar predictions as the polarisable model (see Fig. 6.10), the method of charge polarisation should not have a significant impact. In the presence of an external electric field, Qeq may impose an

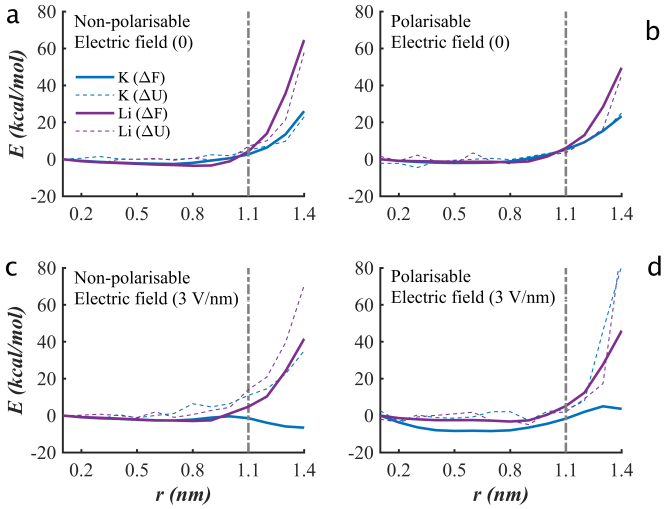

Figure 6.10: Free energy (solid lines) and internal energy (dashed lines) as a function of cation distance from the water cluster center of mass for two cations, K^+ and Li^+. In the upper panels, there is no external electric field, while in the lower panels, there is an external electric field of 3 V/nm. Panels on the left show results for the non-polarisable model, while panels on the right show results for the polarisable model.

unphysical charge distribution due to its global charge transfer across the simulation domain [191]. It has been shown that atom-condensed Kohn-Sham density functional theory (DFT) approximated to second-order (ACKS2) is able to overcome the shortcomings of Qeq [191]. Nevertheless, the unphysical gradient of charge density in a NVT MD simulation with Qeq for a water cluster is several orders of magnitude smaller than that of our problem of attracting cations to the polymer by electrostatic forces [191]. Therefore, we have used the widely used Qeq charge distribution for which ReaxFF has already been examined for electrolyte solutions.

We performed a few additional simulations to investigate whether, in addition to the hydrodynamic drag, there is also an energy barrier in front of the polymer when it enters the capillary. Additionally, we were also able to gain a direct understanding of the changes in hydrodynamic drag, confirming predictions based on an increase in viscosity. This may be more straightforward than calculating the viscosity because, on the one hand, the passage of the polymer inside the capillary causes the problem to be mechanically non-equilibrium, preventing equilibrium calculation of the viscosity. Taking a non-equilibrium approach to the problem, on the other hand, it is unclear whether the liquid with the polymer inside will behave as a Newtonian fluid so that a shear flow can be applied externally and the velocity gradient measured. The polymer was placed into the left reservoir horizontally along the capillary axis. Then, we moved the polymer towards the capillary mouth at a constant velocity of 2 Å/ps, and calculated the horizontal component of the force exerted on the polymer, as well as the potential energy of the system (see Fig. 6.11). At the capillary mouth, the force increases clearly, illustrating the existence of a hydrodynamic drag barrier. As expected, this increase is the largest for the 1.4 nm capillary and the smallest for the 2.4 nm capillary. The potential

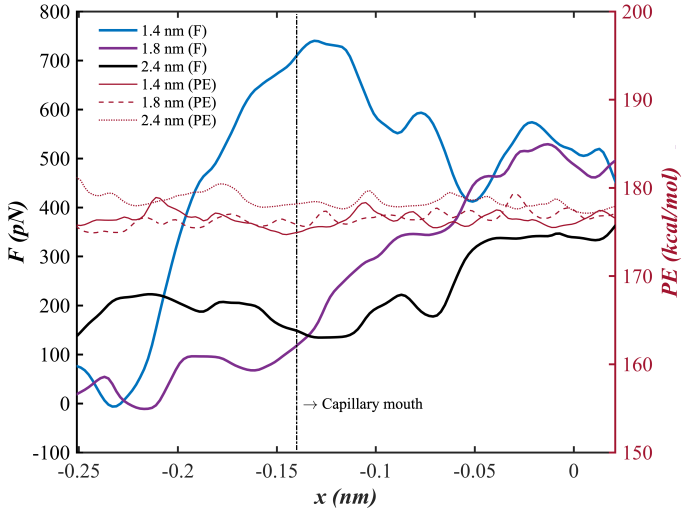

Figure 6.11: Horizontal force applied on the polymer, as well as the system's potential energy when the polymer moves towards the capillary. Force values show an increase at the capillary mouth, whereas potential energy curves maintain almost constant values, suggesting a hydrodynamic barrier in front of the polymer and no energy barrier at the capillary mouth.

energy curves are nevertheless nearly uniform, indicating that there is no energy barrier in front of the polymer as it enters the capillary.

Further, one can compare the free energy ($F = E - TS$) of the polymer inside the reservoir and inside the capillary. The energy curves (Fig. 6.11) represent the enthalpic contribution (E), which is nearly equal for the reservoir and capillary provided that the polymer is horizontal. This is the case for our application, as the polymer was horizontal at the capillary mouth when it attempted to penetrate the capillary. We estimate the polymer's entropy (S) as $k_B lnN$, where k_B is the Boltzmann constant and N is the number of configurations it can adopt [192]. In an in-line configuration, the polymer length is around 14.2 Å (plus 3.4 Å for C-C distances on both sides. See Table 1 in the Methods section below). Furthermore, its gyration radius can be estimated as 4.22 nm, which can be calculated discretely as the root mean square distance of the polymer atoms (weighted by particle mass) with respect to the polymer center of mass ($[\Sigma_{i=1}^{n} m_i r_i^2 / \Sigma_{i=1}^{n} m_i]^{1/2}$, m_i and r_i being the particle mass and the particle distance to the center of mass, respectively). In comparison to the channel height (1.8 nm), it is not inconceivable to envisage as many plausible configurations for the polymer inside the capillary as inside the reservoir. Consequently, the polymer enters the capillary with no free energy barrier, and thus the total contribution is attributed to the hydrodynamic drag.

As a result of the applied electrical field, the entire simulation domain will become polarised. Polarisation decreases the strength of the electrical field, which depends on the amount of added ions and may vary as the polymer moves. It was necessary to examine the capillary's ability to sort out different ions, giving some preference over others, at this stage in order to determine whether the effect of polarisation in the different

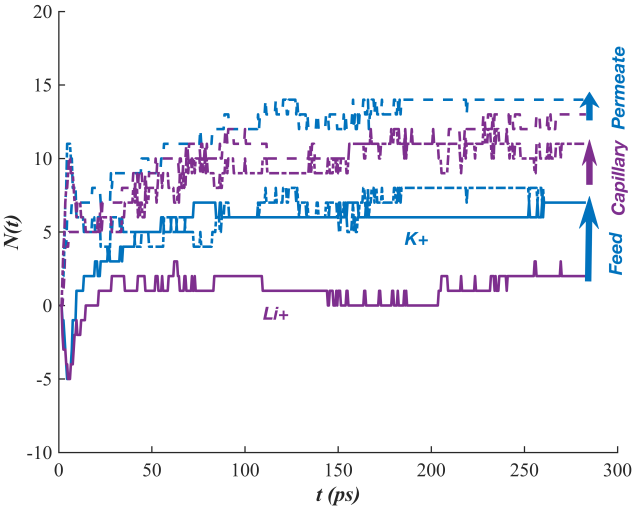

Figure 6.12: The number of cations that penetrate the capillary from the permeate reservoir (dashed lines). K^+ ions are penetrating slightly more. The number of cations remaining inside the capillary (dash-dotted lines). There are slightly more Li^+ ions inside the capillary. They return to the capillary from the feed reservoir, upon reaching a steady state. The number of cations added to the feed reservoir (solid lines). A larger number of K^+ ions in the feed reservoir leads to a partial increase in the potassium electrolyte's polarization voltage.

electrolytes was significant. Hence, we simulated the same system with the 1.8 nm wide capillary without the polymer and at our highest voltage (50 V) and ions concentration (1 M).

While Cl^- anions did not exhibit any noticeable differences in permeation between potassium and lithium electrolytes, K^+ cations tended to penetrate into the capillary from the permeate reservoir slightly more than Li^+ cations (see Fig. 6.12). Additionally, Li^+ ions are slightly more abundant inside the capillary than K^+ ions. This is because once the system has reached a steady state, the Li^+ ions tend to return to the capillary more readily from the feed reservoir than the K^+ ions. Due to these two events, the number of K^+ ions is partly larger in the feed reservoir than Li+ ions (see Fig. 6.12).

We estimated the electric potential induced by polarisation assuming that the ions were located at the center of the reservoirs (see Fig. 6.13). Inset (right side) illustrates the difference between the voltages of the two electrolytes. The induced voltage for potassium electrolyte is partially larger, but the difference between the voltages is around 1.36 V. From the beginning of the polymer's movement until it reaches the capillary mouth, the polarisation voltage is in the range from 4-6 V with a 1.3 V difference (see inset on left), which is the most relevant part of the polymer movement for us.

The same analysis is carried out with the polymer present. With the polymer at the capillary mouth, the difference between the induced voltages of the two electrolytes was 0.6 V larger than without the polymer (similarly with a higher voltage for the potassium electrolyte). This can also be attributed to the tendency of cations to adhere to the polymer

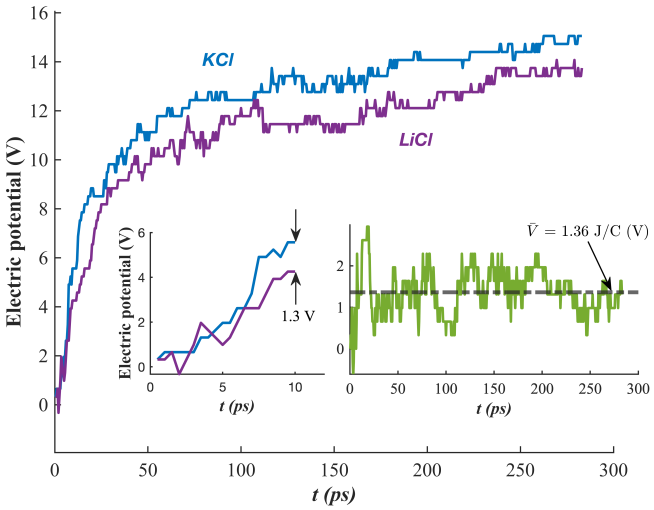

Figure 6.13: Potential difference generated by polarization in KCl and LiCl electrolytes. The inset on the left shows the initial instances until the polymer reaches the capillary mouth. The right inset shows the difference between the induced voltages of the two electrolytes. Compared to the field voltage (50 volts), the induced voltages by the polarization can be neglected.

(with K^+ ions slightly more). Eventually, when compared with the field voltage (50 V), the induced voltages caused by polarisation can be ignored in the interpretation of the main results.

Radial distribution function (RDF) can be used to better understand ionic and polymer solvation, as shown in Fig. 6.14. In the main figure, RDF graphs are shown for potassium-oxygen and lithium-oxygen, each for two cases of inside the reservoir and inside the capillary. There is almost no difference between the two graphs, indicating that the capillary (here 1.8 nm) is not too thin to tear off the hydration shells of the cations. The first minimum for lithium is almost zero for a considerable distance, which implies that its first hydration shell is still present [193]. The coordination number of potassium and lithium (up to the first minimum of the RDFs) is 6.3 and 4, respectively, consistent with the literature [194]. Therefore, our LJ model, in conjunction with electrostatic forces, appropriately models their hydration (see inset at left).

The other three curves shown in the left inset along with their corresponding RDF graphs (right inset) represent the polymer solvation (polymer-O), as well as the distance between the polymer's heavy atom (here C) and the cations (polymer-K and polymer-Li). It is apparent from the location of the first peak in the RDF graphs (right inset) or alternatively from the point at which coordination numbers begin to rise (left inset) that the cations have penetrated well into the polymer's first hydration shell. This also demonstrates the partial dehydration of the cations.

Lastly, we address the water structure near the hydrophobic graphene walls. We calculated the number density of oxygen and hydrogen atoms next to the capillary wall with and without the polymer inside (see Fig. 6.15). The number density of hydrogen in half

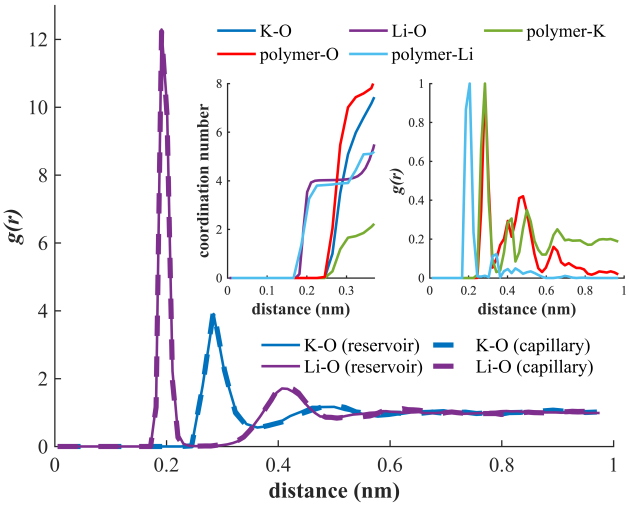

Figure 6.14: Radial distribution functions (RDF) for potassium-oxygen and lithium-oxygen inside the reservoir and inside the capillary. The capillary (1.8 nm) is not too thin to rip off the hydration shells of the cations. Coordination number and RDF graphs for ionic and polymer solvation are shown in the insets.

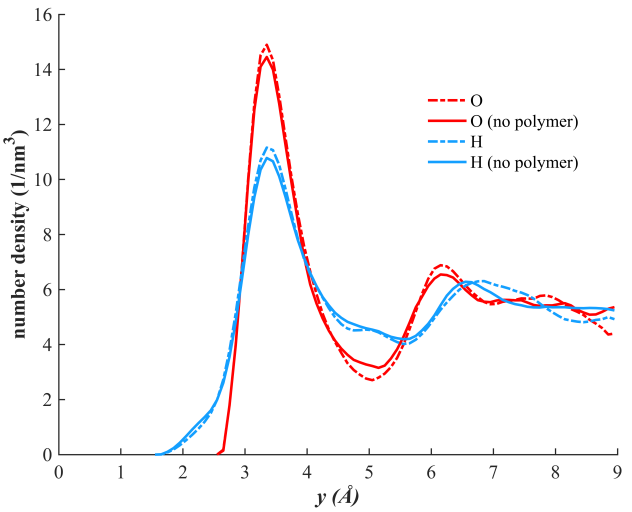

Figure 6.15: The number density of oxygen and hydrogen atoms close to the capillary wall with and without the polymer. Number density of hydrogen is shown in half value. The water molecules next to the capillary wall are evenly populated between dangling OH groups and when two hydrogen atoms are facing the wall.

value is shown in the figure. As the first peak value for hydrogen is almost coincidentally 1.5 times larger than for oxygen, we can deduce that the structure of water molecules near the graphene is almost evenly populated between dangling OH groups and the two hydrogen atoms facing the wall, indicating moderate hydrogen bonds among the water molecules. The graphs indicate that the polymer has little impact on the water structure, although slightly denser water molecules are found close to the wall when the polymer is present.

6.4 Conclusion

We studied the permeation of a charged polymer driven by an external electrical field through a graphene capillary. The polymer encounters a hydrodynamic barrier while going through the capillary. In the presence of cations inside the feed reservoir, some cations adhere to the surface of the polymer. As a result, the polymer's effective charge decreases. This weakens its ability to overcome the barrier and to enter the capillary. Interestingly, the monovalent cations of Li^+, Na^+, and K^+ show a different influence in a way that the polymer entering occurs more likely, and the transmission speed is faster, when lithium electrolyte is present, followed by sodium and then potassium electrolytes. This phenomenon is explained by the different hydration free energies of the cations. Based on their interaction strength with the solvent, different alkali cations exhibit different surface versus bulk preferences in small clusters of water when exposed to a strong external electric field. This study shows that by exploring the interplay between the hydrodynamic barrier resulting from confinement and the electrolyte conditions, one can control the polymer transmission in nm-scale capillaries.

Chapter 7

Capillary condensation of water in graphene nanocapillaries[¶]

Recent experiments have revealed that the macroscopic Kelvin equation remains surprisingly accurate even for nanoscale capillaries. This phenomenon was so far explained by the oscillatory behavior of the solid-liquid interfacial free energy. In this chapter, we demonstrate thermodynamic and capillarity inconsistencies with this explanation. After revising the Kelvin equation, we ascribe its validity at nanoscale confinement to the effect of disjoining pressure. To substantiate our hypothesis, we employed molecular dynamics simulations to evaluate interfacial heat transfer and wetting properties. Our assessments unveil a breakdown in the previously established proportionality between the work of adhesion and the Kapitza conductance at capillary heights below 1.3 nm, where the dominance of the work of adhesion shifts primarily from energy to entropy. Alternatively, the peak density of the initial water layer can effectively serve as a parameter to probe the work of adhesion. Unlike under bulk conditions, high confinement renders the work of adhesion entropically unfavorable.

7.1 Introduction

When a narrow, open-ended capillary tube is immersed in a container of liquid, the liquid rises or falls inside the tube to a level that is different from the position of the liquid surface in the container. This difference in height is determined by equating the weight of the liquid column to the force exerted by the capillary pressure. Capillary pressure is essentially the pressure difference across the interface of the liquid and its vapor above it.

However, what happens if the scale of the experiment is comparable to the molecular distances, i.e., nanoscale? The aforementioned force balance should, in this situation, also take into account the difference in the vapor pressure at the surface of the container and at the surface of the tube. This pressure difference, which varies vertically like the change of atmospheric pressure with altitude, can be neglected for macroscale devices. Thomson (Lord Kelvin) showed in 1870 that the ratio of vapor pressure above the tube

[¶]This chapter contributed to the paper: Capillary Condensation of Water in Graphene Nanocapillaries. Nano Letters **24**, 18, 5625–5630 (2024).

P_r to that above the liquid surface P_∞ can be expressed as $P_r = P_\infty exp(\frac{M_r}{\rho_l R}\frac{1}{T}\frac{2\gamma}{r})$ where M_r is the molecular mass of vapor, ρ_l is the density of the fluid, R is the universal gas constant (8.314 $Jmol^{-1}K^{-1}$), T is temperature, γ is the liquid surface tension and r is the curvature of the liquid surface in the tube. This equation is known as the Kelvin equation [195, 196]. If the capillary system is placed in an environment whose relative humidity exceeds the ratio of vapor pressure given by the Kelvin equation, the vapor above the tube becomes oversaturated, starts to condense, and the tube starts to fill with liquid. This phenomenon is called capillary condensation. It is customary for the Kelvin equation to directly use relative humidity rather than the ratio of vapor pressure (see Equation 1 in ref. 70). Capillary condensation typically occurs under large negative pressure, which makes its study very important for e.g. the design of microelectromechanical systems [71, 197–199].

Recent experiments investigated capillary condensation of water inside extremely narrow capillary tubes of less than 1 nm height, made of graphene and mica [70]. Surprisingly, the Kelvin equation was found to be valid for these thin geometries. The experiments found condensation near the predictions of the Kelvin equation with additional oscillations for capillary heights below 1 nm (see Fig. 7.1). In this chapter, we demonstrate that this observation can be explained by the disjoining pressure

7.2 Evaluating the hypothesis on oscillatory interfacial energies

We start with the hypothesis of ref. 70. According to this hypothesis, the Kelvin equation can be rewritten based on Young's equation ($\gamma_{sv} - \gamma_{sl} = \gamma cos(\theta)$, γ_{sv} and γ_{sl} being the solid-vapor and solid-liquid interfacial free energies, respectively, and θ the contact angle) resulting in $P_r = P_\infty exp[-2M_r(\gamma_{sv} - \gamma_{sl})/hRT\rho_l]$. If it is assumed that γ_{sv} and ρ_l are independent of confinement, then the effect of confinement can only manifest itself in γ_{sl}. The effect of capillary height (h) on γ_{sl} can be expressed as $\Delta\gamma = \gamma_{sl}(h) - \gamma_{sl}(\infty)$, which should approach zero for sufficiently wide capillaries. Therefore, the Kelvin equation should be modified with the term $exp[2M_r\Delta\gamma/hRT\rho_l]$ to account for the effect of confinement.

To compute $\Delta\gamma$ as a function of h, ref. 70 considers a graphene nanochannel submerged in water. Then, the nanochannel is gradually narrowed and the potential energy of the system is computed at each channel height. The changes in the potential energy of the system relative to the width of the channel are interpreted as changes in γ_{sl}. Molecular dynamics (MD) simulations in ref. 70 were performed with rigid graphene sheets. Due to the commensurability effects of water, the system potential energy and consequently the corrected Kelvin equation show fluctuating behavior in small channel heights (see Fig. 2 of ref. 70).

It was suggested that if the elastic flexibility of the graphene sheets is taken into account, the fluctuations will be reduced and the corrected Kelvin equation may agree well with the experimental results [70]. Here, we performed similar MD simulations with both rigid and flexible graphene sheets. It is found that the wall flexibility indeed diminishes the fluctuations in the results, although for very small channel heights, the decrease is

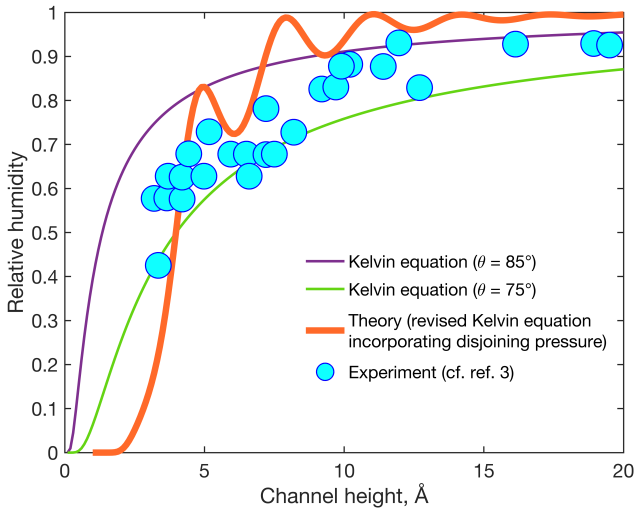

Figure 7.1: The revised Kelvin equation, attributing capillary pressure to disjoining pressure, exhibits excellent agreement with experimental data (cf. ref. 70). The predictions from the original Kelvin equation with water-graphene contact angles of 75° and 85° are also presented. The oscillatory behavior of the structural term in the disjoining pressure, distinct from Laplace pressure, enables the revised equation to accurately capture the oscillations observed in the experimental data. Small disparities in higher channel heights arise from additional terms in the disjoining pressure (beyond van der Waals and structural terms), as well as from the onset of Laplace pressure due to the meniscus formation in the liquid profile as the capillary widens.

small.

We conducted molecular dynamics (MD) simulations to investigate the hypothesis presented in ref. 70. A water pool with dimensions of 92 × 83 × 55 Å was utilized in our simulation. Inside this pool, a graphene nanochannel was embedded, comprising four layers as the top wall and four layers as the bottom wall, each layer measuring 61 × 55 Å (see Fig. 7.2). While the outermost graphene layers remained fixed, the inner six layers were subjected to either fixed positions (solid walls approach, similar to the simulation in ref. 3) or allowed movement (flexible walls approach).

The initial channel height was set at 20 Å and progressively decreased in 0.2 Å intervals. At each channel height, the system underwent an equilibration phase in the canonical ensemble (NVT) using the Nose-Hoover thermostat (with a damping factor of 20 fs) for 1 ns. Subsequently, we computed the potential energy of the system, including that of the water molecules alone, for each channel height. This allowed us to calculate the changes in the potential energy of the system at each height with respect to the potential energy at the initial height (20 Å), represented by ($\Delta\gamma = \gamma_{sl}(h) - \gamma_{sl}(\infty)$). These changes are interpreted as alterations in the solid-liquid interfacial free energy due to varying channel heights.

The outcomes are depicted in Fig. 7.3. The original Kelvin equation is represented by the green solid line. Multiplying the original Kelvin equation by the correction factor—introduced in the main text as $exp[2M_r\Delta\gamma/hRT\rho_l]$—resulted in open blue circles (for the solid walls approach) and filled purple circles (for the flexible walls approach). Notably, the flexible walls alleviate oscillations, although their impact is minor in very small channel heights.

However, a crucial observation is that this type of calculation does not accurately provide us with changes in the interfacial free energy. The inset also displays the changes in potential energy when only the group of water molecules, specifically for the solid walls approach, is considered. The results are nearly identical to when the energy of the entire system is taken into account. Minimal differences emerge only at very small heights when the upper and lower walls reach their MD cut-off, contributing to the total energy. Therefore, this examination is more influenced by changes in the state of the bulk water rather than the interface (whose contribution essentially embodies the interfacial free energy).

Nevertheless, we argue that this method might not estimate γ_{sl} accurately. First, altering the nanochannel height impacts not only the interface but also the state of the bulk water. Consequently, the calculated energy difference might not solely represent the contribution arising from the change of the interface state. When computing the energy difference solely for water molecules, the resulting outcome closely resembles that obtained when calculating the entire system's energy (see the inset of Fig. 7.3). The difference becomes evident only when the upper and lower walls fall within the MD cut-off distance (9.8 Å).

Second, in estimating the free energy, only the potential energy is considered while the entropy contribution is disregarded. Specifically, for the water-graphene interface, the entropy contribution to the work of adhesion ($W_{sl} = \gamma_{sv} + \gamma - \gamma_{sl}$) has been estimated to be approximately one third [200]. However, this value pertains to bulk water. Here, the water is confined, and in the subsequent discussion, we will demonstrate that the

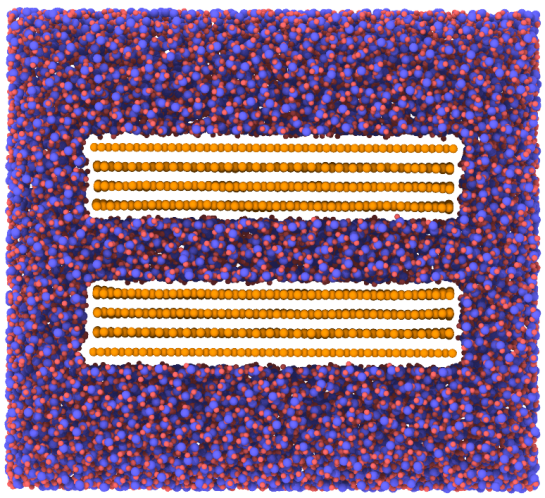

Figure 7.2: Schematic of the molecular dynamics simulation system. The graphene nanochannel thickness is gradually reduced, and the potential energy of the system is calculated at each channel height. Cf. Fig. 7.5 in the main text for color indications.

entropy contribution is comparable to the energy contribution and may even dominate at times.

Third, the validity of Young's equation under high confinement is questionable. In a very narrow capillary, when the capillary contains perhaps as few as only two layers of water, either when the capillary is being filled or when the water profile has settled, the velocity profile of water is not expected to be anything other than the plug flow profile. If then, in equilibrium, the column of water is axially raised by an infinitesimal amount δx, the contribution of the energy change from the interfaces will be $\gamma_{sl}\delta x$ and $-\gamma_{sv}\delta x$. However, the vapor-liquid interface (contribution from γ) has no area change. Therefore, Young's equation cannot be derived. Another conclusion can also be reached here. If the energy of bulk water remains unchanged due to the displacement, equilibrium requires γ_{sl} to approach γ_{sv} (which is nearly negligible), which is implausible. Therefore, the energy of the column of water, which varies with displacement, needs to be significant. This is the film energy $P(h)$. This was expected because for high confinement, there is a considerable repulsive force between the capillary walls, which induces disjoining pressure (derivative of the film energy $\Pi(h) = -dP/dh$).

7.3 Revising the Kelvin Equation

Let us now revisit the Kelvin equation. The term $2\gamma/r$ is essentially the pressure difference across the liquid-vapor interface, according to the Young-Laplace equation. Although the validity of the Young-Laplace equation has been demonstrated at the nanoscale [201], this is only so when at least the shape of the curvature is preserved. The smallest scale for the liquid shape and the Young-Laplace equation to remain valid has been estimated to

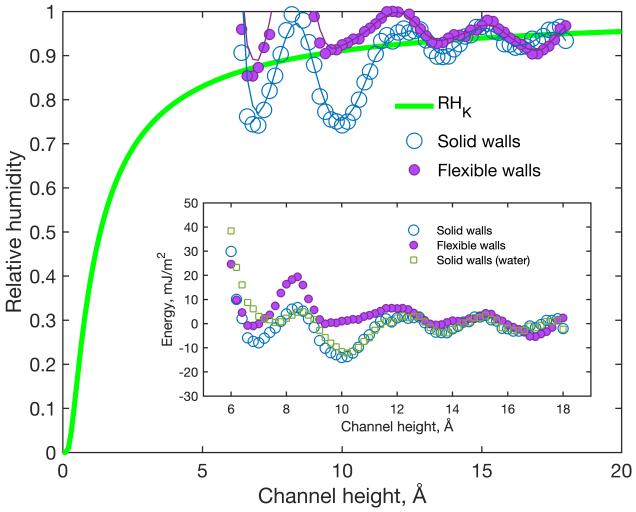

Figure 7.3: The macroscopic Kelvin equation (RH_K, represented by the green line) and the adjusted Kelvin equation, accounting for variations in γ_{sl} concerning channel height for solid (depicted as open blue circles) and flexible (shown as purple filled circles) nanochannel walls. Inset: Depictions of the system's potential energy variations concerning the channel height for both rigid and flexible walls. Additionally, the potential energy of water molecules (for the solid walls approach) is illustrated.

be about 3–4 molecular diameters (σ) with σ being 0.5 nm [202]. In the situation of plug flow profile, where there is no meniscus, it is better to disregard the Laplace pressure and attribute the entire contribution of the capillary pressure to the disjoining pressure. It is worth noting that this replacement in the term of pressure difference does not invalidate the derivation of the Kelvin equation [196, 203]. The other quantities can be obtained by equating the grand potential functions of the liquid and gas sides (or heuristically by writing the hydrostatic pressure drop of the water and gas columns in a Jurin-like experiment [196, 203]) and do not depend on the confinement.

The disjoining pressure, in turn, can be expressed as the sum of van der Waals (vdW) and structural terms. There are some other contributing terms, but the main contribution is from the two mentioned terms [19, 73]. The vdW contribution to the disjoining pressure can be estimated as:

$$P_{vdW} = A_{vdW}/6\pi h^3 \tag{7.1}$$

with A_{vdW} being the Hamaker constant for water-graphite interaction ($1.15 \times 10^{-19} J$) [19, 73, 204]. The structural term in the disjoining pressure for hard spheres confined in a 2D slit pore can be expressed as:

$$P_{str} = -(1/\sigma^3)k_B T cos(2\pi h/\sigma)exp(-h/\sigma) \tag{7.2}$$

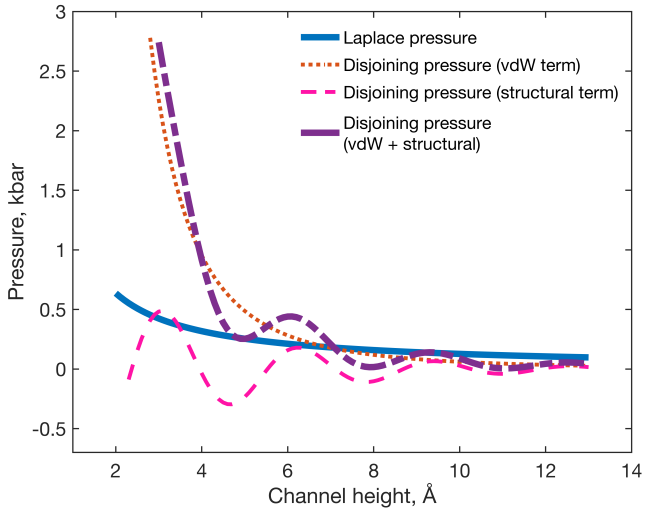

Figure 7.4: Predictions of Laplace pressure and disjoining pressure that are close to each other at h around 1 nm.

with k_B being the Boltzmann constant and σ being the molecular diamater (3.16 Å) [19, 205].

To gain a better understanding, we show in Fig. 7.4 the predictions of disjoining pressure (sum of vdW and structural terms) and what the Laplace pressure would predict (for a water-graphene contact angle of 85°). Notice that the predictions are coincidentally close to each other for h values that are relevant to us (around 0.8 to 1.3 nm). We hypothesize that it is the negative disjoining pressure that causes the vapor above the water column to condense at a lower pressure than would be required for condensation over a flat surface, and the vapor pressure ratio is quantitatively consistent with the Kelvin equation. The only term in the Kelvin equation capable of accounting for fluctuating relative humidity is the pressure difference term. It is especially noteworthy that the disjoining pressure demonstrates this fluctuating behavior through the cosine function of its structural term, while the Laplace pressure does not. Drawing from this hypothesis, we compare the predictions of the revised Kelvin equation with experimental data sourced from ref. 70 (see Fig. 7.1). The remarkable agreement between theoretical predictions and experimental observations underscores the capacity of the revised Kelvin equation to precisely capture capillary condensation at the nanoscale.

7.4 The prevalence of disjoining pressure

We argue that more solid evidence is needed to confirm that the capillary pressure, at least in small channel heights, is fluctuating. Let us examine the fluid flow in a narrow capillary, whose driving force is the capillary pressure and the resisting force is the viscous friction. It is worth noting that the gradient of hydrostatic pressure is much smaller than the negative capillary pressure, obviating the need to consider the viscous

pressure drop along the water column.

Due to the very small characteristic length (and Reynolds number), we may assume that the flow is steady and fully developed both hydrodynamically and thermally. Therefore, unlike some studies of decelerating flow [206], we may assume that the material derivative of the velocity field in the flow direction is zero, and simplify the momentum conservation equation to $\nabla.T = -\nabla P$, where T is the viscous pressure tensor and P is the hydrostatic pressure [207]. Moreover, we avoid expressing the shear stress in terms of the velocity gradient and reasoning based on the Poiseuille relation (unlike ref. 208) because although water is Newtonian and the flow (of a few layers of fluid) could be regarded as laminar (such that the fluid deformation can be estimated as the velocity gradient), the gradient of velocity at the fluid-wall interface would be undefined. We thus directly reason based on the shear stress, which has also been recognized as the key factor for the flow properties [206]. Therefore, if capillary pressure is going to fluctuate, then shear stress also needs to fluctuate.

Let us assume that the Reynolds analogy is valid. It means the shear stress is proportional to the heat flux toward the wall. Considering the flow as a few fluid layers moving in parallel, it conforms to laminar flow. Consequently, the heat flux at the wall interface can be interpreted as molecular conduction, defined by Fourier's law ($\dot{q} = -k\frac{dT}{dy}$), and the shear stress by Newton's law of viscosity ($\tau_w = \mu\frac{\partial u}{\partial y}$). In these formulas, $\dot{q}$ represents heat flow, τ_w is shear stress, k is thermal conductivity, μ is viscosity, T is temperature, u is velocity, and y refers to the direction perpendicular to the wall. Thus, the ratio of heat flow to shear stress is expressed as:

$$\frac{\dot{q}}{\tau_w} = -\frac{k}{\mu}\frac{dT}{du} \tag{7.3}$$

k/μ can also be written based on the Prandtl Number and specific heat capacity as c_p/Pr.

Now, our focus is to evaluate $\dot{q}/\tau_w$ at the wall interface, specifically examining whether the slight (sub-angstrom) variations in capillary width, causing commensurability effects, impact this ratio. Assuming both velocity and temperature profiles resemble plug flow, we anticipate dT/du to remain unaffected by commensurability. While fluid properties might fluctuate due to confinement (as discussed in the main text regarding the oscillatory behavior of surface tension), for our assessment at the wall interface, the structure of the initial fluid layer adjacent to the wall remains constant and unaffected by commensurability. Hence, it suggests a proportionality between heat flow and shear stress. In the context of our study, if one displays oscillation, the other is likely to do so too.

This argument can also be approached equivalently. Given the flow conditions, we assume that the boundary layer approximations govern the Navier-Stokes equations for both momentum and energy, which read:

$$u\frac{\partial u}{\partial x} + v\frac{\partial u}{\partial y} = \nu\frac{\partial^2 u}{\partial y^2} \tag{7.4}$$

$$u\frac{\partial T}{\partial x} + v\frac{\partial T}{\partial y} = \frac{\nu}{Pr}\frac{\partial^2 T}{\partial y^2} \tag{7.5}$$

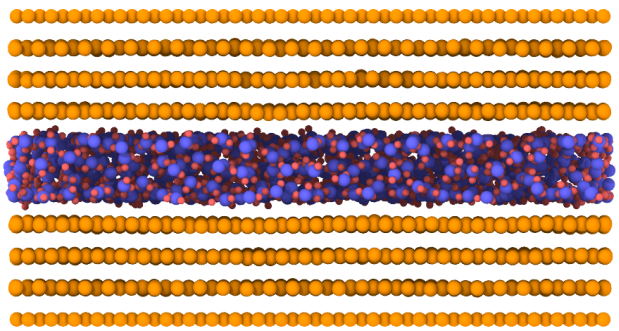

Figure 7.5: Schematic illustrating the molecular dynamics simulation system. Within this setup, calculations for Kapitza conductance, peak density of the initial water layer, and work of adhesion are conducted. The graphene sheets (6.1 nm × 5.5 nm) are represented with orange and the water molecules with blue (oxygen) and red (hydrogen) atoms.

where u and v denote the velocity components in the x and y directions respectively, and ν represents the kinematic viscosity.

Assuming fully developed flow (both hydrodynamically and thermally), the x-derivative terms can be disregarded. By dividing the above equations (and assuming the second derivative terms for velocity and temperature are equally small and can be simplified by each other), one can infer that du/dT is proportional to the Prandtl number, thereby supporting the earlier argument. Regarding the validity of boundary layer equations, it is worth mentioning that we are not going to select an infinitesimal control volume within the fluid and examine the spatial stress and heat flux vectors, so we do not need to worry about the effects of discontinuity. In essence, as the parameters at the wall interface are our focus, the control volume can encompass the entire capillary width.

The temperature profile will also have a plug flow profile (no temperature gradient), thus the heat flux can be attributed to the Kapitza conductance (G_K) at the interface. Now, G_K can be computed using MD simulations. From the literature, it is generally accepted that the Kapitza resistance ($R_K = \Delta T/G_K$, interface temperature jump divided by the Kapitza conductance) is independent of the fluid thickness (see refs. 209 and 210 for fluid thickness down to 1 nm and 2 nm, respectively). However, what has been reported is for fluid thickness with variations of 1 nm interval. What happens if G_K is examined in intervals of e.g. 0.2 Å? To the best of our knowledge, such an investigation of G_K has not been done to date. We therefore calculate G_K for water confined between graphene sheets with the channel height ranging from 10.05 Å to 16.75 Å, corresponding to two to four graphene spacers in relevant experiments [70, 208].

For each value of h, the number of water molecules is adjusted to yield the bulk density

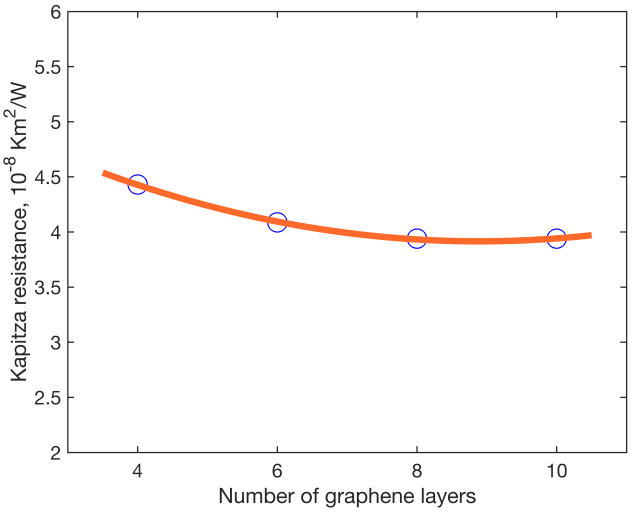

Figure 7.6: Variations of the Kapitza resistance with the number of graphene layers. Number of graphene layers has little effect on the Kapitza resistance. The solid line is a guide to the eye.

for the channel geometry, as density has been found to change little with confinement [208]. Fig. 7.5 shows a snapshot of the simulated system. It is worth noting that the impact of the number of graphene layers on R_K is a contentious matter in the literature [209, 210]. Having established the MD simulation framework for computing G_K, we seek to address this contentious issue.

Alexeev et al. [209] demonstrated a strong correlation between R_K and the number of graphene layers, observing a decrease in R_K that stabilizes at an asymptotic value as the layers increase. Conversely, Alosious et al. [210] proposed a minimal decrease in R_K with an increased number of graphene layers, suggesting that the Kapitza length remains largely unaffected by the number of layers.

Here, we constructed a sufficiently wide nanochannel (3 nm height) and computed R_K for nanochannel walls comprising four, six, eight, and ten graphene sheets on each side. The results depict only a slight reduction in R_K with the number of graphene layers (see Fig. 7.6). Therefore, we propose that the number of graphene layers does not significantly impact R_K. This subtle decline can be attributed to the increased number of permissible phonon modes in graphene [210]. It appears that the utilization of the Tersoff potential [156] can induce mechanical instability in graphene sheets, potentially altering the initial density peak and consequently affecting R_K. Hence, we suggest employing the Airebo potential [117] (despite increased computational costs) or implementing a methodology similar to the constrained approach in ref. 210 by resetting the center of mass of each graphene sheet to its initial position after every MD step.

R_K has been known to inversely scale with the magnitude of the density peak of the first water layer adjacent to the interface (ρ_m) [209, 210]. On the other hand, G_K has been recognized to be directly proportional (linear relationship without y-intercept) to W_{sl} [75]. Therefore, in addition to G_K, we also calculate ρ_m and W_{sl} so that we can examine

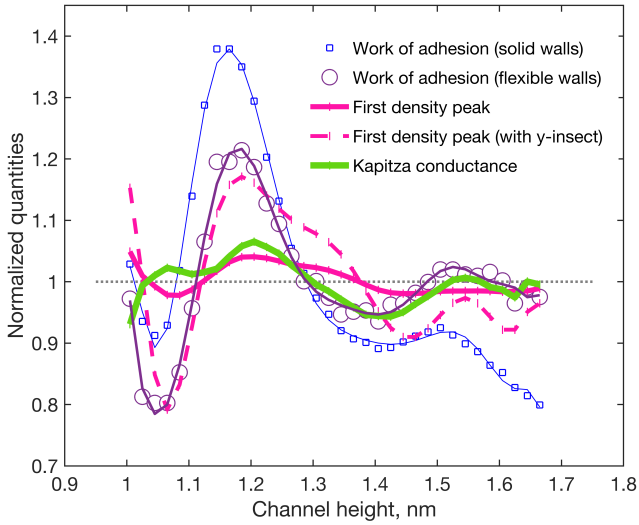

Figure 7.7: Normalized work of adhesion (W_{sl}) for solid and flexible graphene walls (shown with square and circle symbols respectively, with solid lines provided as a guide to the eye), Kapitza conductance (G_K) and first density peak (ρ_m). The normalization for each quantity is performed by dividing by their respective mean values. Direct proportionality of work of adhesion and Kapitza conductance holds true down to channel height of 1.3 nm. For very narrow channels, the parameterized first density peak can provide an accurate estimate of the work of adhesion.

all quantities together. ρ_m is extracted from the same simulation system used for G_K. It is worth noting that for our study with only two to three layers of water and almost no temperature gradient across the channel height, the temperature jump at the interface was the same for different channel heights. Therefore, we directly discuss G_K rather than R_K and expect a linear relationship between the G_K and ρ_m.

In the literature, estimations of W_{sl} are mostly based on the assumption that it scales with $1 + cos(\theta)$, where θ is either computed directly or, when it is ill-defined, assumed to linearly scale with the Lennard-Jones energy parameter of the interface interactions [211, 212]. Here, we calculate W_{sl} directly using its definition from the interfacial energies. This is useful when considering the previously mentioned concerns about the validity of Young's equation, as well as for testing whether W_{sl} still maintains a direct proportion to G_K in the case of confined water. To calculate the work of adhesion, we employ a modified version of the so-called phantom-wall method [213, 214], relying on thermodynamic integration. In the following, we elaborate on the phantom-wall method and outline our modifications to it.

The results for W_{sl}, G_K and ρ_m are shown in Fig. 7.7, each normalized by their respective mean values, across channel heights ranging from 10.05 Å to 16.75 Å. Interestingly, all quantities are fluctuating. Therefore, we conclude that the capillary pressure is fluctuating and the disjoining pressure dominates.

When the capillary pressure is dominated by the cosine function of the disjoining pres-

sure, there are certain values of film thickness for which the curvature of the film energy is negative. In these regions, the film is dawnwardly unstable and would tend to break into two films of larger and smaller thicknesses, which coexist with the same film tension ($P(h) + h\Pi(h)$) [215]. It is beyond the scope of this study, but it would be interesting to investigate the interplay of the tendency to increase the film thickness with the flexibility of the graphene walls, as well as the filling of the channel as a result of the tendency to decrease the film thickness.

7.5 breakdown of proportionality between kapitza conductance and work of adhesion

As shown in Fig. 7.7, the normalized W_{sl} and G_K coincide consistently over a considerable variation in channel height, indicating the validity of the direct proportionality for the confined water-graphene interface. However, this correlation weakens for channel heights below 1.3 nm, and when the heights are less than 1 nm, G_K even fails to predict the extremum points of W_{sl}. On the other hand, ρ_m accurately predicts the extremum points. Through the addition of an arbitrary constant to ρ_m (while preserving its linear relationship), it achieves reliable estimations of W_{sl}, even in the narrowest channels. Therefore, when empirically parameterized, ρ_m proves highly effective in probing W_{sl}. Unlike some studies in the literature [174, 216], our calculation of the work of adhesion with rigid solid walls did not produce favorable outcomes (blue squares). Therefore, we recommend using simulations involving flexible walls for determination of W_{sl}.

Even though G_K displays oscillating behavior, the amplitude of these oscillations remains within 10 percent. Thus, the qualitative independence of R_K on the fluid thickness persists. [209, 210]. The oscillation amplitude of W_{sl} reaches approximately 20 percent. Considering that γ_{sl} for the water-graphene interface is estimated to be only around five percent of the surface tension of water [200], it is improbable for γ_{sl} to exhibit an oscillation amplitude a few times larger than its value. Therefore, the anticipation is that γ oscillates due to confinement, despite the notion of surface tension as an intrinsic property of water valid down to the nanoscale [201]. This is another instance demonstrating the impact of confinement on material properties, a phenomenon we have previously explored in other examples [59].

One pertinent question arises: in a scenario where commensurability induces fluctuating behaviors across all quantities—especially capillary pressure as the driving force and shear stress at the wall as the resisting force—does the flow velocity relative to the channel height also exhibit fluctuations? Specifically, following the Poiseuille relation, would u/h^2 (where u represents the flow axial velocity, or u/h with boundary slip assumptions) demonstrate oscillations? Our consideration suggests that this could be the case, provided that viscosity remains constant.

There is an anticipation of reduced viscosity near hydrophobic walls [202, 217, 218]. Following an extensive literature review, Wu et al. [218] estimated the interface region (where viscosity is significantly affected) to extend approximately 0.7 nm for the water-graphene interface. Consequently, for channels less than 1.4 nm in height, it is anticipated that the reduced viscosity within the interface region spans the entire height. This 1.4 nm

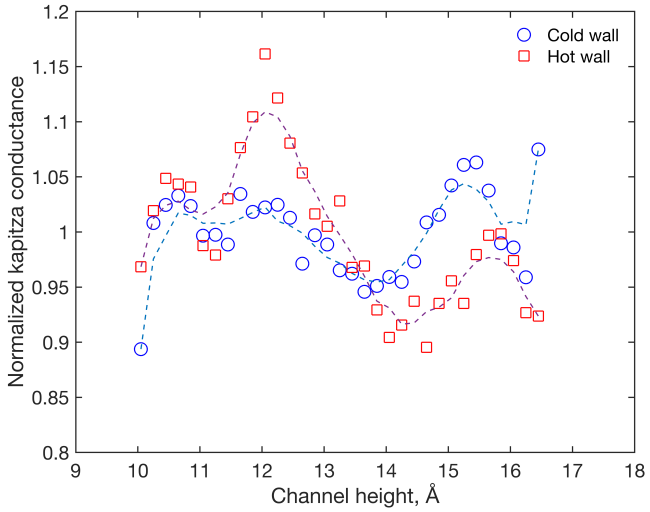

Figure 7.8: Normalized Kapitza conductance for hot and cold surfaces. The Kapitza conductance is higher at the cold surface up to a capillary height of 1.3 nm, below which the hot surface exhibits a higher Kapitza conductance. The dashed curves are guide to the eye.

channel height notably aligns with the channel height at which a substantial enhancement in flow rate is observed (refer to Fig. 3b of ref. 208).

It deserves special attention that while explaining the flow enhancement, Radha et al. did not account for spatially varying viscosity (compare Equation 1 in ref. 208 with Equation 7 in ref. 218). Instead, they attributed the flow enhancement to the summation of Laplace pressure and disjoining pressure within the Poiseuille relation. As a result, their hypothesis could only predict a flow enhancement of up to 2-3 times, whereas their experiment exhibited around a 10-fold increase (compare the main panel of Fig. 2b in ref. 208 with its inset). Estimating viscosity as in a real experiment, however, is not trivial by MD, because besides the structure of water, the gas nucleation near the hydrophobic walls plays a role in viscosity reduction as well [217]. To sum up, within capillaries of molecular heights, the pronounced variations in viscosity adjacent to hydrophobic walls are likely to override any induced oscillatory patterns in flow velocity.

Let us explore why G_K has lost its direct proportionality with W_{sl}. In non-equilibrium studies of R_K, whether R_K is higher at the hot or cold surface is controversial [209, 210, 212, 219–221].

In the study conducted by Alexeev et al. [209], they observed a ΔT at the cold surface with nearly equivalent heat flux for both surfaces (inferred from the gradient of their reported temperature profile), leading to an elevated R_K for the cold surface. This trend is similarly reported by Alosious et al. [210] Ramos-Alvarado et al. [212] reported an almost identical ΔT with approximately 10 percent higher heat flux at the hot surface, resulting in a higher R_K at the cold surface. In contrast, Kim et al. [219] as well as Barrat and Chiaruttini [220] reported higher ΔT and R_K at the hot surface. Murad and Puri [221] observed a higher R_K at the cold surface, despite their temperature profile

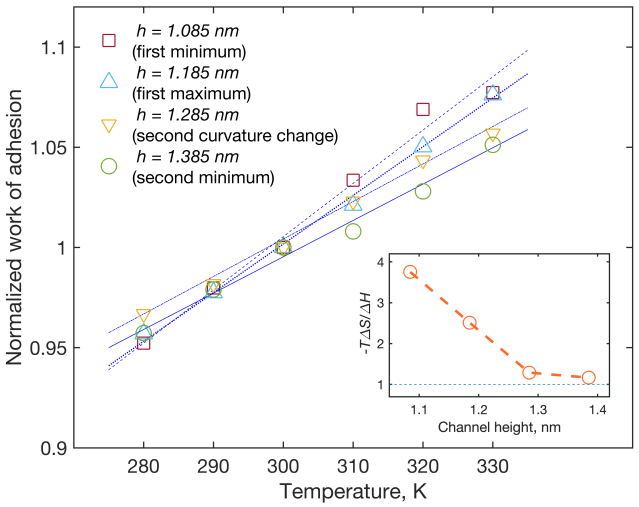

Figure 7.9: Variations of the work of adhesion with temperature. The ascending trend indicates a reduction in entropy resulting from the separation of water from the graphene wall. The dashed lines are guide to the eye. Inset: At very narrow capillaries, entropy dominates the work of adhesion.

indicating a higher ΔT at the hot surface and higher heat flux at the cold surface. It is worth noting that in their study, heat flux was not calculated using MD but was derived using Fourier's law and correlating equations for the thermal conductivity of the water substance, a method that might need more examination at the nanoscale.

What we showed in Fig. 7.7 was the average of the hot and cold surface. Fig. 7.8 illustrates G_K separately for the hot and cold surfaces (normalized by their mean value). G_K at the cold surface is higher for channel heights down to 1.3 nm, while for narrower channels, the hot surface displays a higher G_K. In wider channels, the fluid demonstrates a more ordered arrangement at low temperature, yielding enhanced heat transfer. However, in very narrow channels, the fluid is highly confined and ordered, displaying similar characteristics on both surfaces. Consequently, higher temperatures induce thermal movement of particles, leading to improved heat transfer. Interestingly, this 1.3 nm height corresponds to the point at which the dominance in W_{sl} shifts from energy to entropy, resulting in G_K losing its proportionality with W_{sl} .

To investigate further, we study the effect of temperature on W_{sl}. We select four channel height values according to Fig. 7.7: the first minimum (h = 10.85 Å), the first maximum (h = 11.85 Å), second curvature change (h = 12.85 Å), and the second minimum (h = 13.85 Å), and calculate W_{sl} across temperatures ranging from 280 K to 330 K (see Fig. 7.9). For each h, W_{sl} is normalized to its value at 300 K (same data of Fig. 7.7). By fitting a line to the data, we can distinguish the enthalpy and entropy contributions ($A\Delta\gamma = \Delta H - T\Delta S$). Surprisingly, the curves are ascending ($\Delta S < 0$). This contradicts the entropy increase at the graphene with bulk water interface as the effect of the phantom wall [200].

The slopes of the lines decrease with increasing channel height. The inset of Fig. 7.9

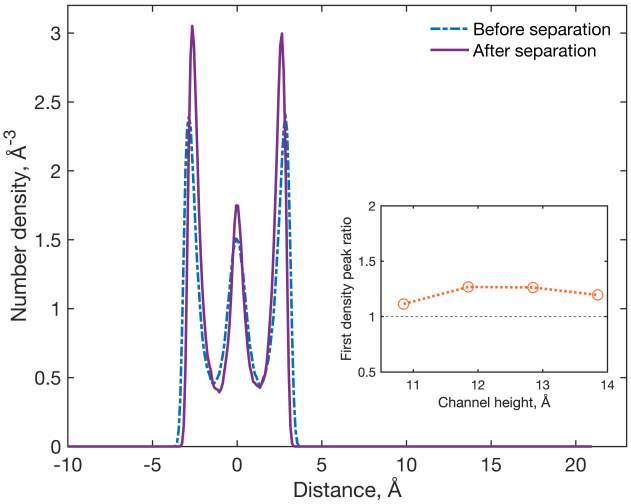

Figure 7.10: Number density profile of water atoms before and after the separation of water from the graphene wall. Inset: Ratio of the peak number density values after and before the separation of water from the graphene wall. The separation process leads to an increased order in water molecules.

shows the ratio of $T\Delta S$ (at $T = 300K$) to ΔH. Interestingly, the entropy and enthalpy contributions are of the same order of magnitude, and for the two narrower channels, entropy holds a significant dominance. The observation of changing the trend of hot and cold surfaces in G_K at $h \sim 1.3$ nm, as well as the dominance of entropy in W_{sl} at the same height, which is remarkably the same height at which G_K loses its agreement with W_{sl}, leads us to conclude that the direct proportionality is a consequence of proportionality between the energy transfer and adhesion energy at the interface.

To further investigate the unexpected increase in $W_s l$ with temperature (see Fig. 7.9), we plot the number density profile of water for $h = 11.85$ Å before and after the influence of the imaginary wall (see Fig. 7.10). Evidently, the initial density peak appears higher following the impact of the imaginary wall. This contrasts with the behavior observed in bulk water [200]. It seems that the presence of a graphene wall on one side is sufficient to induce a well-layered structure in the water, resulting in lower entropy.

7.6 Modified phantom-wall method for calculating interfacial free energy

In this section, we will elaborate on the modified version of the so-called phantom-wall method [213, 214], which we use to calculate the work of adhesion.

Efforts to calculate interfacial free energies have a significant presence in the literature [222–230]. One pivotal work was conducted by Kirkwood and Buff [222], establishing a link between surface free energy and stress anisotropy at the interface. Originally devised

for fluid-fluid interfaces, this research was subsequently expanded upon by Navascués and Berry [223] to address solid-liquid interfaces, treating the solid as a time-independent external field at the interface with the fluid.

The method, termed the mechanical route, relies on spatially integrating the system's stress anisotropy, as outlined by Sikkenk et al. [231]. For this integration to be well-defined, it is critical that the anisotropy disappears at the integration limits. While this criterion is easily met when both phases are fluids, the presence of a solid phase introduces complexities. Size effects can only be nullified if the solid extends infinitely in space [214]. However, when dealing with actual solids, which often have limited spatial extent, calculating free energy at their surfaces becomes challenging. The interfacial region encompasses a substantial portion of the solid, causing ambiguity and a prevalence of size effects [213]. Additionally, it is important to note that stress calculations within the solid are primarily governed by inter-molecular forces rather than inter-diffusion, making these computations highly reliant on the force fields used to describe the solid [214].

The so-called phantom-wall method, introduced by Leroy et al. [213, 214], addresses these limitations. Instead of directly calculating the absolute interfacial free energy for a specific structured solid, this method first computes the interface free energy for a reference system. Subsequently, the interface free energy of the actual surface is determined relative to the reference system through thermodynamic integration.

The reference system comprises the interface of the identical liquid with a perfectly flat two-dimensional wall, referred to as the imaginary wall. This approach simplifies the system's stress anisotropy, reducing it to the stress distribution within the liquid. This distribution can be obtained using the mechanical route.

The transition from the reference system to the actual system occurs in stages: Firstly, the imaginary wall is placed within the real solid, running parallel to the genuine interface. It exclusively interacts with the liquid particles, devoid of any interaction with the solid particles. Positioned initially at a considerable distance from the liquid—beyond the MD cutoff distance—the imaginary wall ensures no interaction between the liquid and itself.

Afterward, the imaginary wall incrementally approaches the interface while remaining parallel, thereby influencing the liquid's behavior. This gradual movement persists until the imaginary wall creates separation between the liquid and the authentic surface. Ultimately, the liquid is positioned at a significant distance from the real surface, interacting solely with the imaginary wall. This transformation facilitates the conversion of the actual system into an imaginary system, enabling straightforward calculation of stress anisotropy using the mechanical route.

The conversion between the two systems needs to occur gradually to prevent imposing macroscopic temperature or pressure gradients on the system. This step ensures the process maintains thermodynamic reversibility, avoiding the introduction of sources of irreversibility (entropy generation). Consequently, the alteration in the system's free energy throughout the process equals the difference between the interfacial free energies of the actual and reference systems.

Moreover, it is evident that the alteration in the system's free energy equates to the work conducted by the imaginary wall throughout its operation (for an analytical proof, see

213). This work can be readily obtained by integrating the force-displacement behavior of the imaginary wall.

Leroy et al. [213, 214] conducted MD simulations employing the phantom-wall method within the isobaric-isothermal (NPT) ensemble, utilizing the Gibbs free energy as the thermodynamic potential. As a result, part of the system's free energy change during the surface conversion can be attributed to the $P\Delta V$ term (readily obtainable), while the remaining component reflects the alteration in interfacial free energies.

Our modification to the phantom-wall method is as follows: when simulating the system in the NPT ensemble during MD, the volume and configuration of the fluid change. However, this approach is not suitable for studying the interfacial free energy in confined systems. In our method, the system is simulated in the canonical (NVT) ensemble, preserving the structure of the capillary.

In our method, as the imaginary wall shifts slightly into the fluid domain, the confining wall moves away from the fluid at an identical rate to the imaginary wall. This simultaneous movement effectively substitutes the solid-fluid interface with the phantom wall while preserving the structure of the confined fluid. However, a limitation of our modification arises from the complete confinement of the fluid, where the stress anisotropy in the reference system does not necessarily vanish. As a result, the mechanical route cannot be applied.

Nevertheless, if the phantom wall is designed to be purely repulsive, the fluid-phantom wall interface is equivalent to the interface between the fluid and its vapor [200]. As a result, the work done by the imaginary wall is equal to $(\gamma - \gamma_{sl})$, which, when neglecting γ_{sv} [232, 233], equals the work of adhesion.

With temperature and specific volume, both intensive thermodynamic properties, maintained constant in our system, we anticipate the thermodynamic state of our system to remain constant throughout the process. This means that $\Delta(PV)$ is constant, and the overall alteration in the system's free energy can be attributed solely to the difference in interfacial free energies between the actual and reference systems. This requires the convergence of Gibbs and Helmholtz free energies, similar to the assumption made in the work by [200], where internal energy and enthalpy were considered equal.

7.7 Conclusion

Recent experiments have surprisingly shown that the macroscopic Kelvin equation accurately predicts capillary condensation for capillaries as thin as 1 nm. We therefore employed molecular dynamics simulations to analyze and understand the mechanisms behind the capillary condensation of water in graphene nanocapillaries.

We identified weaknesses in the hypothesis from previous literature that suggested commensurability-induced oscillations in liquid-solid interfacial free energy were responsible for this phenomenon. Found weaknesses include inaccuracies in estimating the liquid-solid interfacial free energy, neglecting the entropic contributions in free energy assessments, and the improper application of Young's equation in the absence of a meniscus in the liquid film. Instead, we proposed an alternative hypothesis, namely

that the condensation occurs due to the disjoining pressure whose value is close to the Laplace pressure at the relevant channel height. This leads to the occurrence of capillary condensation at relative humidity levels close to the predictions of the Kelvin equation.

To support our hypothesis, we assumed the Reynolds analogy, as well as leveraged the previously established direct proportionality between Kapitza heat conductance and the work of adhesion. These steps enabled us to assess the capillary pressure by determining interfacial heat transfer and calculating the work of adhesion directly based on the definitions of interfacial energies. In these assessments, we discovered that commensurability induces oscillatory behavior in all quantities, including Kapitza conductance, work of adhesion, and the first density peak of confined water. We found that the direct proportionality between the work of adhesion and Kapitza conductance remains valid in confined liquid circumstances, but it breaks down in very narrow capillaries where the work of adhesion is dominated more by entropy than by energy. In contrast to bulk water conditions, for strong confinement, separating water and graphene requires overcoming both the adhesion energy and the decrease in entropy. Nevertheless, the work of adhesion can be accurately predicted by empirically parameterizing the first density peak of water, even in the narrowest capillaries.

Finally, we investigated a controversial issue in the literature regarding the influence of the number of graphene layers on Kapitza resistance and found that it is practically unaffected by the number of graphene layers. All together, our study provides a thorough account of the fundamental principles governing the capillary condensation in nanocapillaries, and offers fresh perspectives on interfacial bonding and thermal transport in ultimately constrained systems.

Chapter 8

Comment on "Misinterpretation of the Shuttleworth equation"[¶]

*In a published paper (Scripta Materialia, **2012**, 66, 627–629), it is concluded that the so-called Shuttleworth equation holds no implications for the relationship between surface tension and surface energy. In this chapter, we provide clarifications to demonstrate that this conclusion is not valid.*

In Ref. 234, Makkonen asserts that the so-called Shuttleworth equation 'reduces to the definition of surface tension derived from mechanics' and that 'it does not provide an additional law of surface physics.' We respectfully disagree with Makkonen's interpretation.

Shuttleworth (1949) demonstrated [77] that 'the surface tension of a crystal face is related to the surface free energy by the relation

$$\gamma = F + A(dF/dA) \tag{8.1}$$

where A is the area of the surface', γ is the surface tension, and F is the specific surface free energy, with $F = H/A$, H being the total Helmholtz free energy.

Since then, numerous claims both in support [78–82] and criticism [83–88] of this equation's derivation and its consistency with Hermann's mathematical structure of thermodynamics have been raised. We do not intend to stir these discussions further; rather, our aim is to challenge Makkonen's viewpoint as presented in Ref. 234.

Let us first clarify the terms *surface tension* and *surface stress*. In the literature, there are cases where surface tension is defined as the reversible work required to create a surface per unit area, similar to Gibbs' introduction [80]. Nevertheless, when Shuttleworth states 'the surface tension is the tangential stress,' he is specifically referring to surface stress within the surface layer in his equation and discussions.

Let us now explore Makkonen's perspectives. Makkonen defines surface stress as the strain derivative of the total free energy, i.e.

[¶] This chapter contributed to the paper: Comment on "Misinterpretation of the Shuttleworth equation". Scripta Materialia **250**, 116186 (2024)

$$\gamma = \frac{\partial H}{\partial A} \tag{8.2}$$

This definition is certainly accurate but not aligned with Makkonen's intended use. Expanding the differential dH as $AdF + FdA$ indeed yields Eq. 8.1. However, there are a few considerations to note here. Makkonen claims that Eq. 8.2 is the definition of stress 'in mechanics', but this is not accurate. Rather, it is the definition of stress in the thermodynamics of deformation [235]. The definition of stress in mechanics is typically based on Cauchy's stress principles, representing the surface force per unit area (or line) that tends to return the deformed mass to its mechanical equilibrium state. This understanding of stress predates the introduction of free energy. When discussing surface stress, it is essential to consider the *excess* stress (either positive or negative) in surface atoms compared to bulk atoms, necessary to keep surface atoms in their positions as if they were in the bulk. While the interpretation of excess properties dates back to the era of Gibbs, it extends beyond free energy and can relate to any extensive thermodynamic property. Therefore, the definition of surface stress is not contingent upon the interpretation of free energy. Shuttleworth effectively discusses excess stress without directly referring to Gibbs' formulation.

Shuttleworth interprets an infinitesimal elastic change in the surface of a solid in terms of both mechanics and thermodynamics, which lead, respectively, to the left and right sides of his equation. Makkonen, on the other hand, solely relies on thermodynamic evaluations and asserts that the Shuttleworth equation is trivial. This approach over-simplifies the matter. To draw a parallel in fluid dynamics, it is akin to defining the components of the velocity field for an incompressible flow as derivatives of the stream function ($u = \partial\psi/\partial y$, $v = -\partial\psi/\partial x$) and concluding that the law of continuity holds no additional implication and essentially reduces to the definition of velocity (since it inherently satisfies itself when defined through the stream function). It is also analogous to stating that the Young-Laplace equation, which estimates the pressure difference over a curved interface, is essentially a result of static equilibrium and basic geometry. We agree with Makkonen in acknowledging that the Shuttleworth equation is not a 'law of surface physics' but rather an equation, as initially asserted by Shuttleworth himself.

Additionally, Makkonen states, 'the evaluation of surface stress should be based on its mechanical definition, as outlined by Gurtin and Murdoch [236] and Wolfer [237].' Gurtin and Murdoch's work does not directly reference free energy, and Wolfer defines surface stress as $\partial F/\partial\epsilon$ (ϵ being the strain, similar to the Gibbs formulation). Deriving Eq. 8.2 from $\partial F/\partial\epsilon$ requires keeping A constant, or essentially neglecting FdA in contrast to AdF. This essentially brings Makkonen's arguments back to Gutman's objections to Shuttleworth [83], which have been thoroughly discussed by Kramer and Weissmüller [80]. While thermodynamic properties need to be interpreted in their unstrained state, this does not imply that, in an Eulerian derivation where measurements are taken in a deformed state (similar to Shuttleworth's approach), one could neglect dA meanwhile the derivation.

To sum up, is Eq. 8.2, as used by Makkonen, incorrect? No, but referencing $\partial F/\partial\epsilon$ introduces unnecessary confusion regarding the proper definition of specific free energy [80]. A simpler and more appropriate formulation could be to simply relate the work required for infinitesimal deformation to the differential of the extensive total free energy, similar to Shuttleworth's approach. It is still appropriate for Makkonen to use $F =$

H/A (similar to Shuttleworth), in contrast to several other works that use $F = \partial H/\partial A$ [85, 87, 238], as with the latter definition it is impossible to derive Eq. 8.1 from Eq. 8.2.

Now, what are the implications of the Shuttleworth equation? The Shuttleworth equation is designed specifically for properly defined elastic strains and should not be interpreted beyond its intended scope. For instance, Gutman's arguments [83] concerning the movement of atoms from the bulk to the surface, as in the case of liquids, are not appropriate, because Shuttleworth explicitly hedged 'provided the deformation is reversible'.

Regarding liquids, although dF/dA is zero, which simplifies the Shuttleworth equation to $\gamma = F$ (making it trivial for liquids), it should not be applied in this context. This is due to the pressure gradient at the surface relative to the bulk, which introduces a source of irreversibility. Even though the Shuttleworth equation coincidentally describes the end state of this process correctly, its derivation is not suitable for liquids. It would have been better if Shuttleworth had stated this explicitly.

Kramer and Weissmüller simply illustrate how the surface energy of solids may change without causing surface stress [80]. A broader discussion is available in Ref. 76, where it is elaborated how solids may have more than one stress-free configuration. Therefore, one excellent application of the Shuttleworth equation could be in wetting problems. In these scenarios, the surrounding thermodynamic conditions, such as interfacial free energy, can alter the stress distribution within the solid without changing its mechanical response.

Chapter 9

Conclusions and outlook

This comprehensive thesis is structured into six meticulously investigated segments, each examining different aspects of nanomechanics and interfacial physics. The initial section challenges a previously accepted universal aspect ratio, revealing substrate-dependent stability and aspect ratio in nanometer-sized bubbles on graphene. The exploration then extends to the indentation of graphene nanobubbles, uncovering failure points similar to those of viral shells, and investigating phase transitions of encapsulated noble gases. The third segment examines the formation of anomalous shapes in flat nanobubbles encapsulated by hexagonal boron nitride, highlighting the influence of heating rates and hydrogen bonds. The investigation proceeds to the cation-controlled permeation of charged polymers through nano-capillaries, uncovering distinct effects of monovalent cations on polymer transmission speed. The ability to control permeation is attributed to the varying surface versus bulk preferences of different alkali cations, particularly in the presence of an external electric field. The fifth segment critically examines the accuracy of the Kelvin equation in nanoscale capillaries, challenging conventional explanations and proposing a revised understanding based on disjoining pressure. Finally, the concluding segment provides critical commentary on the Shuttleworth equation, rectifying misconceptions and contributing to a comprehensive understanding of interfacial thermodynamics. Collectively, this thesis offers nuanced insights into the intricate interplay between confinement, material properties, and interfacial thermodynamics, significantly advancing our understanding of these complex phenomena.

While this research represents a significant advancement, it does not mark the conclusion of our efforts. In the study of nanobubble morphology, a notable oversimplification is the exclusive focus on pure energetics analysis, neglecting the critical role of entropy. Specifically, when calculating the adhesion energy between the trapped materials and the respective crystals, it is essential to consider the variation in the system's free energy during the separation of the materials at the interface, known as the work of adhesion. As discussed in chapter 7, for the interface of graphene with bulk water, the entropy contribution to the work of adhesion constitutes approximately one-third of the energy contribution. Moreover, we demonstrated in chapter 7 that for the same interface, when water is confined, the entropic contribution is of comparable magnitude to the energy contribution. In very narrow confinements, entropy even predominates.

Furthermore, as elucidated in chapter 4, we discovered that in small bubbles, the trapped materials undergo solidification at room temperature, even at pressures lower than the

predicted melting pressure based on their phase diagram. Given the likely solidification and crystalline structure of the trapped materials, neglecting entropy can lead to misleading conclusions. Another critical aspect in evaluating interfacial free energy is its impact on the mechanical response of crystals interfacing with fluids. As discussed in chapter 8, the thermodynamics of the surroundings may alter the thermodynamics of the stresses in the solid, but not their mechanical response. Therefore, the study of interfacial free energies in the nanobubble system is of significant importance. This aspect is notably absent in the existing literature and constitutes a primary objective for future research.

Nanobubbles also hold significant potential in facilitating chemical reactions within them, making the study of heat transfer inside nanobubbles critically important. Given the very small length scales of these bubbles, heat transfer is expected to be governed by interfacial thermal resistance, known as Kapitza resistance. In chapter 7, we demonstrated how confinement-induced commensurability inside nano-capillaries can influence Kapitza resistance. Additionally, within nanobubbles, the trapped materials experience extreme hydrostatic pressure, typically on the order of tens of gigapascals (see chapter 3). High pressure is expected to impact Kapitza resistance. There is a significant gap in the literature regarding the investigation of thermal resistance at interfaces within nanobubbles, underscoring the importance of this aspect in future research.

Future research should also aim to evaluate the solid surface free energy (γ_{sv}) for the deformed crystal and the substrate. Utilizing the phantom-wall method (see chapter 7) provides $\gamma - \gamma_{sl}$, which equals the work of adhesion only when γ_{sv} is disregarded. While this disregard may be valid for the graphene-bulk water interface, it is not applicable to the nanobubble system, necessitating the evaluation of γ_{sv}. Extensive thermodynamic properties of a solid film, including its free energy, exhibit an excess value at the surface compared to their bulk value. Specifically, the solid surface undergoes strain proportional to γ_{sv}/Y, where Y represents its two-dimensional Young's modulus, influencing the electronic properties of the crystal. Therefore, studying γ_{sv} in the nanobubble system holds great significance and represents another primary objective for future research.

Bibliography

[1] Francesco Fornasiero, Hyung Gyu Park, Jason K Holt, Michael Stadermann, Costas P Grigoropoulos, Aleksandr Noy, and Olgica Bakajin. Ion exclusion by sub-2-nm carbon nanotube pores. *Proc. Natl. Acad. Sci. USA*, 105(45):17250–17255, 2008. 1, 79

[2] Alessandro Siria, Philippe Poncharal, Anne-Laure Biance, Rémy Fulcrand, Xavier Blase, Stephen T Purcell, and Lydéric Bocquet. Giant osmotic energy conversion measured in a single transmembrane boron nitride nanotube. *Nature*, 494(7438):455–458, 2013.

[3] Eleonora Secchi, Sophie Marbach, Antoine Niguès, Derek Stein, Alessandro Siria, and Lydéric Bocquet. Massive radius-dependent flow slippage in carbon nanotubes. *Nature*, 537(7619):210–213, 2016.

[4] Eleonora Secchi, Antoine Niguès, Laetitia Jubin, Alessandro Siria, and Lydéric Bocquet. Scaling behavior for ionic transport and its fluctuations in individual carbon nanotubes. *Phys. Rev. Lett.*, 116(15):154501, 2016.

[5] Ramya H Tunuguntla, Robert Y Henley, Yun-Chiao Yao, Tuan Anh Pham, Meni Wanunu, and Aleksandr Noy. Enhanced water permeability and tunable ion selectivity in subnanometer carbon nanotube porins. *Science*, 357(6353):792–796, 2017.

[6] Slaven Garaj, W Hubbard, A Reina, J Kong, D Branton, and JA Golovchenko. Graphene as a subnanometre trans-electrode membrane. *Nature*, 467(7312):190–193, 2010.

[7] RK Joshi, Paola Carbone, Feng-Chao Wang, Vasyl G Kravets, Ying Su, Irina V Grigorieva, HA Wu, Andre K Geim, and Rahul Raveendran Nair. Precise and ultrafast molecular sieving through graphene oxide membranes. *Science*, 343(6172):752–754, 2014.

[8] Tarun Jain, Benjamin C Rasera, Ricardo Jose S Guerrero, Michael SH Boutilier, Sean C O'hern, Juan-Carlos Idrobo, and Rohit Karnik. Heterogeneous sub-continuum ionic transport in statistically isolated graphene nanopores. *Nat. Nanotechnol.*, 10(12):1053–1057, 2015.

[9] Jiandong Feng, Michael Graf, Ke Liu, Dmitry Ovchinnikov, Dumitru Dumcenco, Mohammad Heiranian, Vishal Nandigana, Narayana R Aluru, Andras Kis, and Aleksandra Radenovic. Single-layer MoS_2 nanopores as nanopower generators. *Nature*, 536(7615):197–200, 2016.

[10] Seunghyun Hong, Charlotte Constans, Marcos Vinicius Surmani Martins, Yong Chin Seow, Juan Alfredo Guevara Carrio, and Slaven Garaj. Scalable graphene-based membranes for ionic sieving with ultrahigh charge selectivity. *Nano Lett.*, 17(2):728–732, 2017.

[11] Jijo Abraham, Kalangi S Vasu, Christopher D Williams, Kalon Gopinadhan, Yang Su, Christie T Cherian, James Dix, Eric Prestat, Sarah J Haigh, Irina V Grigorieva, et al. Tunable sieving of ions using graphene oxide membranes. *Nat. Nanotechnol.*, 12(6):546–550, 2017. 1, 79

[12] Katie A Black, Dimitrios Priftis, Sarah L Perry, Jeremy Yip, William Y Byun, and Matthew Tirrell. Protein encapsulation via polypeptide complex coacervation. *ACS Macro Lett.*, 3(10):1088–1091, 2014. 1, 79

[13] Natassa Pippa, Maria Karayianni, Stergios Pispas, and Costas Demetzos. Complexation of cationic-neutral block polyelectrolyte with insulin and in vitro release studies. *Int. J. Pharm.*, 491(1-2):136–143, 2015.

[14] Antsje Nolles, Adrie H Westphal, Jacob A de Hoop, Remco G Fokkink, J Mieke Kleijn, Willem JH van Berkel, and Jan Willem Borst. Encapsulation of GFP in complex coacervate core micelles. *Biomacromolecules*, 16(5):1542–1549, 2015. 79

[15] Akifumi Kawamura, Atsushi Harada, Kenji Kono, and Kazunori Kataoka. Self-assembled nano-bioreactor from block ionomers with elevated and stabilized enzymatic function. *Bioconjugate Chem.*, 18(5):1555–1559, 2007. 79

[16] Atsushi Harada and Kazunori Kataoka. Pronounced activity of enzymes through the incorporation into the core of polyion complex micelles made from charged block copolymers. *J. Control. Release*, 72(1-3):85–91, 2001. 79

[17] Anthony A Hyman and Kai Simons. Beyond oil and water—phase transitions in cells. *Science*, 337(6098):1047–1049, 2012. 79

[18] Erica A Frankel, Philip C Bevilacqua, and Christine D Keating. Polyamine/nucleotide coacervates provide strong compartmentalization of Mg2+, nucleotides, and RNA. *Langmuir*, 32(8):2041–2049, 2016. 1, 79

[19] Jacob N Israelachvili. *Intermolecular and surface forces*. Academic press, 2011. 1, 104, 105

[20] Jan CT Eijkel and Albert van den Berg. Nanofluidics: what is it and what can we expect from it? *Microfluid. Nanofluid.*, 1:249–267, 2005. 1

[21] Reto B Schoch, Jongyoon Han, and Philippe Renaud. Transport phenomena in nanofluidics. *Rev. Mod. Phys.*, 80(3):839, 2008.

[22] Stefan Howorka and Zuzanna Siwy. Nanopores and nanochannels: from gene sequencing to genome mapping. *ACS Nano*, 10(11):9768–9771, 2016. 6, 79

[23] Andre K Geim and Irina V Grigorieva. Van der waals heterostructures. *Nature*, 499(7459):419–425, 2013. 2, 45

[24] Kostya S Novoselov, Da Jiang, F Schedin, TJ Booth, VV Khotkevich, SV Morozov, and Andre K Geim. Two-dimensional atomic crystals. *Proc. Natl. Acad. Sci. U.S.A.*, 102(30):10451–10453, 2005. 1

[25] Walter Drost-Hansen. Structure of water near solid interfaces. *Ind. Eng. Chem.*, 61(11):10–47, 1969. 1

[26] David Chandler. Interfaces and the driving force of hydrophobic assembly. *Nature*, 437(7059):640–647, 2005. 1

[27] J Faeder and BM Ladanyi. Molecular dynamics simulations of the interior of aqueous reverse micelles. *J. Phys. Chem. B*, 104(5):1033–1046, 2000.

[28] Carlos F Lopez, Steve O Nielsen, Michael L Klein, and Preston B Moore. Hydrogen bonding structure and dynamics of water at the dimyristoylphosphatidylcholine lipid bilayer surface from a molecular dynamics simulation. *J. Phys. Chem. B*, 108(21):6603–6610, 2004.

[29] Cristina Colosi, Marco Costantini, Andrea Barbetta, Cesare Cametti, and Mariella Dentini. Anomalous debye-like dielectric relaxation of water in micro-sized confined polymeric systems. *Phys. Chem. Chem. Phys.*, 15(46):20153–20160, 2013.

[30] MF Reedijk, J Arsic, FFA Hollander, SA De Vries, and E Vlieg. Liquid order at the interface of kdp crystals with water: evidence for icelike layers. *Phys. Rev. Lett.*, 90(6):066103, 2003.

[31] Weiduo Zhu, Yingying Huang, Chongqin Zhu, Hong-Hui Wu, Lu Wang, Jaeil Bai, Jinlong Yang, Joseph S Francisco, Jijun Zhao, Lan-Feng Yuan, et al. Room temperature electrofreezing of water yields a missing dense ice phase in the phase diagram. *Nat. Commun.*, 10(1):1925, 2019.

[32] So Toxvaerd et al. The structure and thermodynamics of a solid–fluid interface. *J. Chem. Phys.*, 74(3):1998–2005, 1981.

[33] Karl P Travis, BD Todd, and Denis J Evans. Departure from navier-stokes hydrodynamics in confined liquids. *Phys. Rev. E*, 55(4):4288, 1997. 1

[34] Sarah J Haigh, Ali Gholinia, Rashid Jalil, Simon Romani, Liam Britnell, Daniel C Elias, Konstantin S Novoselov, Leonid A Ponomarenko, Andre K Geim, and R Gorbachev. Cross-sectional imaging of individual layers and buried interfaces of graphene-based heterostructures and superlattices. *Nat. Mater.*, 11(9):764–767, 2012. 2, 45

[35] Alexander A Balandin, Suchismita Ghosh, Wenzhong Bao, Irene Calizo, Desalegne Teweldebrhan, Feng Miao, and Chun Ning Lau. Superior thermal conductivity of single-layer graphene. *Nano Lett.*, 8(3):902–907, 2008. 2

[36] Alexander A Balandin. Thermal properties of graphene and nanostructured carbon materials. *Nat. Mater.*, 10(8):569–581, 2011.

[37] Changgu Lee, Xiaoding Wei, Jeffrey W Kysar, and James Hone. Measurement of the elastic properties and intrinsic strength of monolayer graphene. *Science*, 321(5887):385–388, 2008. 3, 4, 35

[38] Kostya S Novoselov, Andre K Geim, Sergei V Morozov, De-eng Jiang, Yanshui Zhang, Sergey V Dubonos, Irina V Grigorieva, and Alexandr A Firsov. Electric field effect in atomically thin carbon films. *Science*, 306(5696):666–669, 2004.

[39] Yuanbo Zhang, Yan-Wen Tan, Horst L Stormer, and Philip Kim. Experimental observation of the quantum hall effect and berry's phase in graphene. *Nature*, 438(7065):201–204, 2005.

[40] Rahul Raveendran Nair, Peter Blake, Alexander N Grigorenko, Konstantin S Novoselov, Tim J Booth, Tobias Stauber, Nuno MR Peres, and Andre K Geim. Fine structure constant defines visual transparency of graphene. *Science*, 320(5881):1308–1308, 2008. 2

[41] Andrey V Kretinin, Yuan Cao, Jhih-Sian Tu, GL Yu, Rashid Jalil, Konstantin S Novoselov, Sarah J Haigh, Ali Gholinia, Artem Mishchenko, Marcelo Lozada, et al. Electronic properties of graphene encapsulated with different two-dimensional atomic crystals. *Nano Lett.*, 14(6):3270–3276, 2014. 2

[42] RR Nair, HA Wu, PN Jayaram, IV Grigorieva, and AK Geim. Unimpeded permeation of water through helium-leak–tight graphene-based membranes. *Science*, 335(6067):442–444, 2012. 3, 45

[43] Jason K Holt, Hyung Gyu Park, Yinmin Wang, Michael Stadermann, Alexander B Artyukhin, Costas P Grigoropoulos, Aleksandr Noy, and Olgica Bakajin. Fast mass transport through sub-2-nanometer carbon nanotubes. *Science*, 312(5776):1034–1037, 2006. 45

[44] Alexander I Kolesnikov, Jean-Marc Zanotti, Chun-Keung Loong, Pappannan Thiyagarajan, Alexander P Moravsky, Raouf O Loutfy, and Christian J Burnham. Anomalously soft dynamics of water in a nanotube: a revelation of nanoscale confinement. *Phys. Rev. Lett.*, 93(3):035503, 2004. 3

[45] Jong Min Yuk, Jungwon Park, Peter Ercius, Kwanpyo Kim, Daniel J Hellebusch, Michael F Crommie, Jeong Yong Lee, A Zettl, and A Paul Alivisatos. High-resolution em of colloidal nanocrystal growth using graphene liquid cells. *Science*, 336(6077):61–64, 2012. 3, 45

[46] Jungwon Park, Hyesung Park, Peter Ercius, Adrian F Pegoraro, Chen Xu, Jin Woong Kim, Sang Hoon Han, and David A Weitz. Direct observation of wet biological samples by graphene liquid cell transmission electron microscopy. *Nano Lett.*, 15(7):4737–4744, 2015. 45

[47] Michal Wojcik, Margaret Hauser, Wan Li, Seonah Moon, and Ke Xu. Graphene-enabled electron microscopy and correlated super-resolution microscopy of wet cells. *Nat. Commun.*, 6(1):7384, 2015.

[48] KS Vasu, E Prestat, J Abraham, J Dix, RJ Kashtiban, J Beheshtian, J Sloan, P Carbone, M Neek-Amal, SJ Haigh, et al. Van der waals pressure and its effect on trapped interlayer molecules. *Nat. Commun.*, 7:12168, 2016. 3, 35

[49] G Algara-Siller, O Lehtinen, FC Wang, Rahul Raveendran Nair, U Kaiser, HA Wu, Andre K Geim, and Irina V Grigorieva. Square ice in graphene nanocapillaries. *Nature*, 519(7544):443–445, 2015. 3, 45

[50] Ke Xu, Peigen Cao, and James R Heath. Graphene visualizes the first water adlayers on mica at ambient conditions. *Science*, 329(5996):1188–1191, 2010. 3, 45

[51] Candy Haley Yi Xuan Lim, Anastassia Sorkin, Qiaoliang Bao, Ang Li, Kai Zhang, Milos Nesladek, and Kian Ping Loh. A hydrothermal anvil made of graphene nanobubbles on diamond. *Nat. Commun.*, 4(1):1556, 2013. 3

[52] E Khestanova, F Guinea, L Fumagalli, AK Geim, and IV Grigorieva. Universal shape and pressure inside bubbles appearing in van der waals heterostructures. *Nat. Commun.*, 7(1):12587, 2016. 3, 4, 35, 36, 38, 40, 45, 47, 48, 59, 65, 66, 68

[53] Elena Blundo, Tanju Yildirim, Giorgio Pettinari, and Antonio Polimeni. Experimental adhesion energy in van der waals crystals and heterostructures from atomically thin bubbles. *Phys. Rev. Lett.*, 127(4):046101, 2021. 3, 65

[54] Stephen Timoshenko, Sergius Woinowsky-Krieger, et al. *Theory of plates and shells*, volume 2. McGraw-hill New York, 1959. 3

[55] Kaimin Yue, Wei Gao, Rui Huang, and Kenneth M Liechti. Analytical methods for the mechanics of graphene bubbles. *J. Appl. Phys.*, 112(8), 2012. 3

[56] Renan Villarreal, Pin-Cheng Lin, Fahim Faraji, Nasim Hassani, Harsh Bana, Zviadi Zarkua, Maya N Nair, Hung-Chieh Tsai, Manuel Auge, Felix Junge, et al. Breakdown of universal scaling for nanometer-sized bubbles in graphene. *Nano Lett.*, 21(19):8103–8110, 2021. 4, 43, 47, 48, 66

[57] M Neek-Amal and FM Peeters. Nanoindentation of a circular sheet of bilayer graphene. *Phys. Rev. B*, 81(23):235421, 2010. 4, 65

[58] William S Klug, Robijn F Bruinsma, Jean-Philippe Michel, Charles M Knobler, Irena L Ivanovska, Christoph F Schmidt, and Gijs JL Wuite. Failure of viral shells. *Phys. Rev. Lett.*, 97(22):228101, 2006. 5, 52

[59] Fahim Faraji, Mehdi Neek-Amal, Erik C Neyts, and François M Peeters. Indentation of graphene nano-bubbles. *Nanoscale*, 14(15):5876–5883, 2022. 5, 65, 68, 73, 110

[60] Wayne Yang, Boya Radha, Adnan Choudhary, Yi You, Gangaiah Mettela, Andre K Geim, Aleksei Aksimentiev, Ashok Keerthi, and Cees Dekker. Translocation of DNA through ultrathin nanoslits. *Adv. Mater.*, 33(11):2007682, 2021. 6, 79

[61] Stephanie J Heerema and Cees Dekker. Graphene nanodevices for DNA sequencing. *Nat. Nanotechnol.*, 11(2):127–136, 2016. 79

[62] John J Kasianowicz and Sergey M Bezrukov. On 'three decades of nanopore sequencing'. *Nat. Biotechnol.*, 34(5):481–482, 2016.

[63] Fredrik Persson and Jonas O Tegenfeldt. DNA in nanochannels—directly visualizing genomic information. *Chem. Soc. Rev.*, 39(3):985–999, 2010. 6, 79

[64] Stefan W Kowalczyk, David B Wells, Aleksei Aksimentiev, and Cees Dekker. Slowing down dna translocation through a nanopore in lithium chloride. *Nano Lett.*, 12(2):1038–1044, 2012. 6, 7, 82, 84, 89

[65] Fahim Faraji, Mehdi Neek-Amal, Erik C Neyts, and François M Peeters. Cation-controlled permeation of charged polymers through nanocapillaries. *Phys. Rev. E*, 107(3):034501, 2023. 6

[66] David H Herce, Lalith Perera, Thomas A Darden, and Celeste Sagui. Surface solvation for an ion in a water cluster. *J. Chem. Phys.*, 122(2):024513, 2005. 7, 89, 90, 91

[67] Carl Caleman, Jochen S Hub, Paul J van Maaren, and David van der Spoel. Atomistic simulation of ion solvation in water explains surface preference of halides. *Proc. Natl. Acad. Sci. U.S.A.*, 108(17):6838–6842, 2011. 81, 89, 90, 91

[68] Steven J Stuart and BJ Berne. Effects of polarizability on the hydration of the chloride ion. *J. Phys. Chem.*, 100(29):11934–11943, 1996. 90

[69] Liem X Dang. Computational study of ion binding to the liquid interface of water. *J. Phys. Chem. B*, 106(40):10388–10394, 2002. 7, 90

[70] Qian Yang, PZ Sun, Laura Fumagalli, YV Stebunov, SJ Haigh, ZW Zhou, IV Grigorieva, FC Wang, and AK Geim. Capillary condensation under atomic-scale confinement. *Nature*, 588(7837):250–253, 2020. 8, 100, 101, 102, 105, 107

[71] Joost W Van Honschoten, Nataliya Brunets, and Niels R Tas. Capillarity at the nanoscale. *Chem. Soc. Rev.*, 39(3):1096–1114, 2010. 8, 100

[72] LR Fisher and JN Israelachvili. Determination of the capillary pressure in menisci of molecular dimensions. *Chem. Phys. Lett.*, 76(2):325–328, 1980. 8

[73] C Mathew Mate. Taking a fresh look at disjoining pressure of lubricants at slider-disk interfaces. *IEEE Trans. Magn.*, 47(1):124–130, 2010. 9, 104

[74] Zhenbin Ge, David G Cahill, and Paul V Braun. Thermal conductance of hydrophilic and hydrophobic interfaces. *Phys. Rev. Lett.*, 96(18):186101, 2006. 9

[75] Natalia Shenogina, Rahul Godawat, Pawel Keblinski, and Shekhar Garde. How wetting and adhesion affect thermal conductance of a range of hydrophobic to hydrophilic aqueous interfaces. *Phys. Rev. Lett.*, 102(15):156101, 2009. 9, 108

[76] Deepak Kumar, Thomas P Russell, Benny Davidovitch, and Narayanan Menon. Stresses in thin sheets at fluid interfaces. *Nat. Mater.*, 19(7):690–693, 2020. 9, 119

[77] Ro Shuttleworth. The surface tension of solids. *Proc. Phys. Soc. Sect. A*, 63(5):444, 1950. 9, 117

[78] Harald Ibach. The role of surface stress in reconstruction, epitaxial growth and stabilization of mesoscopic structures. *Surf. Sci. Rep.*, 29(5-6):195–263, 1997. 9, 117

[79] Anatoli Ivanovich Rusanov. Surface thermodynamics revisited. *Surf. Sci. Rep.*, 58(5-8):111–239, 2005.

[80] Dominik Kramer and Jörg Weissmüller. A note on surface stress and surface tension and their interrelation via shuttleworth's equation and the lippmann equation. *Surf. Sci.*, 601(14):3042–3051, 2007. 117, 118, 119

[81] Franz Dieter Fischer, Thomas Waitz, Dieter Vollath, and Narendra K Simha. On the role of surface energy and surface stress in phase-transforming nanoparticles. *Prog. Mater. Sci.*, 53(3):481–527, 2008.

[82] Jan Christer Eriksson. Thermodynamics of surface phase systems: V. contribution to the thermodynamics of the solid-gas interface. *Surf. Sci.*, 14(1):221–246, 1969. 9, 117

[83] EM Gutman. On the thermodynamic definition of surface stress. *J. Phys. Condens. Matter*, 7(48):L663, 1995. 9, 117, 118, 119

[84] DJ Bottomley and T Ogino. Alternative to the shuttleworth formulation of solid surface stress. *Phys. Rev. B*, 63(16):165412, 2001.

[85] DJ Bottomley, Lasse Makkonen, and Kari Kolari. Incompatibility of the shuttleworth equation with hermann's mathematical structure of thermodynamics. *Surf. Sci.*, 603(1):97–101, 2009. 119

[86] Lasse Makkonen. The gibbs- thomson equation and the solid- liquid interface. *Langmuir*, 18(4):1445–1448, 2002.

[87] G Láng and KE Heusler. Can the internal energy function of solid interfaces be of a non-homogeneous nature? *J. Electroanal. Chem.*, 472(2):168–173, 1999. 119

[88] VA Marichev. The shuttleworth equation: Its modifications and current state. *Protect. Met. Phys. Chem. Surf.*, 47(1):25–30, 2011. 9, 117

[89] Colin R Groom, Ian J Bruno, Matthew P Lightfoot, and Suzanna C Ward. The cambridge structural database. *Acta Cryst. B*, 72(2):171–179, 2016. 16

[90] Guenter Bergerhoff, R Hundt, R Sievers, and ID Brown. The inorganic crystal structure data base. *J. Chem. Inf. Comput. Sci.*, 23(2):66–69, 1983. 16

[91] Protein Data Bank. Protein data bank. *Nat. New Biol.*, 233(223):10–1038, 1971. 16

[92] Mark E Tuckerman. *Statistical mechanics: theory and molecular simulation*. Oxford University Press: New York, 2010. 26, 27, 29

[93] Christophe Chipot and Andrew Pohorille. *Free energy calculations*, volume 86. Springer, 2007. 29

[94] Fernando Martín Boubeta, Rocío María Contestín García, Ezequiel Norberto Lorenzo, Leonardo Boechi, Dario Estrin, Mariela Sued, and Mehrnoosh Arrar. Lessons learned about steered molecular dynamics simulations and free energy calculations. *Chem. Biol. Drug Des.*, 93(6):1129–1138, 2019. 30

[95] Gwan-Hyoung Lee, Ryan C Cooper, Sung Joo An, Sunwoo Lee, Arend Van Der Zande, Nicholas Petrone, Alexandra G Hammerberg, Changgu Lee, Bryan Crawford, Warren Oliver, et al. High-strength chemical-vapor–deposited graphene and grain boundaries. *Science*, 340(6136):1073–1076, 2013. 35

[96] Giovanni Zamborlini, Mighfar Imam, Laerte L Patera, Tevfik Onur Mentes, Natasa Stojic, Cristina Africh, Alessandro Sala, Nadia Binggeli, Giovanni Comelli, and Andrea Locatelli. Nanobubbles at gpa pressure under graphene. *Nano Lett.*, 15(9):6162–6169, 2015. 35, 36, 59

[97] Rosanna Larciprete, Stefano Colonna, Fabio Ronci, Roberto Flammini, Paolo Lacovig, Nicoleta Apostol, Antonio Politano, Peter Feulner, Dietrich Menzel, and Silvano Lizzit. Self-assembly of graphene nanoblisters sealed to a bare metal surface. *Nano Lett.*, 16(3):1808–1817, 2016.

[98] H Ghorbanfekr-Kalashami, KS Vasu, RR Nair, François M Peeters, and M Neek-Amal. Dependence of the shape of graphene nanobubbles on trapped substance. *Nat. Commun.*, 8(1):15844, 2017. 35, 36, 41, 42, 45

[99] Candy Haley Yi Xuan Lim, Milos Nesladek, and Kian Ping Loh. Observing high-pressure chemistry in graphene bubbles. *Angew. Chem.*, 53(1):215–219, 2014. 35

[100] Zenan Qi, Alexander L Kitt, Harold S Park, Vitor M Pereira, David K Campbell, and AH Castro Neto. Pseudomagnetic fields in graphene nanobubbles of constrained geometry: A molecular dynamics study. *Phys. Rev. B: Condens. Matter Mater. Phys.*, 90(12):125419, 2014. 35

[101] N Levy, SA Burke, KL Meaker, M Panlasigui, A Zettl, F Guinea, AH Castro Neto, and Michael F Crommie. Strain-induced pseudo–magnetic fields greater than 300 tesla in graphene nanobubbles. *Science*, 329(5991):544–547, 2010.

[102] Pengfei Jia, Wenjing Chen, Jiabin Qiao, Miao Zhang, Xiaohu Zheng, Zhongying Xue, Rongda Liang, Chuanshan Tian, Lin He, Zengfeng Di, et al. Programmable graphene nanobubbles with three-fold symmetric pseudo-magnetic fields. *Nat. Commun.*, 10(1):3127, 2019. 35

[103] Christian Carmesin, Michael Lorke, Matthias Florian, Daniel Erben, Alexander Schulz, Tim O Wehling, and Frank Jahnke. Quantum-dot-like states in molybdenum disulfide nanostructures due to the interplay of local surface wrinkling, strain, and dielectric confinement. *Nano Lett.*, 19(5):3182–3186, 2019. 35

[104] Yi-Tao Wang, Wei Liu, Zhi-Peng Li, Shang Yu, Zhi-Jin Ke, Yu Meng, Jian-Shun Tang, Chuan-Feng Li, and Guang-Can Guo. A bubble-induced ultrastable and robust single-photon emitter in hexagonal boron nitride. *arXiv preprint arXiv:1906.00493*, 2019. 35

[105] Charlotte Herbig, E Harriet Åhlgren, Ulrike A Schröder, Antonio J Martinez-Galera, Mohammad A Arman, Jani Kotakoski, Jan Knudsen, Arkady V Krasheninnikov, and Thomas Michely. Xe irradiation of graphene on ir (111): From trapping to blistering. *Phys. Rev. B: Condens. Matter Mater. Phys.*, 92(8):085429, 2015. 36

[106] Hyo Won Kim, Wonhee Ko, JiYeon Ku, Insu Jeon, Donggyu Kim, Hyeokshin Kwon, Youngtek Oh, Seunghwa Ryu, Young Kuk, Sung Woo Hwang, et al. Nanoscale control of phonon excitations in graphene. *Nat. Commun.*, 6(1):7528, 2015. 36

[107] Ken Verguts, Yves Defossez, Alessandra Leonhardt, Joke De Messemaeker, Koen Schouteden, Chris Van Haesendonck, Cedric Huyghebaert, Stefan De Gendt, and Steven Brems. Growth of millimeter-sized graphene single crystals on al_2o_3(0001)/pt(111) template wafers using chemical vapor deposition. *ECS J. Solid State Sci. Technol.*, 7(12), 2018. M195. 36

[108] Ken Verguts, Nandi Vrancken, Bart Vermeulen, Cedric Huyghebaert, Herman Terryn, Steven Brems, and Stefan De Gendt. Single-layer graphene synthesis on a al_2o_3(0001)/cu(111) template using chemical vapor deposition. *ECS J. Solid State Sci. Technol.*, 5(11), 2016. Q3060. 36

[109] U Bangert, William Pierce, DM Kepaptsoglou, Q Ramasse, R Zan, MH Gass, JA Van den Berg, CB Boothroyd, J Amani, and H Hofsäss. Ion implantation of graphene - toward ic compatible technologies. *Nano Lett.*, 13(10):4902–4907, 2013. 36

[110] Demie Kepaptsoglou, Trevor P Hardcastle, Che R Seabourne, Ursel Bangert, Recep Zan, Julian Alexander Amani, Hans Hofsäss, Rebecca J Nicholls, Rik M D Brydson, Andrew J Scott, et al. Electronic structure modification of ion implanted graphene: the spectroscopic signatures of p-and n-type doping. *ACS Nano*, 9(11):11398–11407, 2015.

[111] Philip Willke, Julian A Amani, Anna Sinterhauf, Sangeeta Thakur, Thomas Kotzott, Thomas Druga, Steffen Weikert, Kalobaran Maiti, Hans Hofsäss, and Martin Wenderoth. Doping of graphene by low-energy ion beam implantation: structural, electronic, and transport properties. *Nano Lett.*, 15(8):5110–5115, 2015. 36

[112] Jürgen Vogt and Santiago Alvarez. van der waals radii of noble gases. *Inorg. Chem.*, 53(17):9260–9266, 2014. 39

[113] Jorge Torres, Yisi Zhu, Pei Liu, Seong Chu Lim, and Minhee Yun. Adhesion energies of 2d graphene and mos2 to silicon and metal substrates. *Phys. Status Solidi*, 215(1):1700512, 2018. 40, 42

[114] Jörg Weissmüller and JW Cahn. Mean stresses in microstructures due to interface stresses: A generalization of a capillary equation for solids. *Acta Mater.*, 45(5):1899–1906, 1997. 41, 62

[115] DH Tsai. The virial theorem and stress calculation in molecular dynamics. *J. Chem. Phys.*, 70(3):1375–1382, 1979. 41, 43, 59, 60

[116] Taeshik Yoon, Woo Cheol Shin, Taek Yong Kim, Jeong Hun Mun, Taek-Soo Kim, and Byung Jin Cho. Direct measurement of adhesion energy of monolayer graphene as-grown on copper and its application to renewable transfer process. *Nano Lett.*, 12(3):1448–1452, 2012. 42

[117] Steven J Stuart, Alan B Tutein, and Judith A Harrison. A reactive potential for hydrocarbons with intermolecular interactions. *J. Chem. Phys.*, 112(14):6472–6486, 2000. 43, 46, 108

[118] Murray S Daw and Michael I Baskes. Semiempirical, quantum mechanical calculation of hydrogen embrittlement in metals. *Phys. Rev. Lett.*, 50(17):1285–1288, 1983. 43

[119] H Hippler, J Troe, and HJ Wendelken. Collisional deactivation of vibrationally highly excited polyatomic molecules. ii. direct observations for excited toluene. *J. Chem. Phys.*, 78(11):6709–6717, 1983. 43, 47

[120] Louis A Girifalco, Miroslav Hodak, and Roland S Lee. Carbon nanotubes, buckyballs, ropes, and a universal graphitic potential. *Phys. Rev. B: Condens. Matter Mater. Phys.*, 62(19):13104, 2000. 43, 47, 82

[121] T Halicioğlu and GM Pound. Calculation of potential energy parameters form crystalline state properties. *Phys. Status Solidi A*, 30(2):619–623, 1975. 43, 47

[122] Chang Lyoul Kong. Combining rules for intermolecular potential parameters. ii. rules for the lennard-jones (12–6) potential and the morse potential. *J. Chem. Phys.*, 59(5):2464–2467, 1973. 43

[123] Steve Plimpton. Fast parallel algorithms for short-range molecular dynamics. *J. Comput. Phys.*, 117(1):1–19, 1995. 43, 47, 68, 80

[124] Markus Arnoldi, Monika Fritz, Edmund Bäuerlein, Manfred Radmacher, Erich Sackmann, and Alexei Boulbitch. Bacterial turgor pressure can be measured by atomic force microscopy. *Phys. Rev. E*, 62(1):1034, 2000. 45

[125] Murray S Daw and Michael I Baskes. Embedded-atom method: Derivation and application to impurities, surfaces, and other defects in metals. *Phys. Rev. B*, 29(12):6443, 1984. 46

[126] Zhonghua Ni, Hao Bu, Min Zou, Hong Yi, Kedong Bi, and Yunfei Chen. Anisotropic mechanical properties of graphene sheets from molecular dynamics. *Phys. B Condens. Matter*, 405(5):1301–1306, 2010. 46

[127] OA Shenderova, DW Brenner, A Omeltchenko, X Su, and LH Yang. Atomistic modeling of the fracture of polycrystalline diamond. *Phys. Rev. B*, 61(6):3877, 2000. 46

[128] KGS Dilrukshi, MAN Dewapriya, and UGA Puswewala. Size dependency and potential field influence on deriving mechanical properties of carbon nanotubes using molecular dynamics. *Theor. Appl. Mech. Lett.*, 5(4):167–172, 2015. 46

[129] MAN Dewapriya, A Srikantha Phani, and RKND Rajapakse. Influence of temperature and free edges on the mechanical properties of graphene. *Model. Simul. Mater. Sci. Eng.*, 21(6):065017, 2013. 46

[130] Bei Peng, Mark Locascio, Peter Zapol, Shuyou Li, Steven L Mielke, George C Schatz, and Horacio D Espinosa. Measurements of near-ultimate strength for multiwalled carbon nanotubes and irradiation-induced crosslinking improvements. *Nat. Nanotechnol.*, 3(10):626–631, 2008. 46

[131] Magnus Rudolph Hestenes, Eduard Stiefel, et al. *Methods of conjugate gradients for solving linear systems*, volume 49. NBS Washington, DC, 1952. 47

[132] Teng Zhang, Xiaoyan Li, and Huajian Gao. Fracture of graphene: a review. *Int. J. Fract.*, 196(1):1–31, 2015. 47

[133] Alexander Stukowski. Visualization and analysis of atomistic simulation data with ovito–the open visualization tool. *Model. Simul. Mater. Sci. Eng.*, 18(1):015012, 2009. 47, 81

[134] WH Roos, R Bruinsma, and GJL Wuite. Physical virology. *Nat. Phys.*, 6(10):733–743, 2010. 52

[135] Lev Davidovich Landau and Evgenii Mikhailovich Lifshits. *Theory of Elasticity*. Pergamon Press, 1964. 52

[136] Annalisa Fasolino, JH Los, and Mikhail I Katsnelson. Intrinsic ripples in graphene. *Nat. Mater.*, 6(11):858–861, 2007. 53

[137] P Liu and YW Zhang. Temperature-dependent bending rigidity of graphene. *Appl. Phys. Lett.*, 94(23):231912, 2009.

[138] Lijun Yi. Temperature dependence bending rigidity of 2d membranes: Graphene as an example. *AIP Adv.*, 8(7):075104, 2018. 53

[139] Huijuan Zhao and NR Aluru. Temperature and strain-rate dependent fracture strength of graphene. *J. Appl. Phys.*, 108(6):064321, 2010. 53

[140] Dominic Vella, Amin Ajdari, Ashkan Vaziri, and Arezki Boudaoud. The indentation of pressurized elastic shells: from polymeric capsules to yeast cells. *J. R. Soc. Interface*, 9(68):448–455, 2012. 59

[141] Frédéric Datchi, Paul Loubeyre, and René LeToullec. Extended and accurate determination of the melting curves of argon, helium, ice (h 2 o), and hydrogen (h 2). *Phys. Rev. B*, 61(10):6535, 2000. 63

[142] Jan Solca, Anthony J Dyson, Gerold Steinebrunner, Barbara Kirchner, and Hanspeter Huber. Melting curves for neon calculated from pure theory. *J. Chem. Phys.*, 108(10):4107–4111, 1998. 63

[143] Ethan A Mastny and Juan J de Pablo. Melting line of the lennard-jones system, infinite size, and full potential. *J. Chem. Phys.*, 127(10):104504, 2007. 64

[144] Cinzia Di Giorgio, Elena Blundo, Giorgio Pettinari, Marco Felici, Yuerui Lu, Anna Maria Cucolo, Antonio Polimeni, and Fabrizio Bobba. Nanoscale measurements of elastic properties and hydrostatic pressure in h2-bulged mos2 membranes. *Adv. Mater. Interfaces*, 7(23):2001024, 2020. 65

[145] Binyu Zhao, Yang Song, Shuo Wang, Bin Dai, Lijuan Zhang, Yaming Dong, Junhong Lü, and Jun Hu. Mechanical mapping of nanobubbles by peakforce atomic force microscopy. *Soft Matter*, 9(37):8837–8843, 2013.

[146] Hideaki Teshima, Hiroki Kusudo, Carlos Bistafa, and Yasutaka Yamaguchi. Quantifying interfacial tensions of surface nanobubbles: How far can young's equation explain? *Nanoscale*, 14(6):2446–2455, 2022. 65

[147] Xing Chen, Peng Wu, Michael Rousseas, David Okawa, Zev Gartner, Alex Zettl, and Carolyn R Bertozzi. Boron nitride nanotubes are noncytotoxic and can be functionalized for interaction with proteins and cells. *J. Am. Chem. Soc.*, 131(3):890–891, 2009. 65

[148] Chunyi Zhi, Yoshio Bando, Chengchun Tang, and Dmitri Golberg. Boron nitride nanotubes. *Mater. Sci. Eng. R Rep.*, 70(3-6):92–111, 2010.

[149] X Blase, Angel Rubio, Steven G Louie, and Marvin L Cohen. Stability and band gap constancy of boron nitride nanotubes. *Europhys. Lett.*, 28(5):335, 1994. 65

[150] Sobin Alosious, Sridhar Kumar Kannam, Sarith P Sathian, and BD Todd. Effects of electrostatic interactions on kapitza resistance in hexagonal boron nitride–water interfaces. *Langmuir*, 38(29):8783–8793, 2022. 66

[151] Chang Y Won and NR Aluru. Water permeation through a subnanometer boron nitride nanotube. *J. Am. Chem. Soc.*, 129(10):2748–2749, 2007.

[152] Chang Y Won and NR Aluru. Structure and dynamics of water confined in a boron nitride nanotube. *J. Phys. Chem. C*, 112(6):1812–1818, 2008.

[153] Levan Chkhartishvili, Dekanosidze Sh, Nodar Maisuradze, Manana Beridze, and Ramaz Esiava. stimation of atomic charges in boron nitrides. *East.-Eur. J. Enterp. Technol.*, 3(5 (75)):50–57, 2015.

[154] Tamsyn A Hilder, Rui Yang, V Ganesh, Dan Gordon, Andrey Bliznyuk, Alistair P Rendell, and S-H Chung. Validity of current force fields for simulations on boron nitride nanotubes. *Micro Nano Lett.*, 5(2):150–156, 2010. 66

[155] William L Jorgensen, Jeffry D Madura, and Carol J Swenson. Optimized intermolecular potential functions for liquid hydrocarbons. *J. Am. Chem. Soc.*, 106(22):6638–6646, 1984. 68, 80, 82

[156] L Lindsay and DA Broido. Optimized tersoff and brenner empirical potential parameters for lattice dynamics and phonon thermal transport in carbon nanotubes and graphene. *Phys. Rev. B*, 81(20):205441, 2010. 68, 108

[157] Anitha Kommu and Jayant K Singh. Separation of ethanol and water using graphene and hexagonal boron nitride slit pores: A molecular dynamics study. *J. Phys. Chem. C*, 121(14):7867–7880, 2017. 68

[158] R Hockney and J Eastwood. Computer simulations using particles mcgraw-hill. *New York*, Vol. 61, 1981. 68, 80

[159] Dan Qu, Jan S Pedersen, Sebastien Garnier, Andre Laschewsky, Helmuth Möhwald, and Regine v Klitzing. Effect of polymer charge and geometrical confinement on ion distribution and the structuring in semidilute polyelectrolyte solutions: comparison between AFM and SAXS. *Macromolecules*, 39(21):7364–7371, 2006. 79

[160] Joanne N Bright, Mark J Stevens, Jan Hoh, and Thomas B Woolf. Characterizing the function of unstructured proteins: Simulations of charged polymers under confinement. *J. Chem. Phys.*, 115(10):4909–4918, 2001. 79

[161] Grégory F Schneider, Stefan W Kowalczyk, Victor E Calado, Grégory Pandraud, Henny W Zandbergen, Lieven MK Vandersypen, and Cees Dekker. DNA translocation through graphene nanopores. *Nano Lett.*, 10(8):3163–3167, 2010. 80

[162] Arnold J Storm, Cornelis Storm, Jianghua Chen, Henny Zandbergen, Jean-Francois Joanny, and Cees Dekker. Fast DNA translocation through a solid-state nanopore. *Nano Lett.*, 5(7):1193–1197, 2005.

[163] Vladimir V Palyulin, Tapio Ala-Nissila, and Ralf Metzler. Polymer translocation: the first two decades and the recent diversification. *Soft Matter*, 10(45):9016–9037, 2014. 80

[164] M Daoud and PG De Gennes. Statistics of macromolecular solutions trapped in small pores. *J. Phys.*, 38(1):85–93, 1977. 80

[165] Theo Odijk. The statistics and dynamics of confined or entangled stiff polymers. *Macromolecules*, 16(8):1340–1344, 1983. 80

[166] Gerald S Manning. The molecular theory of polyelectrolyte solutions with applications to the electrostatic properties of polynucleotides. *Q. Rev. Biophys.*, 11(2):179–246, 1978. 80

[167] ROBERT WILFRED Wilson, DONALD C Rau, and VICTOR A Bloomfield. Comparison of polyelectrolyte theories of the binding of cations to DNA. *Biophys. J.*, 30(2):317–325, 1980. 80

[168] Jean-Paul Ryckaert, Giovanni Ciccotti, and Herman JC Berendsen. Numerical integration of the cartesian equations of motion of a system with constraints: molecular dynamics of n-alkanes. *J. Comput. Phys.*, 23(3):327–341, 1977. 81

[169] Hans C Andersen. Rattle: A "velocity" version of the shake algorithm for molecular dynamics calculations. *J. Comput. Phys.*, 52(1):24–34, 1983. 81

[170] William Humphrey, Andrew Dalke, and Klaus Schulten. Vmd: visual molecular dynamics. *J. Mol. Graphics*, 14(1):33–38, 1996. 81

[171] Leandro Martínez, Ricardo Andrade, Ernesto G Birgin, and José Mario Martínez. Packmol: a package for building initial configurations for molecular dynamics simulations. *J. Comput. Chem.*, 30(13):2157–2164, 2009. 81

[172] Anna CV Johansson and Erik Lindahl. Position-resolved free energy of solvation for amino acids in lipid membranes from molecular dynamics simulations. *Proteins Struct. Funct. Bioinf.*, 70(4):1332–1344, 2008. 81

[173] Yujie Wu, Harald L Tepper, and Gregory A Voth. Flexible simple point-charge water model with improved liquid-state properties. *J. Chem. Phys.*, 124(2):024503, 2006. 82

[174] T Werder, Jens Honore Walther, RL Jaffe, T Halicioglu, and Petros Koumoutsakos. On the water- carbon interaction for use in molecular dynamics simulations of graphite and carbon nanotubes. *J. Phys. Chem. B*, 107(6):1345–1352, 2003. 82, 110

[175] Snehasis Chowdhuri and Amalendu Chandra. Hydration structure and diffusion of ions in supercooled water: Ion size effects. *J. Chem. Phys.*, 118(21):9719–9725, 2003. 82

[176] Derek W Smith. Ionic hydration enthalpies. *J. Chem. Educ.*, 54(9):540, 1977. 86

[177] Uri Raviv, Pierre Laurat, and Jacob Klein. Fluidity of water confined to subnanometre films. *Nature*, 413(6851):51–54, 2001. 88

[178] Mehdi Neek-Amal, Francois M Peeters, Irina V Grigorieva, and Andre K Geim. Commensurability effects in viscosity of nanoconfined water. *ACS Nano*, 10(3):3685–3692, 2016. 88

[179] Lalith Perera and Max L Berkowitz. Many-body effects in molecular dynamics simulations of $Na^+(H_2O)_n$ and $Cl^-(H_2O)_n$ clusters. *J. Chem. Phys.*, 95(3):1954–1963, 1991. 89

[180] Lalith Perera and Max L Berkowitz. Structure and dynamics of $Cl^-(H_2O)_{20}$ clusters: The effect of the polarizability and the charge of the ion. *J. Chem. Phys.*, 96(11):8288–8294, 1992. 90

[181] Lalith Perera and Max L Berkowitz. Erratum: Many-body effects in molecular dynamics simulations of $Na^+(H_2O)_n$ and $Cl^-(H_2O)_n$ clusters [J. Chem. Phys. 95, 1954 (1991)]. *J. Chem. Phys.*, 99(5):4236–4237, 1993. 89

[182] Robert Anthony Robinson and Robert Harold Stokes. *electrolyte solutions*. Butterworths Scientific Publications, London, 1959. 89

[183] Ronald Wilfrid Gurney and Ronald W Gurney. *Ionic processes in solution*, volume 5. McGraw-Hill, New York, 1953. 89

[184] HJC Berendsen, JR Grigera, and TP Straatsma. The missing term in effective pair potentials. *J. Phys. Chem.*, 91(24):6269–6271, 1987. 90

[185] You Han, Dandan Jiang, Jinli Zhang, Wei Li, Zhongxue Gan, and Junjie Gu. Development, applications and challenges of ReaxFF reactive force field in molecular simulations. *Front. Chem. Sci. Eng.*, 10(1):16–38, 2016. 90

[186] Thomas P Senftle, Sungwook Hong, Md Mahbubul Islam, Sudhir B Kylasa, Yuanxia Zheng, Yun Kyung Shin, Chad Junkermeier, Roman Engel-Herbert, Michael J Janik, Hasan Metin Aktulga, et al. The ReaxFF reactive force-field: development, applications and future directions. *npj Comput. Mater.*, 2(1):1–14, 2016. 90

[187] Zhongjin He, Haishuai Cui, Shihua Hao, Liping Wang, and Jian Zhou. Electric-field effects on ionic hydration: a molecular dynamics study. *J. Phys. Chem. B*, 122(22):5991–5998, 2018. 91

[188] Sebastien Kerisit, M Vijayakumar, Kee Sung Han, and Karl T Mueller. Solvation structure and transport properties of alkali cations in dimethyl sulfoxide under exogenous static electric fields. *J. Chem. Phys.*, 142(22):224502, 2015. 91

[189] Mark V Fedkin, Yun Kyung Shin, Nabankur Dasgupta, Jejoon Yeon, Weiwei Zhang, Diana Van Duin, Adri CT Van Duin, Kento Mori, Atsushi Fujiwara, Masahiko Machida, et al. Development of the ReaxFF methodology for electrolyte–water systems. *J. Phys. Chem. A*, 123(10):2125–2141, 2019. 91

[190] Anthony K Rappe and William A Goddard III. Charge equilibration for molecular dynamics simulations. *J. Phys. Chem.*, 95(8):3358–3363, 1991. 91

[191] Jason P Koski, Stan G Moore, Raymond C Clay, Kurt A O'Hearn, H Metin Aktulga, Mark A Wilson, Joshua A Rackers, J Matthew D Lane, and Normand A Modine. Water in an external electric field: comparing charge distribution methods using ReaxFF simulations. *J. Chem. Theory Comput.*, 18(1):580–594, 2021. 92

[192] Murugappan Muthukumar. Entropic barrier theory of polymer translocation. In *Structure and Dynamics of Confined Polymers*, pages 227–239. Springer, 2002. 93

[193] Subha Pratihar and Amalendu Chandra. A first principles molecular dynamics study of lithium atom solvation in binary liquid mixture of water and ammonia: Structural, electronic, and dynamical properties. *J. Chem. Phys.*, 134(2):024519, 2011. 95

[194] Johan Mahler and Ingmar Persson. A study of the hydration of the alkali metal ions in aqueous solution. *Inorg. Chem.*, 51(1):425–438, 2012. 95

[195] William Thomson. 4. on the equilibrium of vapour at a curved surface of liquid. *Proc. R. Soc. Edinb.*, 7:63–68, 1872. 100

[196] ND Lisgarten, JR Sambles, and LM Skinner. Vapour pressure over curved surfaces-the kelvin equation. *Contemp. Phys.*, 12(6):575–593, 1971. 100, 104

[197] Elisabeth Charlaix and Matteo Ciccotti. Capillary condensation in confined media. *arXiv preprint arXiv:0910.4626*, 2009. 100

[198] P Weiss. Tired of grinding their gears, micromachine researchers turn to surface science. *SCIENCE NEWS-WASHINGTON-*, 158(4):56–59, 2000.

[199] Roya Maboudian, W Robert Ashurst, and Carlo Carraro. Tribological challenges in micromechanical systems. *Tribol. Lett.*, 12:95–100, 2002. 100

[200] Fereshte Taherian, Valentina Marcon, Nico FA van der Vegt, and Frédéric Leroy. What is the contact angle of water on graphene? *Langmuir*, 29(5):1457–1465, 2013. 102, 110, 112, 113, 115

[201] Hailong Liu and Guoxin Cao. Effectiveness of the young-laplace equation at nanoscale. *Sci. Rep.*, 6(1):1–10, 2016. 103, 110

[202] Shengfeng Cheng and Mark O Robbins. Nanocapillary adhesion between parallel plates. *Langmuir*, 32(31):7788–7795, 2016. 104, 110

[203] KP Galvin. A conceptually simple derivation of the kelvin equation. *Chem. Eng. Sci.*, 60(16):4659–4660, 2005. 104

[204] Je-Luen Li, Jaehun Chun, Ned S Wingreen, Roberto Car, Ilhan A Aksay, and Dudley A Saville. Use of dielectric functions in the theory of dispersion forces. *Phys. Rev. B*, 71(23):235412, 2005. 104

[205] Simon Gravelle, Christophe Ybert, Lydéric Bocquet, and Laurent Joly. Anomalous capillary filling and wettability reversal in nanochannels. *Phys. Rev. E*, 93(3):033123, 2016. 105

[206] Xi Chen, Guoxin Cao, Aijie Han, Venkata K Punyamurtula, Ling Liu, Patricia J Culligan, Taewan Kim, and Yu Qiao. Nanoscale fluid transport: size and rate effects. *Nano Lett.*, 8(9):2988–2992, 2008. 106

[207] BD Todd, Denis J Evans, and Peter J Daivis. Pressure tensor for inhomogeneous fluids. *Phys. Rev. E*, 52(2):1627, 1995. 106

[208] B Radha, Ali Esfandiar, FC Wang, AP Rooney, K Gopinadhan, Ashok Keerthi, Artem Mishchenko, Amritha Janardanan, Peter Blake, Laura Fumagalli, et al. Molecular transport through capillaries made with atomic-scale precision. *Nature*, 538(7624):222–225, 2016. 106, 107, 108, 111

[209] Dmitry Alexeev, Jie Chen, Jens H Walther, Konstantinos P Giapis, Panagiotis Angelikopoulos, and Petros Koumoutsakos. Kapitza resistance between few-layer graphene and water: liquid layering effects. *Nano Lett.*, 15(9):5744–5749, 2015. 107, 108, 110, 111

[210] Sobin Alosious, Sridhar Kumar Kannam, Sarith P Sathian, and BD Todd. Kapitza resistance at water–graphene interfaces. *J. Chem. Phys.*, 152(22):224703, 2020. 107, 108, 110, 111

[211] Christian Sendner, Dominik Horinek, Lyderic Bocquet, and Roland R Netz. Interfacial water at hydrophobic and hydrophilic surfaces: Slip, viscosity, and diffusion. *Langmuir*, 25(18):10768–10781, 2009. 109

[212] Bladimir Ramos-Alvarado, Satish Kumar, and GP Peterson. Solid–liquid thermal transport and its relationship with wettability and the interfacial liquid structure. *The journal of physical chemistry letters*, 7(17):3497–3501, 2016. 109, 111

[213] Frédéric Leroy, Daniel JVA Dos Santos, and Florian Müller-Plathe. Interfacial excess free energies of solid–liquid interfaces by molecular dynamics simulation and thermodynamic integration. *Macromol. Rapid Commun.*, 30(9-10):864–870, 2009. 109, 113, 114, 115

[214] Frédéric Leroy and Florian Müller-Plathe. Solid-liquid surface free energy of lennard-jones liquid on smooth and rough surfaces computed by molecular dynamics using the phantom-wall method. *J. Chem. Phys.*, 133(4):044110, 2010. 109, 113, 114, 115

[215] Pierre-Gilles Gennes, Françoise Brochard-Wyart, David Quéré, et al. *Capillarity and wetting phenomena: drops, bubbles, pearls, waves*. Springer, 2004. 110

[216] ES Machlin. On interfacial tension at a rigid apolar wall–water interface. *Langmuir*, 28(49):16729–16732, 2012. 110

[217] Olga I Vinogradova. Drainage of a thin liquid film confined between hydrophobic surfaces. *Langmuir*, 11(6):2213–2220, 1995. 110, 111

[218] Keliu Wu, Zhangxin Chen, Jing Li, Xiangfang Li, Jinze Xu, and Xiaohu Dong. Wettability effect on nanoconfined water flow. *Proc. Natl. Acad. Sci. U.S.A.*, 114(13):3358–3363, 2017. 110, 111

[219] Bo Hung Kim, Ali Beskok, and Tahir Cagin. Molecular dynamics simulations of thermal resistance at the liquid-solid interface. *J. Chem. Phys.*, 129(17):174701, 2008. 111

[220] Jean-Louis Barrat and François Chiaruttini. Kapitza resistance at the liquid—solid interface. *Mol. Phys.*, 101(11):1605–1610, 2003. 111

[221] Sohail Murad and Ishwar K Puri. Thermal transport across nanoscale solid-fluid interfaces. *Appl. Phys. Lett.*, 92(13), 2008. 111

[222] John G Kirkwood and Frank P Buff. The statistical mechanical theory of surface tension. *J. Chem. Phys.*, 17(3):338–343, 1949. 113

[223] G Navascués and MV Berry. The statistical mechanics of wetting. *Mol. Phys.*, 34(3):649–664, 1977. 114

[224] Ruslan L Davidchack and Brian B Laird. Simulation of the hard-sphere crystal–melt interface. *J. Chem. Phys.*, 108(22):9452–9462, 1998.

[225] J Miyazaki, JA Barker, and GM Pound. A new monte carlo method for calculating surface tension. *J. Chem. Phys.*, 64(8):3364–3369, 1976.

[226] Jeremy Q Broughton and George H Gilmer. Molecular dynamics investigation of the crystal–fluid interface. vi. excess surface free energies of crystal–liquid systems. *J. Chem. Phys.*, 84(10):5759–5768, 1986.

[227] Ruslan L Davidchack and Brian B Laird. Direct calculation of the crystal–melt interfacial free energies for continuous potentials: Application to the lennard-jones system. *J. Chem. Phys.*, 118(16):7651–7657, 2003.

[228] Richard Handel, Ruslan L Davidchack, Jamshed Anwar, and Andrey Brukhno. Direct calculation of solid-liquid interfacial free energy for molecular systems: Tip4p ice-water interface. *Phys. Rev. Lett.*, 100(3):036104, 2008.

[229] Ranjit Bahadur, Lynn M Russell, and Saman Alavi. Surface tensions in nacl- water-air systems from md simulations. *J. Phys. Chem. B*, 111(41):11989–11996, 2007.

[230] Sandeep Pal, Horst Weiss, Harald Keller, and Florian Müller-Plathe. Effect of nanostructure on the properties of water at the water- hydrophobic interface: A molecular dynamics simulation. *Langmuir*, 21(8):3699–3709, 2005. 113

[231] JH Sikkenk, JO Indekeu, JMJ Van Leeuwen, and EO Vossnack. Molecular-dynamics simulation of wetting and drying at solid-fluid interfaces. *Phys. Rev. Lett.*, 59(1):98, 1987. 114

[232] Frédéric Leroy and Florian Müller-Plathe. Rationalization of the behavior of solid-liquid surface free energy of water in cassie and wenzel wetting states on rugged solid surfaces at the nanometer scale. *Langmuir*, 27(2):637–645, 2011. 115

[233] Wai Keong Choong. *The determination of contact angle of water on graphite surface: Using grand canonical transition matrix Monte Carlo*. State University of New York at Buffalo, 2007. 115

[234] Lasse Makkonen. Misinterpretation of the shuttleworth equation. *Scr. Mater.*, 66(9):627–629, 2012. 117

[235] Lev Davidovich Landau, Evgenii Mikhailovich Lifshitz, Arnold Markovich Kosevich, and Lev Petrovich Pitaevskii. *Theory of elasticity: volume 7*, volume 7. Elsevier, 1986. 118

[236] Morton E Gurtin and A Ian Murdoch. Surface stress in solids. *Int. J. Solids Struct.*, 14(6):431–440, 1978. 118

[237] Wilhelm G Wolfer. Elastic properties of surfaces on nanoparticles. *Acta Mater.*, 59(20):7736–7743, 2011. 118

[238] Lasse Makkonen. Misconceptions of the relation between surface energy and surface tension on a solid. *Langmuir*, 30(9):2580–2581, 2014. 119

Curriculum vitæ

Name:
Fahim Faraji
Born:
16/02/1987, Tehran, Iran
Contact:
Campus Groenenborger
Groenenborgerlaan 171
2020 Antwerpen, Belgium
fahim.faraji@uantwerpen.be
fahimfaraji@gmail.com

Education

University of Antwerp, Antwerp, Belgium
(Jan 2020 - present)
PhD, Physcis
Thesis title: The Influence of Confinement on Material Properties and Interfacial Thermodynamics

University of Tehran, Tehran, Iran
(Sep 2010 - Nov 2012)
MSc, Mechanical Engineering, Thermal science
Thesis title: Fluid transport by symmetric temperature gradient along the walls in a composite nanochannel: a non-equilibrium molecular dynamics study.

University of Tehran, Tehran, Iran
(Sep 2005 - Sep 2010)
BSc, Mechanical Engineering
Thesis title: Themodynamics study of heat recovery steam generators

Publications related to this thesis

1) **Fahim Faraji**, Erik C. Neyts, Milorad V. Milošević, François M. Peeters, Comment on "Misinterpretation of the Shuttleworth equation". Scripta Materialia **250**, 116186 (2024).

2) **Fahim Faraji**, Erik C. Neyts, Milorad V. Milošević, François M. Peeters, Capillary condensation of water in graphene nanocapillaries. Nano Letters **24**, 18, 5625–5630, (2024).

3) **Fahim Faraji**, Mehdi Neek-Amal, Erik C. Neyts, François M. Peeters, Cation-controlled permeation of charged polymers through nanocapillaries. Physical Review E **107**, 034501 (2023).

4) **Fahim Faraji**, Mehdi Neek-Amal, Erik C. Neyts, François M. Peeters, Indentation of graphene nano-bubbles. Nanoscale **14**, 5876–5883 (2022).

5) Renan Villarreal, Pin-Cheng Lin, **Fahim Faraji**, et al. Breakdown of universal scaling for nanometer-sized bubbles in graphene. Nano Letters **21**, 8103–8110 (2021).

Other publications

1) Zohreh Javdani, Nassim Hassani, **Fahim Faraji**, et al., Clogging and Unclogging of Hydrocarbon-Contaminated Nanochannels. The Journal of Physical Chemistry Letters **13**, 11454–11463 (2022).

2) **Fahim Faraji**, Ali Rajabpour, Fluid heating in a nano-scale Poiseuille flow: A non-equilibrium molecular dynamics study. Current Applied Physics **12**, 1646-1654 (2017).

3) **Fahim Faraji**, Ali Rajabpour, Temperature gradient-induced fluid pumping inside a single-wall carbon nanotube: A non-equilibrium molecular dynamics study. Physics of Fluids 28, 092004 (2016).

4) **Fahim Faraji**, Ali Rajabpour, Temperature profile for nanoscale Poiseuille flow: A multiscale study. Journal of Mechanical Science and Technology **30**, 803-807 (2016).

Computer Skills

C++/C, Fortran, Matlab, Bash/Zsh scripting, Microsoft Windows, Unix Systems, LaTeX, LAMMPS

Languages

English (Fluent); Dutch (Basic); Persian (Native).